VILNIUS UNIVERSITY

Donatas Narbutis

Star Clusters in the M31 Galaxy Southwest Field. Photometric Survey and Population Properties

Doctoral Dissertation

Physical sciences, Physics (02 P)

Vilnius, 2010

Doctoral Dissertation was completed during 2006–2010 at Vilnius University.

Scientific supervisor:

Dr. Vladas Vansevičius (Vilnius University, Institute of Physics of Center for Physical Sciences and Technology, Physical sciences, Physics – 02 P)

VILNIAUS UNIVERSITETAS

Donatas Narbutis

Žvaigždžių spiečiai M31 galaktikos pietvakarinėje dalyje. Fotometrinė apžvalga ir populiacijos savybės

Daktaro disertacija

Fiziniai mokslai, fizika (02 P)

Vilnius, 2010

Disertacija rengta 2006–2010 metais Vilniaus universitete.

Mokslinis vadovas:

Dr. Vladas Vansevičius (Vilniaus universitetas, Fizinių ir technologijos mokslų centro Fizikos institutas, fiziniai mokslai, fizika – 02 P)

Abstract

Observational evidence that star formation proceeds in a clustered manner raises a question on the mass function of star clusters and their evolution. However, we have a limited scope of these processes in the Milky Way galaxy. The M31 galaxy is the nearest stellar system similar to our Galaxy, therefore, it is the most suitable one to provide clues for understanding the star cluster population and the evolution of galactic structures. However, detailed study of stellar populations and star clusters is a challenging task for ground-based observations due to crowded stellar fields.

Using Subaru telescope Suprime-Cam wide-field images, a survey of clusters was carried out in the disk region of the M31 galaxy southwest field, which is a close analogue to that of the Solar neighborhood in terms of chemical composition, stellar density, and quiescent star formation. Data analysis methods and programs were developed, tested, and applied for crowded wide-field image reduction and evolutionary parameter determination of semi-resolved star clusters.

The main results are: (1) enhanced star cluster formation activity in M31 occurred $\sim$70 Myr ago; (2) approximately 10% of stars born in star clusters remain there at 100 Myr age; (3) the characteristic lifetime of a cluster of $\sim 10^4$ $M_\odot$ mass is $\sim$300 Myr; (4) the mass function of star clusters in M31 is similar to that in other low star formation activity galaxies, and it is best described by the Schechter's function with a characteristic mass of $\sim 2 \times 10^5$ $M_\odot$; (5) a rich intermediate-mass cluster population in M31, which appears to be scarce or hidden by dust clouds in the Milky Way galaxy, was discovered.

Acknowledgments

I would like to express gratitude to Rima Stonkutė, Audrius Bridžius, Dmitrij Semionov, Viktoras Deveikis, Ramūnas Vanagas, Ieva Šablevičiūtė, Tadas Mineikis, Valdas Vansevičius, Mark Kidger, Fabiola Martin-Luis, Nobuo Arimoto, and Keiichi Kodaira.

I appreciate numerous interactions and help from J. Sūdžius, S. Bartašiūtė, J. Sperauskas, A. Kučinskas, V. Straižys, G. Trinkūnas, S. Narbutytė, S. Kavaliauskas, T. Luneckas, M. Karčiauskas, J. Bagdonaitė, V. Dobrovolskas, A. Ivanauskas, S. Bekeraitė, A. Pučinskas, S. Raudeliūnas, R. Lazauskaitė, G. Tautvaišienė, K. Černis, S. Lovčikas, G. Valiauga, G. Kakaras, R. Beinorienė, O. Gaubienė, A. Visockienė, P. Jablonka, T. Hasegawa, Y. Komiyama, S. Miyazaki, C. Ikuta, K. Ohta, N. Tamura, and Y. Yamada among many people.

I would like to acknowledge Vilnius University, Institute of Physics, and State Studies Foundation for financial support providing opportunities to participate in summer/winter schools and conferences, and exchange ideas with other groups working on the same subject.

I am very grateful to supervisor Vladas Vansevičius and indebted to my parents and family.

Contents

Introduction

Motivation

Formation and evolution of galaxies is one of the most important problems in contemporary astrophysics requiring the study of distant as well as near objects in the universe. The valid galaxy formation theory has to be based on understanding of physical processes triggering and suspending star formation, since star formation in general determines the luminosity, chemical, and structural evolution of galaxies.

It was not possible till now to obtain a panoramic view of the Milky Way galaxy (MW), because of the Solar system's proximity to the galaxy plane within the dusty disk. Interstellar extinction and only approximately known distances to the individual MW objects limit detailed studies to observations of the nearby star formation regions. However, it is important to understand the formation and evolution of the entire disk in order to link the epoch of galaxy formation and the present. Therefore, a more detailed understanding of the global star formation process requires observation of the nearby stellar systems, which are morphologically similar to the MW.

In this context, a detailed population study of the nearest disk galaxy, M31, is indispensable. Observations of spiral arms and star forming regions of this galaxy allow us to determine causes and consequences of star formation processes and their impact on the evolution of stellar population across the galaxy. Star clusters are a suitable tool to solve this problem, since they normally represent a single stellar population and can be easily detected in images, their properties can be modeled at various evolutionary stages and compared to observations.

A recently developed integrated galactic initial mass function theory (Pflamm-Altenburg & Kroupa 2008, and references therein) is based on empirical assumptions – one of them is the star cluster mass function and factors affecting its properties. The universality of the star cluster mass function can be tested only via observations.

Extensive studies of star clusters on the galaxy scale have been carried

out mainly in nearby disk and dwarf galaxies. The M31 galaxy, as the nearest spiral galaxy and a close analogue to the MW, has been regarded to be the most suitable to provide data for understanding of the galaxy structures, and to further elucidate the evolution of disk galaxies.

Many detailed studies of star clusters in M31 were devoted to deriving information related to the structure and evolution of star clusters and of the hosting galaxy: see the review in Kodaira (2002) and the introduction of Caldwell et al. (2009), and the works cited therein, among others.

Numerous *Hubble Space Telescope* (*HST*) observations of M31 were devoted to the studies of globular clusters (see Barmby et al. 2002, 2007 and references therein). Studies of the M31 disk clusters benefited from these high-resolution images, which were used by Williams & Hodge (2001b,a) to identify young star cluster candidates. Recently an extensive archival image survey of *HST* WFPC2/ACS instrument fields, which are scattering a wide area of M31 in patches, was conducted in search of new clusters (see Krienke & Hodge 2007, 2008 and references therein).

Although the M31 galaxy is the most suitable object for such studies, due to its wide extent on the sky and crowded stellar fields in the disk region, no homogeneous and deep star cluster surveys, covering the entire galaxy, were performed. Subaru telescope equipped with Suprime-Cam wide-field CCD camera and good observing conditions allowed us to perform high quality observations of the southwest field in the M31 galaxy disk. This data supplemented with images obtained by other ground-based telescopes and *HST*, *Spitzer*, and *GALEX* space observatories enabled us to determine evolutionary parameters for the representative star cluster sample of the M31 galaxy and compare its properties to the properties of clusters in the MW and other galaxies.

Aims of the study

1. Investigate the properties of star cluster population in the M31 galaxy southwest field.

2. Develop methods of analysis for the wide-field CCD photometry of star clusters and determination of their structural and evolutionary parameters.

Main tasks

1. Develop a method and software for the reductions of the wide-field mosaic CCD images adapted for accurate photometry.

2. Develop a method and program to derive structural parameters of semi-resolved star clusters.

3. Develop a method to derive evolutionary parameters of star clusters based on broadband multicolor photometry.

4. Perform a homogeneous survey of star clusters in the M31 galaxy southwest field and produce multi-band images (wavelength range from 150 nm to 21 cm) of the cluster sample for determination of their structural and evolutionary parameters.

5. Investigate the population of star clusters in the M31 galaxy southwest field, determine the star cluster formation history, mass function and disruption rate, and compare properties of the cluster population with the results derived in other galaxies.

Results and statements to defend

1. Derived structural and evolutionary parameters based on analysis of multi-band photometry results of 238 star clusters in the M31 galaxy southwest field.

2. Developed star cluster analysis methods and programs for: (1) reduction of the wide-field images registered with mosaic CCD cameras; (2)

determination of the structural parameters of semi-resolved star clusters; (3) quantification of the evolutionary parameters of star clusters based on integrated broadband multicolor photometry.

3. Properties of star cluster population in the M31 galaxy southwest field are: (1) enhanced star cluster formation activity $\sim$70 Myr ago; (2) only $\sim$10% of formed stars remain in clusters at the age of $\sim$100 Myr; (3) a typical lifetime of the cluster of $\sim 10^4\,M_\odot$ mass before its disruption is $\sim$300 Myr; (4) the mass function of massive ($\gtrsim$3000 $M_\odot$) star clusters is described well by the Schechter's function with a characteristic mass $m^* = 2 \times 10^5\,M_\odot$.

Personal contribution

The author developed all methods and majority of programs for reduction of the high quality wide-field mosaic CCD images, developed a method and contributed to coding the program for determination of structural parameters of semi-resolved star clusters. The author performed a feasibility study of the star cluster evolutionary parameter quantification method, substantially contributed to the homogeneous star cluster survey in the M31 southwest field, determined structural parameters of star clusters, constructed multi-band images of star clusters, and performed their photometry. The author performed the analysis of star cluster population in the M31 galaxy southwest field and derived its parameters.

Publications on thesis topic in refereed journals

1. Kodaira K., Vansevičius V., Bridžius A., Komiyama Y., Miyazaki S., Stonkutė R., Šablevičiūtė I., **Narbutis D.** 2004, *A Survey of Compact Star Clusters in the South-West Field of the M31 Disk* // Publications of the Astronomical Society of Japan, 56, 1025–1040.
2. **Narbutis D.**, Vansevičius V., Kodaira K., Šablevičiūtė I., Stonkutė R., Bridžius A. 2006, *A Survey of Compact Star Clusters in the South-West Field of the M31 Disk. UBVRI Photometry* // Baltic Astronomy, 15, 461–469.
3. **Narbutis D.**, Stonkutė R., Vansevičius V. 2006, *A Comparison of the Published Stellar Photometry Data in the South-West Field of the Galaxy M31 Disk* // Baltic Astronomy, 15, 471–480.
4. Šablevičiūtė I., Vansevičius V., Kodaira K., **Narbutis D.**, Stonkutė R., Bridžius A. 2006, *A Survey of Compact Star Clusters in the South-West*

Field of the M31 Disk. Structural Parameters // Baltic Astronomy, 15, 547–560.

5. **Narbutis D.**, Vansevičius V., Kodaira K., Bridžius A., Stonkutė R. 2007, *Photometry of Star Clusters in the M31 Galaxy. Aperture Size Effects* // Baltic Astronomy, 16, 409–420.
6. **Narbutis D.**, Bridžius A., Stonkutė R., Vansevičius V. 2007, *Accuracy of Star Cluster Parameters from Integrated UBVRI Photometry* // Baltic Astronomy, 16, 421–429.
7. Šablevičiūtė I., Vansevičius V., Kodaira K., **Narbutis D.**, Stonkutė R., Bridžius A. 2007, *A Survey of Compact Star Clusters in the S-W Field of the M31 Disk. Structural Parameters II* // Baltic Astronomy, 16, 397–408.
8. **Narbutis D.**, Vansevičius V., Kodaira K., Bridžius A., Stonkutė R. 2008, *A Survey of Star Clusters in the M31 South-West Field. UBVRI Photometry and Multi-Band Maps* // The Astrophysical Journal Supplement Series, 177, 174–180.
9. Bridžius A., **Narbutis D.**, Stonkutė R., Deveikis V., Vansevičius V. 2008, *Accuracy of Star Cluster Parameters from Integrated UBVRIJHK Photometry* // Baltic Astronomy, 17, 337–349.
10. Deveikis V., **Narbutis D.**, Stonkutė R., Bridžius A., Vansevičius V. 2008, SimClust – *a Program to Simulate Star Clusters* // Baltic Astronomy, 17, 351–361.
11. Kodaira K., Vansevičius V., Stonkutė R., **Narbutis D.**, Bridžius A. 2008, *Compact Star Clusters in M31 Disk* // Astronomical Society of the Pacific Conference Series, 399, 431–438.
12. Vansevičius V., Kodaira K., **Narbutis D.**, Stonkutė R., Bridžius A., Deveikis V., Semionov D. 2009, *Compact Star Clusters in the M31 Disk* // The Astrophysical Journal, 703, 1872–1883.
13. **Narbutis D.**, Vanagas R., Vansevičius V. 2009, StarL – *a Program to Correct CCD Image Defects* // Baltic Astronomy, 18, 219–224.

Other publications in refereed journals

1. Kidger M., Martin-Luis F., **Narbutis D.**, Perez-Garcia A. 2003, *The Atmospheric Extinction Profile in the Canary Islands: I – The Visible Extinction* // The Observatory, 123, 145–150.
2. Kidger M., Martin-Luis F., Nicolas Gonzalez-Perez J., **Narbutis D.** 2004, *A Resource for Multifrequency Campaigns: a Revised Catalogue of UBVRIJHK Calibration Stars in AGN/blazar Fields* // New Astronomy Reviews, 48, 505–507.
3. Kidger M., Martin-Luis F., **Narbutis D.** 2004, *A Search for Rapid Optical Spectral Variability in Blazars* // New Astronomy Reviews, 48, 509–512.
4. Vansevičius V., Arimoto N., Hasegawa T., Ikuta C., Jablonka P., **Narbutis D.**, Ohta K., Stonkutė R., Tamura N., Vansevičius V., Yamada Y. 2004,

The Full-fledged Dwarf Irregular Galaxy Leo A // The Astrophysical Journal Letters, 611, L93–L96.

5. Pignata G., Patat F., Benetti S., Blinnikov S., Hillebrandt W., Kotak R., Leibundgut B., Mazzali P., Meikle P., Qiu Y., Ruiz-Lapuente P., Smartt S., Sorokina E., Stritzinger M., Stehle M., Turatto M., Marsh T., Martin-Luis F., McBride N., Mendez J., Morales-Rueda L., **Narbutis D.**, Street R. 2004, *Photometric Observations of the Type Ia SN 2002er in UGC 10743* // Monthly Notices of the Royal Astronomical Society, 355, 178–190.
6. Kidger M., Martin-Luis F., Artigue F., Gonzalez-Perez J., Perez-Garcia A., **Narbutis D.** 2006, *The Visible and Near-Infrared Extinction at the Canary Islands International Observatories – Paper II* // The Observatory, 126, 166–176.
7. Stonkutė R., Vansevičius V., Arimoto N., Hasegawa T., **Narbutis D.**, Jablonka P., Ohta K., Tamura N., Yamada Y. 2008, *An Extended Star Cluster at the Outer Edge of the Spiral Galaxy M33* // The Astronomical Journal, 135, 1482–1487.

Presentations at conferences

1. **Narbutis D.**, Vansevičius V., Kodaira K., Bridžius A., Šablevičiūtė I., Stonkutė R., *Star Clusters in the Andromeda Galaxy* // "12 Questions on Star and Massive Star Cluster Formation" (eds. T. Wilson ir M. Kissler-Patig), Garching (Germany), 3–6 July, 2007 (oral presentation).
2. Kodaira K., Vansevičius V., Stonkutė R., **Narbutis D.**, Bridžius A., *Compact Star Clusters in M31 Disk* // "The 1st Subaru International Conference: Panoramic Views of Galaxy Formation and Evolution" (eds. T. Kodama, T. Yamada, K. Aoki), Shonan Village Center, Hayama (Japan), 11–16 December, 2007 (oral presentation).
3. **Narbutis D.**, Vansevičius V., Kodaira K., Stonkutė R., Bridžius A., Semionov D., Deveikis V., *Properties of Star Clusters in the M31 Disk* // "From Taurus to the Antennae" (ed. S. Goodwin), University of Sheffield (England), 4–8 August, 2008 (oral presentation).
4. **Narbutis D.**, Vansevičius V., Kodaira K., Stonkutė R., Bridžius A., Semionov D., Deveikis V., *Properties of Star Clusters in the M31* // "XX Canary Islands Winter School of Astrophysics" (ed. D. Martinez-Delgado), Tenerife (Spain), 17–28 November, 2008 (poster).
5. Deveikis V., **Narbutis D.**, Vansevičius V., Bridžius A., Stonkutė R., *Stochastic Modeling of Star Clusters* // "38th Lithuanian National Physics Conference", Vilnius University (Lithuania), 8–10 June, 2009 (poster).
6. **Narbutis D.**, Deveikis V., Stonkutė R., Semionov D., Bridžius A., Kodaira K., Vansevičius V., *Compact star clusters in the Andromeda galaxy disk* // "38th Lithuanian National Physics Conference", Vilnius University (Lithuania), 8–10 June, 2009 (oral presentation).

Thesis outline

The dissertation consists of **Introduction**, three **Chapters**, **Conclusions**, and **References**.

Chapter 1 presents and discusses observations and data of the homogeneous star cluster survey in the M31 galaxy southwest field, photometry and structural parameter results, and object identification in multi-band (wavelength range from 150 nm to 21 cm) images.

Chapter 2 describes developed analysis methods of star clusters and software, suitable for: (1) reduction of wide-field mosaic images; (2) determination of structural parameters of semi-resolved star clusters; (3) quantification of star clusters based on their broadband multicolor photometry data.

Chapter 3 provides analysis results of star cluster population in the M31 galaxy southwest field: (1) determined star cluster formation history; (2) mass function; (3) disruption rate. The determined parameters are compared to star cluster population properties in other galaxies.

Chapter 1

Star Cluster Sample

Initial study of star clusters in the M31 galaxy southwest field (Kodaira et al. 2004) of an apparent size less than $\sim 3''$ using high-resolution Suprime-Cam (Miyazaki et al. 2002) mosaic images revealed that some of the previously suspected globular cluster (GC) candidates should be classified as open clusters (OCs). This suggests that there is a new kind of star clusters, which is not well known in the MW, but whose counterparts are probably present in Large Magellanic Cloud/Small Magellanic Cloud (LMC/SMC; Kodaira 2002; Kodaira et al. 2004, 2008).

They are apparently more massive than typical OCs in the Solar neighborhood (Piskunov et al. 2008), but less massive than the typical GCs in MW (McLaughlin & van der Marel 2005). The presence of an intermediate disk population of star clusters, which may contribute to the understanding of disk evolution history, suggested a more detailed study.

Our survey, using Suprime-Cam mosaic images, completely covers the area of $17.5' \times 28.5'$ in the southwest field of the M31 disk. About 50 bright ($17.0 \lesssim V \lesssim 19.0$ mag) members of M31 cluster sample from Narbutis et al. (2006b) photometric analysis were studied in detail concerning their radial surface brightness profiles using a tidal-cutoff King model (King 1962) and a power-law EFF model (Elson et al. 1987). Their distribution in the half-light radius vs. the absolute V passband magnitude diagram (Šablevičiūtė et al. 2007) shows that these compact clusters are occupying the same domain as faint GCs (e.g., Barmby et al. 2007).

A comparison in the parameter domain of the King model (Šablevičiūtė et al. 2006) confirms a visual impression that compact clusters have similar radial profiles to GCs, except for minor irregularities, which become visible in high-resolution images. Comparison of the EFF model parameters of compact clusters and massive clusters in LMC (Mackey & Gilmore 2003) and SMC (Hill & Zaritsky 2006) shows that the present sample of compact clusters may have the same structural nature as massive clusters in the

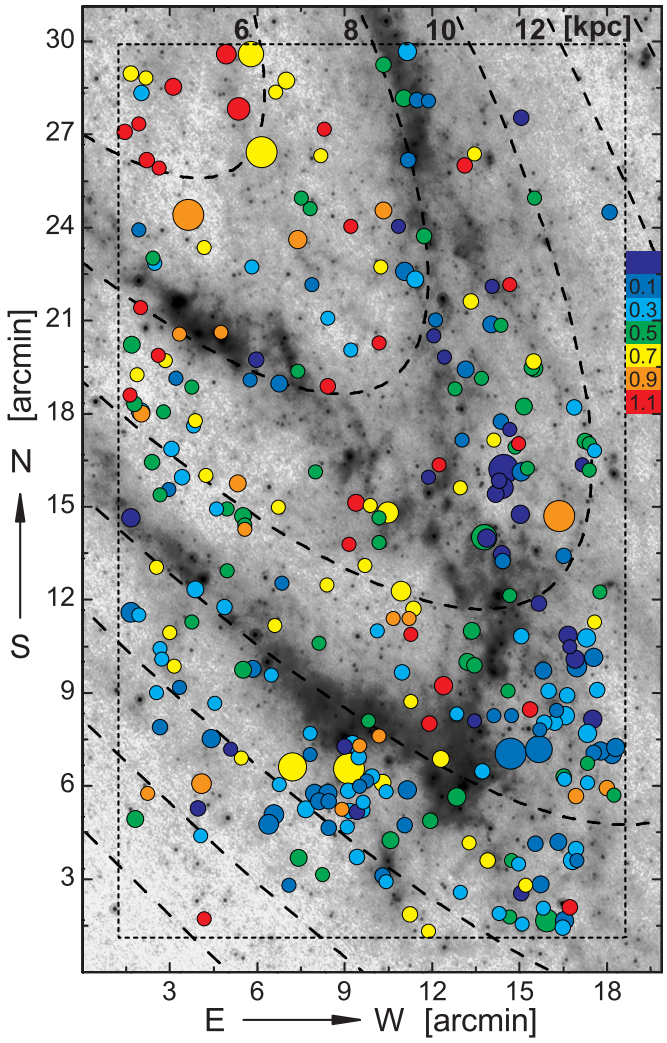

Fig. 1.1. Star cluster candidates (285 objects) in the M31 southwest field are overlaid on the *Spitzer* (24 μm) image. Circle size corresponds to the V passband magnitude and circle color represents the observed $B-V$ (see the color bar for coding). Elliptical ring segments, indicating distances from the M31 center (6–18 kpc), are marked with dashed lines. The rectangle (dotted line) indicates the Suprime-Cam survey area. North is up, east is left.

LMC/SMC (Šablevičiūtė et al. 2006).

These promising results motivated to extend the survey of clusters based on the high-resolution Subaru Suprime-Cam observations, covering ∼15% of the deprojected M31 galaxy disk area (see Fig. 1.1), to a deeper magnitude of $V \lesssim 20.5$ mag (see Fig. 1.2).

The homogeneous *UBVRI* aperture CCD photometry of 285 selected cluster candidates (169 of them identified for the first time) with absolute magnitudes down to $M_V \lesssim -4$ mag was performed using frames of the Local Group Galaxies Survey (LGGS; Massey et al. 2006), which were processed with software developed for removal of CCD image defects and wide-field mosaic homogenization.

We have developed and applied a method to derive structural parameters from the surface brightness distribution of clusters by properly accounting

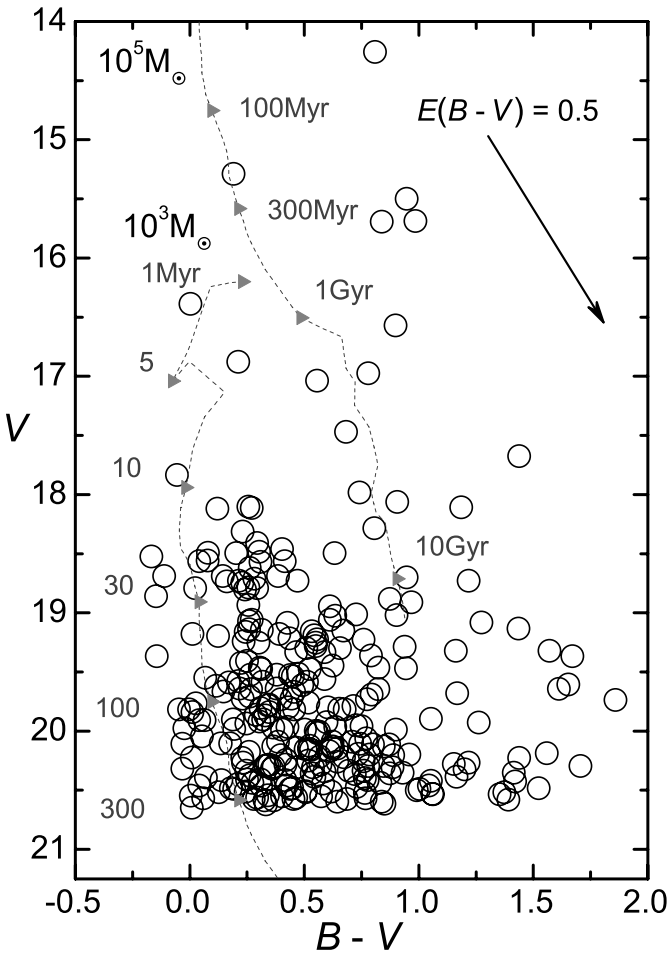

Fig. 1.2. Observed V vs. $B-V$ diagram of 285 star cluster candidates (circles). PEGASE SSP models of $Z = 0.008$ and ages ranging from 1 Myr to 15 Gyr are marked with dashed lines for clusters of 10^3 and $10^5\,M_\odot$ mass. The reddening vector of $E(B-V) = 0.5$, corresponding to the standard extinction law, is indicated.

for the contaminating stars, superimposed on their smooth profile. The final sample, containing 238 high-probability star cluster candidates (hereafter star clusters) of typical half-light radius $r_h \sim 1.5\,\mathrm{pc}$, was selected by specifying a lower limit of $r_h \gtrsim 0.15''$ ($\gtrsim 0.6\,\mathrm{pc}$; see Fig. 1.3).

Each object in the catalog provided by Narbutis et al. (2008, see Tab. 1.2) is supplemented with multi-band color maps combined from ultraviolet (*GALEX* telescope), optical (LGGS), infrared (2MASS survey and *Spitzer* telescope), and neutral hydrogen (HI; WSRT radio telescope) observations (see Fig. 1.5). Seventy seven star clusters from the catalog are located in the *HST* archive frames.

The mass vs. age distribution of 238 star clusters in M31 southwest field of our sample is displayed in Fig. 1.4, overplotted with M31 disk clusters younger than 1 Gyr form MMT spectroscopic survey by Caldwell et al. (2009). The majority of star clusters in our sample are of lower mass due to photometric selection limit of $V < 20.5\,\mathrm{mag}$, which allows us to study a

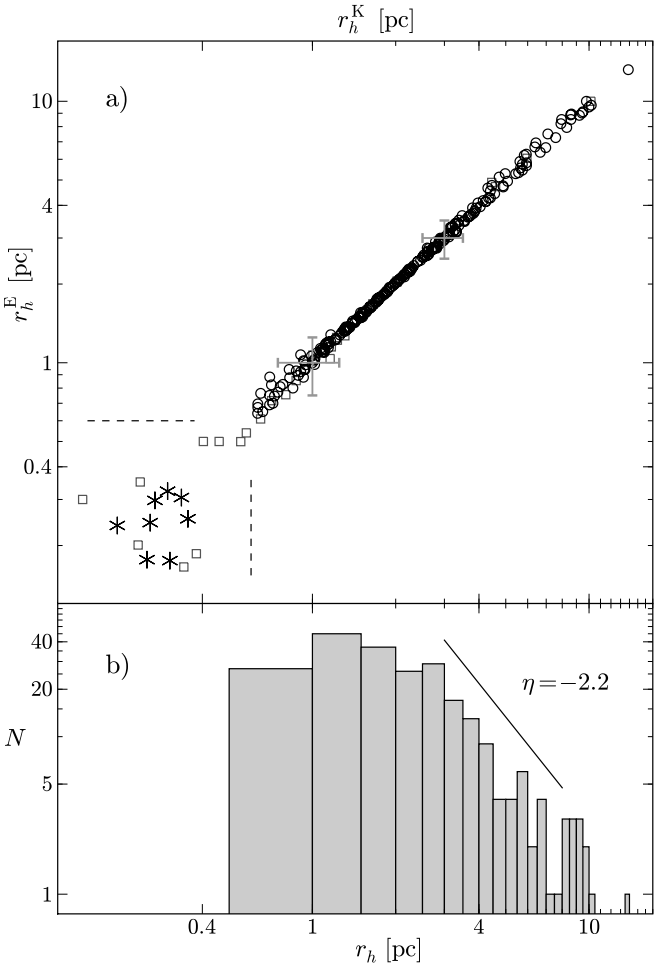

Fig. 1.3. Half-light radii of star cluster candidates. (a) Determined half-light radii of 285 initial sample objects – based on the EFF model, $r_h^{\rm E}$, and the King model, $r_h^{\rm K}$ (squares mark rejected cluster candidates; circles – selected 238 clusters; asterisks – PSFs constructed in the survey field and analyzed as "virtual objects"; dashed lines – the applied half-light radii selection limit $r_h \gtrsim 0.6\,$pc; error-bars – typical σ_{r_h}). (b) Histogram of average half-light radii, $r_h = (r_h^{\rm K} + r_h^{\rm E})/2$, of 238 clusters, overplotted with a slope $\eta = -2.2$ line, defined as $N(r_h){\rm d}r_h \propto r_h^{\eta}{\rm d}r_h$.

complete and homogeneous cluster sample in wide-field area of M31 galaxy for the first time.

Here we present results of observations conducted with Suprime-Cam and images retrieved from the LGGS archive, which were used for star cluster survey and photometry. The star cluster sample selection was based on structural parameters and half-light radii derived by structure model fitting. The developed software to process wide-field mosaic images and perform aperture size tests ensured high precision photometry of objects.

Photometric data was supplemented with multi-band images and used to derive evolutionary parameters of star clusters in the southwest field of M31 galaxy disk. High-resolution *HST* images served as reference for cluster cross-identification and sample completeness estimate. The *UBVRI* photometry data and multi-band maps are used to derive structural and evolutionary parameters (age, mass, metallicity) and extinction. The derived

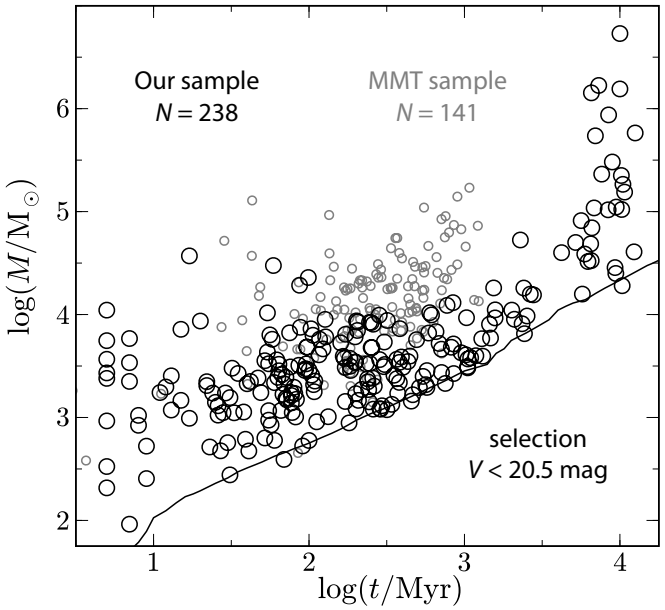

Fig. 1.4. Mass vs. age diagram of 238 star clusters (large circles) overplotted with $V < 20.5$ mag selection limit (line). Objects with Hα emission are omitted. Small circles indicate M31 disk clusters younger than 1 Gyr from MMT spectroscopic survey by Caldwell et al. (2009).

half-light radii were studied in connection with the simple stellar population (SSP) model fitting results.

The following M31 parameters are adopted in this study: distance modulus of $m - M = 24.47$ (785 kpc, thus $1'' \equiv 3.8$ pc; McConnachie et al. 2005); center coordinates $\alpha_{\rm J2000} = 0^{\rm h}42^{\rm m}44.3^{\rm s}$, $\delta_{\rm J2000} = 41°16'09''$ (NASA Extragalactic Database); major axis position angle of 38° (de Vaucouleurs 1958); disk inclination angle to the line of sight of 75° (Gordon et al. 2006).

1.1 Observations and Data

1.1.1 Suprime-Cam Images

Taking into account the angular size of the M31 galaxy, the Subaru telescope equipped with the Suprime-Cam is an ideal instrument to study its stellar content. A single-shot Suprime-Cam mosaic (5×2 CCD chips; 2K×4K each) covers a field of $34' \times 27'$ (scale $0.2''\,{\rm pix}^{-1}$), and magnitude of $V \sim 25$ mag is reached in 60 s.

Each of the B, V, R, and Hα frames was exposed for 5×2 min. The survey field of the $17.5' \times 28.5'$ was centered at $\alpha_{\rm J2000} = 0^{\rm h}40.9^{\rm m}$, $\delta_{\rm J2000} = +40°45'$. The characteristic full width at half maximum (FWHM) of stellar images (PSF) is $0.7''$ (see Tab. 1.1).

The telescope was dithered by $\sim 1'-4'$ between shots to avoid gaps midst CCDs while mapping the survey field. The exposure dithering pattern also

Tab. 1.1. Parameters of Original Images.

Source	Images	FWHM (arcsec)	Scale (arcsec pixel^{-1})
Suprime-Cam	*B*, *V*, *R*, Hα	0.6−0.7	0.20
LGGS[a].....	*U*, *B*, *V*, *R*, *I*, Hα	0.7−1.3	0.27
GALEX[b].....	FUV, NUV	$\sim$4.5, $\sim$5.5	1.50
2MASS.....	*J*, *H*, K_s	$\sim$3.5	1.00
Spitzer.....	24 μm	$\sim$6.0	2.45
HI[c]	21 cm	...	10.3

NOTES. [a] Mosaic images of the F6–F9 fields.
[b] Strongly variable asymmetric PSF.
[c] TIFF format image.

allowed to perform an internal calibration of astrometry and photometry.

The standard reduction procedures (bias subtraction and flat-fielding) were performed with a software package SDFRED[1] (Yagi et al. 2002), dedicated to the Suprime-Cam data. The raw data were processed in a standard manner, but the stacking and the photometric calibration were made on chip-by-chip basis due to a certain non-uniformity found in the initial phase of the verification period. Special care was needed to subtract the background in the crowded area of the galaxy disk.

We have analyzed the Suprime-Cam images to find that the point spread function (PSF) is variable (FWHM up to $\sim$25%) across the Suprime-Cam field, especially in the four chips of mosaic corners. Although the majority of image sets have PSFs of a good quality (symmetric), we have noticed that the shape of PSF have changed between some subsequent exposures. However, tests show that the PSF variability in the stacked V passband mosaic image, which was used for star cluster survey, does not affect star cluster selection and accuracy of the derived structural parameters.

1.1.2 LGGS Images

We used publicly available LGGS[2] stacked U, B, V, R and I passband[3] mosaic images of M31 (fields F6, F7, F8, F9) by Massey et al. (2006), which overlap with Suprime-Cam field. The mosaic camera used by Massey

[1]SDFRED: `http://optik2.mtk.nao.ac.jp/subaru_red/SPCAM/.`

[2]LGGS: `http://www.lowell.edu/users/massey/lgsurvey.html.`

[3]R and I passbands are in Cousins system.

et al. (2006) consists of eight CCDs. Each CCD chip covers $9' \times 18'$ field and has an individual set of color equations.

We considered mosaic images, clean from cosmic rays and cosmetically, to be more preferable for aperture star cluster photometry than individual exposures. The dithering pattern of five individual exposures for each field is the same with maximum shifts up to $1'$ in respect to the first exposure. Exceptions are U passband observations in the F9 field, which has 6 individual exposures.

Massey et al. (2006) do not recommend straightforward use of their mosaic images for precise photometry, therefore, we treated each CCD chip area on the stacked mosaic image separately, with special care for objects residing on different CCDs in individual exposures.

The variable PSFs of four overlapping LGGS field (F6–F9) mosaic images were homogenized to the same FWHM = $1.5''$ (see Tab. 1.1). The mosaics were photometrically calibrated by using individual CCD color equations and the stellar photometry catalog from Massey et al. (2006) as a local photometric standard for zero-point calibration.

We note that a comparison of three published stellar photometry data sets in our survey field makes one to be cautious (Narbutis et al. 2006a) when using tertiary standards as local photometric standards. However, we used a carefully reduced and calibrated data set by Massey et al. (2006), which passed an internal consistency check, making it the most accurately calibrated photometry catalog of the M31 galaxy to date.

1.1.3 *HST* Images

The Multimission Archive at the Space Telescope Science Institute[4] was searched for *HST* frames overlapping with the Suprime-Cam survey field and publicly available. A dozen of *HST* frames were located in our survey field covering less than 20% of its extent.

Flat-fielded frames were cleaned of cosmic rays and corrected for distortions by employing procedures of the STSDAS package in the IRAF program system (Tody 1993). The World Coordinate System information was corrected for all *HST* frames by referencing the Suprime-Cam V passband

[4] *HST*: `http://archive.stsci.edu/hst/search.php`.

image, which was registered to the USNO-B1.0 catalog system.

The numbers of analyzed *HST* data sets/telescope pointings overlapping with the studied Suprime-Cam field are: 222/29 (WFPC2); 9/3 (ACS); 43/6 (STIS); and 75/19 (NICMOS).

Star cluster candidates from our catalog, presented in Tab. 1.2, have been identified only in the WFPC2 (71) and the ACS (6) frames – 77 objects in total.

1.1.4 Multi-Band Maps

The multi-band color images of clusters were produced from the LGGS (U, B, V, I, Hα), *GALEX* (FUV, NUV), 2MASS (J, H, $K_{\rm s}$), *Spitzer* (24 μm), and HI (21 cm) images. They serve as an illustrative material showing the objects' structure, the location of the aperture used for photometry, individual background conditions, and position in the survey field. These maps are also a valuable tool for revealing cluster interrelations with a global framework of various M31 galaxy components.

An example of the electronic multi-band color maps available online[5] and a layout template are shown in Fig. 1.5. Since the displayed intensity range is kept constant for all objects, colors of individual objects are roughly preserved. However, the real emission level at 24 μm should be estimated by referencing the object's position in the global *Spitzer* image of the survey field.

The LGGS mosaic images (Massey et al. 2006) in the U, B, V, I, and Hα passbands of the F7 or F8 fields were used for a multi-band map construction. For objects located to the south of the F7 field, images of lower resolution from field F8 were substituted.

The 2MASS J, H, and $K_{\rm s}$ passband "1×" and "6×" survey images were retrieved from the NASA/IPAC Infrared Science Archive[6] and co-added to increase their signal-to-noise ratio. In general, the "6×" co-added image was used, except for the gap region in the north of the surveyed field, where the "1×" image was substituted.

The *GALEX* NUV and FUV images by Gil de Paz et al. (2007) were

[5]M31 cluster multi-band maps: `http://dx.doi.org/10.1086/586736`.

[6]2MASS: `http://irsa.ipac.caltech.edu/`.

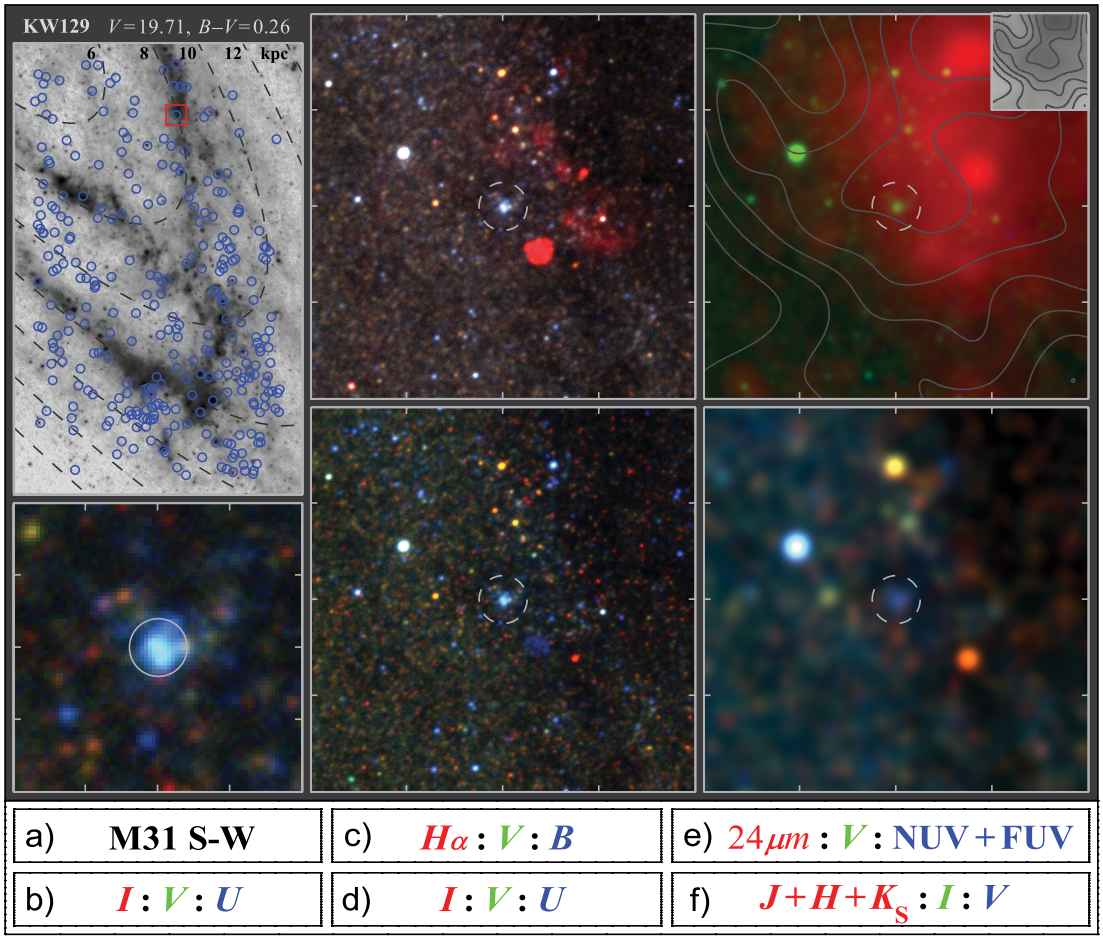

Fig. 1.5. An example of multi-band maps (top) and a corresponding layout template (bottom), indicating panel notations, is shown here as a guide to the individual multi-band color maps, constructed for all objects, available in the electronic edition of Narbutis et al. (2008). The object's ID, the V passband magnitude, and the $B-V$ color are provided in the top-left corner. Panel (a) shows positions of 285 objects in the M31 southwest field (circles); elliptical ring segments indicating distances from the M31 center (6–18 kpc) are marked with dashed lines overlaid on the *Spitzer* (24 μm) image; the object under consideration is indicated by a red square of a size equivalent to the size of panels (c–f). In panels (b–f) of the layout template, passbands of images displayed in red, green, and blue color channels are indicated by corresponding colors. The LGGS images were used in panels as follows: (b–d) U, B, V, I, Hα passbands of the original resolution; (e) the V passband of a homogenized PSF (FWHM = 1.5″); (f) the V and I passbands of a homogenized PSF (FWHM = 3.5″) matching the PSF of 2MASS images. Contour lines in panel (e) emphasize the HI distribution; the gray-shaded inset shows a global 21 cm emission intensity, black standing for the highest and white for the lowest signal level over the entire surveyed area. The size of panel (b) is 15″×15″, and the size of panels (c–f) is 80″×80″. The aperture used for the photometry is overlaid in panel (b). The object in panels (c–f) is marked with a circle of 10″ in diameter. North is up, east is left.

retrieved from the *GALEX* Atlas of Nearby Galaxies[7] and co-added to increase a signal-to-noise ratio.

The *Spitzer* MIPS (24 μm) post-BCD (basic calibrated data) images of M31 (Program ID 99) were retrieved from the *Spitzer* Science Center Data Archive[8], and mosaicked using the SWarp[9] program.

The HI (21 cm) image was retrieved from the National Radio Astronomy Observatory image gallery[10] (courtesy of NRAO/AUI and WSRT). It was converted from the TIFF to the FITS format using ImageTOOLSca[11]. The sky coordinate grid, indicated by Westmeier et al. (2005) in their Fig. 1 on the same HI image, was used for the initial registration. Fine adjustments were made assuming a global correlation between the *Spitzer* (24 μm) and HI (21 cm) source distributions, noted by Gordon et al. (2006).

The Suprime-Cam V passband mosaic image coordinate system was used as a reference to register and transform all images to the homogeneous pixel scale of $0.2''\,\mathrm{pix}^{-1}$. The IRAF's `geotran` procedure was used for the LGGS, *GALEX*, and 2MASS image transformations; the `wregister` procedure was used for the *Spitzer* (24 μm) and HI (21 cm) images.

All images were additionally processed with developed software to remove CCD defects and produced maps for star cluster analysis. Since the LGGS images cover a wide wavelength range, they served as a reference for registering other images. A visual inspection was carried out to ensure accurate coordinate match of the images prepared for a multi-band map production. The FWHM and original pixel scale values of those images are provided in Tab. 1.1.

The sub-images of $80''\times80''$, centered on the objects' position, were cut out from the transformed images. SAOImage DS9 was employed to combine them into multi-band color maps. The LGGS, 2MASS, and *GALEX* sub-images are displayed in a linear intensity scale, and the *Spitzer* sub-images are displayed in a square root scale. The minimal shown data level is individual for each sub-image, depending on the background intensity;

[7] *GALEX*: `http://archive.stsci.edu/prepds/galex_atlas/index.html`.

[8] *Spitzer*: `http://ssc.spitzer.caltech.edu/spitzerdataarchives/`.

[9] SWarp: `http://www.astromatic.net/software/swarp`.

[10] HI: `http://images.nrao.edu/object/index.php?id=475`.

[11] ImageTOOLSca: `http://arnholm.org/astro/software/ImageTOOLSca/`.

however, the range of displayed intensities was kept constant for all objects.

The constant displayed intensity limits across the surveyed area were applied only for HI (21 cm) sub-images and are overplotted with contour lines. A gray-shaded inset shows a global HI emission intensity, with black standing for the highest and white – for the lowest signal level over the survey area. Note, however, that the HI image is converted from the TIFF format and does not represent a real 21 cm emission distribution, serving for illustrative purposes only.

1.2 Star Cluster Survey

Detailed studies of the star clusters in M31 are essential to understanding the evolution mechanisms of disk galaxies and of the cluster population itself. Many observational surveys of this galaxy have been devoted to study of GCs (see, e.g., Barmby et al. 2002, 2007; Kim et al. 2007 and references therein).

Due to crowding, plausible detection and analysis of star clusters projected on the disk of M31 became feasible only with high-resolution imaging. However, *HST* observations cover only a small part of the M31 disk, and recent cluster population studies (e.g., Krienke & Hodge 2007) are based on *HST* fields scattered over the area of M31.

The study by Cohen et al. (2005), based on high-resolution Keck imaging, however, suggests that M31 cluster samples (e.g., Galleti et al. 2007) might be heavily contaminated by asterisms. The discussion on this issue by Caldwell et al. (2009) states that appearance of low-mass clusters dominated by several bright stars depends strongly on the photometric passband used, and emphasizes the need of multi-band observations to identify clusters correctly.

Therefore, high-resolution wide-field Suprime-Cam mosaics used for star cluster survey and multi-band images applied to verify star cluster candidates enable us to identify reliable sample of objects.

1.2.1 Sample Selection

The Suprime-Cam survey of star cluster-like objects was conducted in the southwest field of the M31 disk ($\sim$17.5′×28.5′ in size), centered at $\alpha_{\rm J2000}$ =

$0^{\rm h}40.9^{\rm m}$ and $\delta_{\rm J2000} = +40°45'$ (Fig. 1.1). Visual inspection of the high-resolution Suprime-Cam mosaic images, with characteristic FWHM of the PSF of $\sim$0.7″, enabled us to select the initial sample of $\sim$600 star cluster candidates up to $V \sim 21$ mag.

In addition, several objects that were not recognized as cluster candidates in our survey, were appended to the initial Suprime-Cam object sample from the Revised Bologna Catalog of M31 GCs and candidates V.3.2, July 2007[12] (Galleti et al. 2007) and from the recent *HST* survey of the M31 disk cluster population conducted by Krienke & Hodge (2007). About 40 objects, included in Galleti et al. (2007) and overlapping with our survey field originally come from the recent survey by Kim et al. (2007), however, $\sim$50% of these objects were omitted from our catalog because their surface brightness profiles closely resemble that of stars.

To study selection effects inherent to the initial cluster candidate sample, archival *HST* frames were employed. A completeness of $\sim$70% in the visual selection of star cluster candidates at the limiting magnitude of the catalog ($V \sim 20.5$ mag) was estimated by comparing our initial sample of $\sim$600 objects with an overlapping sample studied by Krienke & Hodge (2007).

We also checked our objects against available archival *HST* images, and some of our cluster candidates were classified as asterisms. Moreover, few new star cluster candidates, overlooked during a visual inspection of the Suprime-Cam images, were found on *HST* frames. Summing up results of these tests, we find the completeness of our cluster candidate sample to be higher than $\sim$50% at $V = 20.5$ mag (see Fig. 1.2).

This is a conservative magnitude limit for objects that can be identified as star clusters on the Suprime-Cam images. However, it is difficult to estimate the completeness of the present cluster candidate sample more accurately, since it depends on a strongly varying background object density across the surveyed area, and the clusters' luminosities, colors, and concentrations.

A strong contamination of young star cluster samples selected in M31 by asterisms has been demonstrated recently by Cohen et al. (2005). Therefore, in order to clean our initial cluster candidate sample ($V \lesssim 20.5$ mag), we

[12]M31 GCs: `http://www.bo.astro.it/M31/`.

determined cluster structural parameters and half-light radii (see Fig. 1.3) by employing FitClust program developed to analyze surface brightness distribution of semi-resolved star clusters and allowing to include individual stars in a structure model fit.

The analysis of multi-band color maps and FitClust results revealed several red objects, possessing smooth elliptical surface brightness distributions. They were also removed from the sample as probable background galaxies.

We did not include KWC13 and KWC24 from Kodaira et al. (2004) either, suspecting them to be background galaxies. After performing this cleaning, we ended up with the final catalog containing 285 star cluster candidates (169 of them identified for the first time). The final cluster candidate sample includes 77 objects observed by *HST*.

1.2.2 Photometry

For the photometry of 285 selected star cluster candidates, we used LGGS (Massey et al. 2006) U, B, V, R, and I passband mosaic images of four M31 fields (F6, F7, F8, and F9) overlapping with our survey field to produce a homogenized *UBVRI* photometric catalog of ($V \lesssim 20.5$ mag). Different aperture sizes and photometric background estimation areas were selected for individual clusters.

The aperture *UBVRI* CCD photometry was carried out by employing the IRAF's XGPHOT package. The images of all objects, except for five saturated in the I passband, are free of visible defects. Apertures were centered on clusters' luminosity distribution peaks in the Suprime-Cam V passband mosaic image and transformed to individual LGGS image coordinate systems with the IRAF's `geoxytran`.

In order to minimize cluster photometry contamination by background objects in crowded fields, we decided to use individual small circular (elliptical for the two bright objects KW102 and KW141 to avoid obvious nearby background stars) apertures; their sizes are provided in Tab. 1.2. The photometric background was determined in individually selected and object-centered circular annuli with typical inner and outer radii of $3''$ and $8''$, respectively. For some clusters, located on a largely variable background,

circular background determination zones were selected individually in representative areas (object-centered circular annuli with typical inner and outer diameters of 6″ and 16″, respectively).

The catalog of 285 star cluster candidates consists of 138 and 141 objects measured in two and three different LGGS fields, respectively, while six objects have been measured in one field. Two main types of error sources determine the final accuracy of the photometry: the photon noise – $\sigma_{\rm n}$ (estimated by XGPHOT) and the calibration procedure – $\sigma_{\rm c}$.

The V passband magnitude and colors, derived in different LGGS fields for each object, were examined interactively. Weighted averages were calculated taking into account individual $\sigma_{\rm n}$ and down-weighting data derived in the mosaic image areas combined from different CCDs. The rms of averaged magnitudes and colors characterize calibration errors in general, therefore, they were assigned to $\sigma_{\rm c}$.

Measured star clusters are relatively bright objects, therefore, photon noise is virtually negligible and photometric accuracy of the catalog is limited by the photometric calibration procedure. For the star clusters located in the mosaic image areas, stacked from different CCDs, we additionally used color equations of corresponding CCDs and performed independent transformations to the standard system. V passband magnitudes and colors, determined in different fields (F6–F9), were averaged by assigning smaller weights to the measurements performed on the mosaic image areas, stacked from different CCDs.

The lowest possible calibration errors of 0.010, 0.015, 0.020 mag were set for objects having 3, 2, and 1 independent measurements, respectively. The final photometric errors, provided in the catalog (Tab. 1.2), are calculated as $\sigma = (\sigma_n^2 + \sigma_c^2)^{1/2}$. The photometric error values, σ_V, for corresponding V passband magnitudes are plotted in Fig. 1.6.

We note that ∼10% of the objects from our sample have suspected variable stars contaminating the aperture photometry results. They were revealed by comparing overlapping LGGS fields observed on different nights.

The *UBVRI* photometry of our sample results in a smaller scatter in color-color diagrams (see Fig. 1.7) than photometry data of the same objects taken from the Revised Bologna Catalog of M31 GCs and candidates

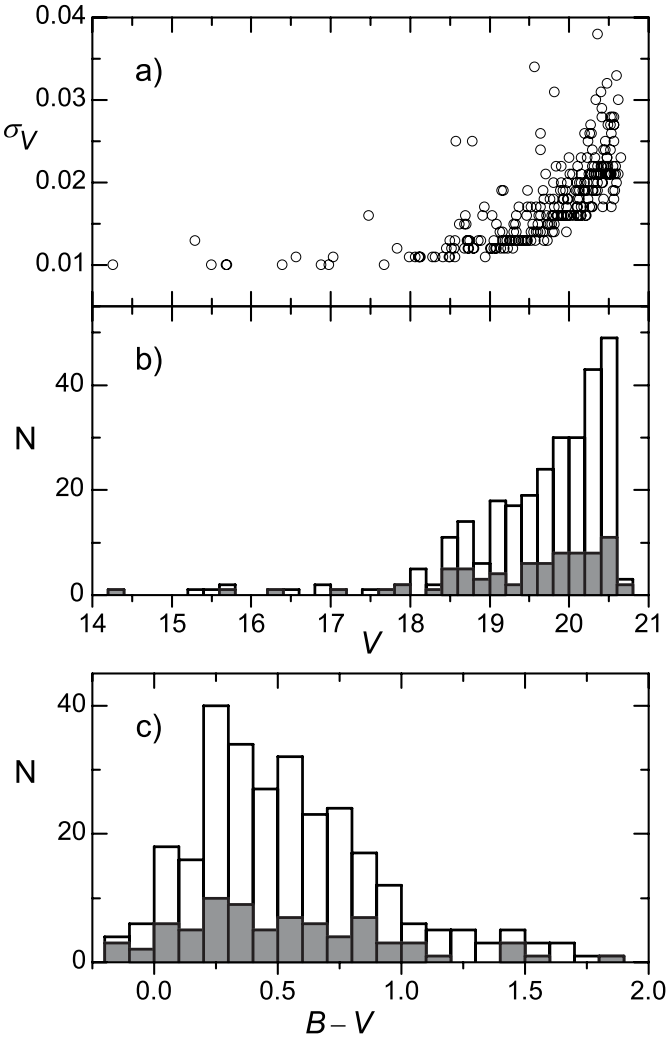

Fig. 1.6. Global characteristics of the star cluster candidate catalog (285 objects). Panels show (a) the photometric errors, σ_V, vs. V passband magnitudes (we adopted the lowest possible error of $\sigma_V = 0.01$ mag); (b) the observed V passband magnitude histogram (an object selection criterion is $V \lesssim 20.5$ mag); (c) the observed $B - V$ color histogram. Gray-shaded histograms are constructed for a sub-sample of 77 objects, located in the *HST* frames.

compiled by Galleti et al. (2004).

This is a result of homogeneous photometric survey and individual apertures carefully chosen for each star cluster. Therefore, accuracy of measured aperture colors of the M31 star clusters is satisfactory to be used for star cluster parameter (age, extinction, metallicity) determination basing on comparison with SSP models.

1.2.3 Aperture Size Effects

The aperture photometry errors of extended objects are determined by photon noise, photometric background uncertainty and calibration procedure errors. However, in the case of extragalactic star clusters projected on a crowded galaxy disk (e.g., M31), the flux from contaminating stars introduces bias to the true colors of the objects, and in some cases the contamination effect exceeds photometric errors.

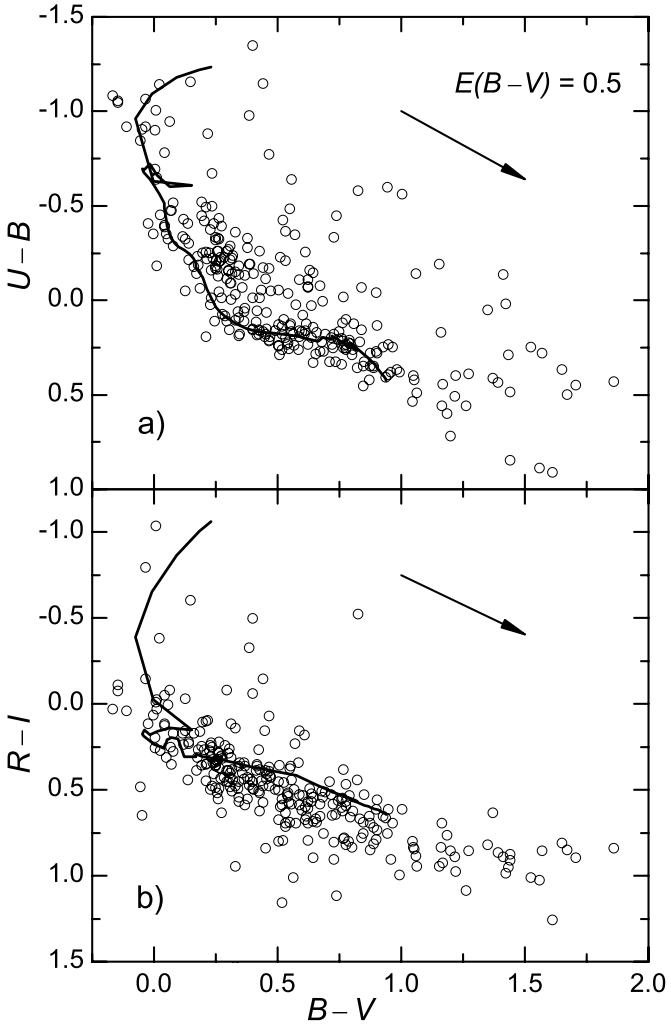

Fig. 1.7. Observed color-color diagrams of 285 catalog objects (circles). PEGASE SSP models of $Z = 0.008$ and ages ranging from 1 Myr to 15 Gyr are marked with solid lines. The reddening vectors of $E(B - V) = 0.5$, corresponding to the standard extinction law, are indicated.

The colors and density of dominating contaminants depend mainly on the age of background stellar populations and on the object location in the galaxy. In general, background stars are distributed randomly, therefore, a probability of their contaminating effect increases with the aperture size.

The resolution of ground-based images is limited by the atmospheric seeing. Therefore, colors of star clusters are affected by contaminating objects to a degree which depends on the quality of images, characterized by the FWHM of the PSF, and the location of the contaminant in respect to the aperture. The alteration of cluster's true colors also depends on the contaminant and the object luminosity ratio – faint star clusters are more affected.

Contaminants, residing outside the aperture, can be partly avoided by using high-resolution imaging, e.g., with the *HST*, however, the sky back-

ground determination becomes more complicated in this case (see discussion by Krienke & Hodge 2007). In order to estimate the resolution effect, we performed a comparison of the cross-identified cluster photometry from our sample and from the sample studied by Krienke & Hodge (2007).

It was demonstrated (Narbutis et al. 2007; Bridžius et al. 2008) that an uncertainty of cluster colors less than $\sim$0.03 mag is required to achieve a reasonable accuracy of age and extinction from integrated photometry. Therefore, to estimate the influence of background contaminants on the accuracy of object colors, we studied aperture size effects, based on our sample of 285 star cluster candidates.

In order to study aperture size effects, arising due to contamination by background stars, on the accuracy of colors, all star cluster candidates were additionally measured through the circular apertures increased/decreased by $0.6''$ in respect to the main aperture diameter. The same photometry reduction procedure, as that applied for the main aperture data, was used, and the differences of the V magnitudes and colors, measured through the increased or decreased and the main apertures, were calculated. These results also provide an estimate of possible star cluster color bias, arising due to aperture centering and size mismatch when measured in images from different surveys.

In Fig. 1.8 we plot ΔV vs. V. Here ΔV are differences of V magnitudes measured through the apertures increased or decreased by $0.6''$ and V magnitudes obtained through the main aperture. The aperture diameter of $3''$ was adopted for the majority of clusters and up to $10''$ for the brightest objects. Since bright objects were measured through large main apertures, that resulted in small magnitude differences. However, for faint objects ($V > 18.5$ mag) ΔV is significantly larger and has to be taken into account for the star cluster mass estimate.

In Fig. 1.9 we plot $\Delta(B-V)$, $\Delta(U-B)$ and $\Delta(V-I)$ vs. V magnitudes. The distribution of $\Delta(B-V)$ is symmetric. However, for faint objects ($V > 18.0$ mag) the distributions of $\Delta(U-B)$ and $\Delta(V-I)$ are asymmetric, suggesting that some objects are affected by blue and red contaminants, respectively. The same color differences are plotted vs. $B-V$ in Fig. 1.10. $\Delta(U-B)$ shows an asymmetric distribution due to the influence of blue

Fig. 1.8. Aperture size test results of the 285 star cluster candidates. ΔV – difference of V magnitudes measured through the apertures increased or decreased by $0.6''$ in respect to the main aperture (open/filled circles, respectively) and magnitudes, measured through the main aperture.

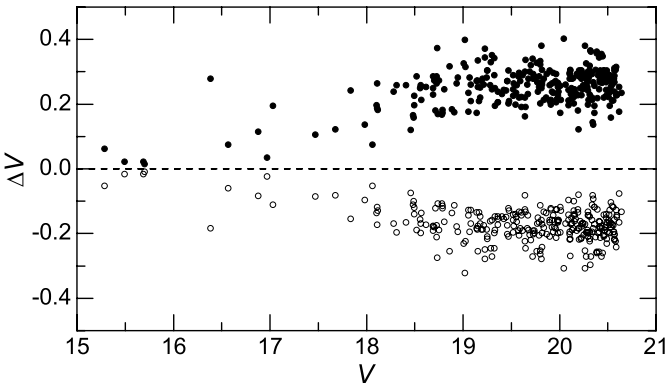

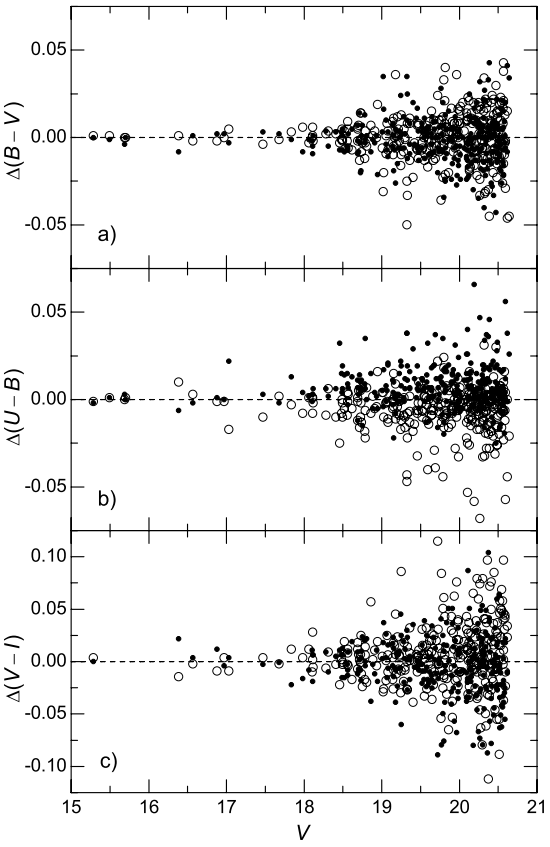

Fig. 1.9. The same as in Fig. 1.8, but for the $\Delta(B-V)$, $\Delta(U-B)$ and $\Delta(V-I)$ color differences.

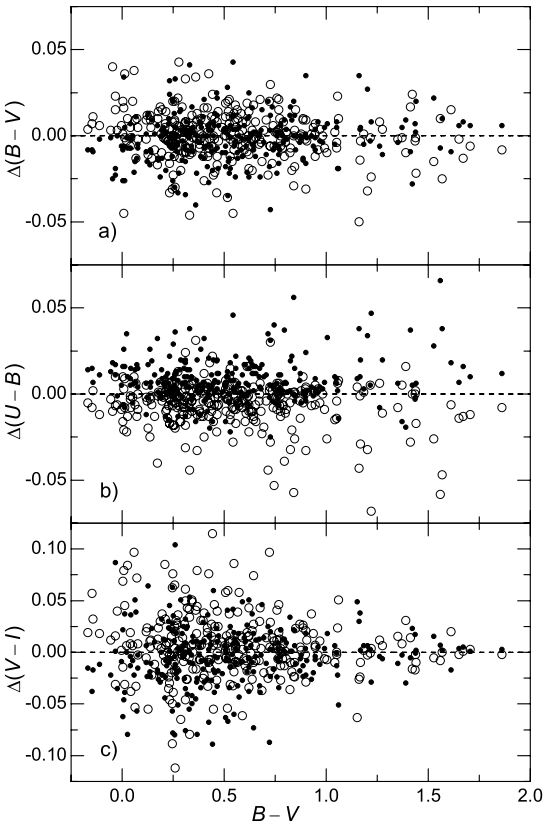

Fig. 1.10. The same as in Fig. 1.9, but the $\Delta(B-V)$, $\Delta(U-B)$ and $\Delta(V-I)$ color differences vs. $B-V$.

contaminants, which is stronger for star cluster candidates with $B-V > 0.5$. $\Delta(V-I)$ shows an asymmetric distribution for the objects with $B-V < 0.75$ due to the influence of red contaminants.

Uncertainties of cluster colors, arising due to the influence of contaminants, were estimated for each object based on $\Delta(U-B)$, $\Delta(B-V)$ and $\Delta(V-I)$. $U-B$ vs. $B-V$ diagrams of 285 star cluster candidates are

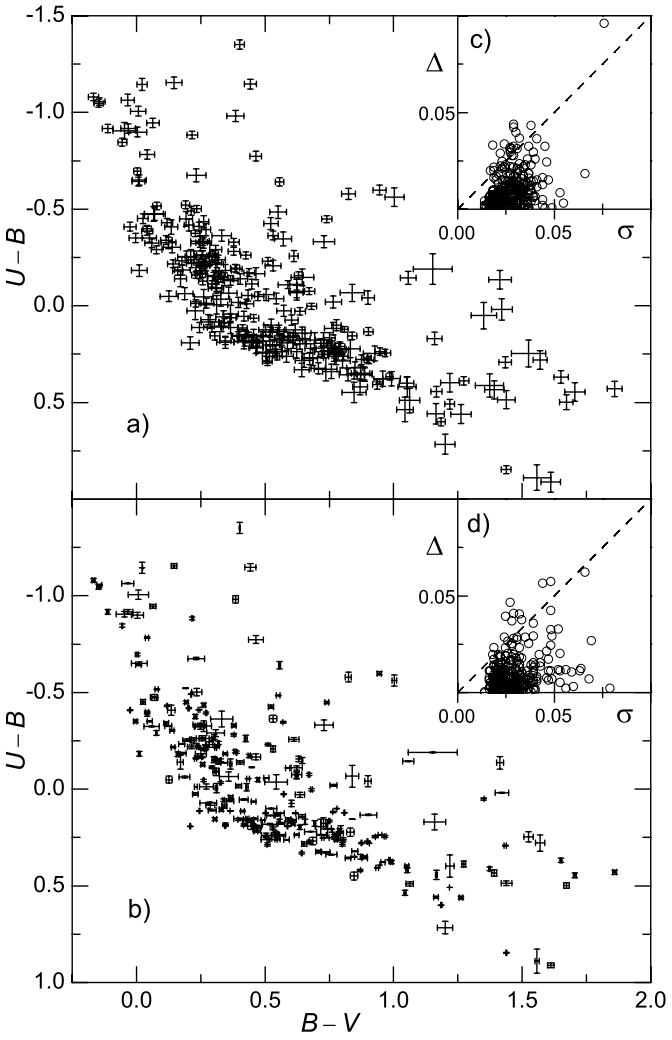

Fig. 1.11. The $U - B$ vs. $B - V$ diagrams for the 285 star cluster candidates. Error bars indicate photometric errors, σ, and the aperture size effects, Δ, in panels (a) and (b), respectively. In the insets $\Delta(B - V)$ of the aperture size test vs. photometric error, $\sigma(B - V)$, and $\Delta(U - B)$ vs. $\sigma(U - B)$ are shown in panels (c) and (d), respectively.

plotted in Fig. 1.11. The error bars indicate photometric errors, $\sigma(U - B)$, $\sigma(B - V)$ (Fig. 1.11 (a)), and $\Delta(U - B)$, $\Delta(B - V)$ (Fig. 1.11 (b)). Due to the influence of contaminants for a fraction of objects, 4% for $U - B$ and 7% for $B - V$, the Δ values exceed the σ values. In Fig. 1.12 the corresponding $V - I$ vs. $B - V$ diagrams are plotted. The $\Delta(V - I)$ values exceed the $\sigma(V - I)$ values for 21% of star clusters.

In the majority of cases photometric errors represent a true uncertainty of cluster colors well, however, for some faint objects, residing in crowded environments, these errors can be largely underestimated. It is noteworthy to say that possible biases in colors have to be taken into consideration prior to the cluster parameter quantification procedure, based on the SSP models.

A large sample of star clusters in M31 has been studied recently with

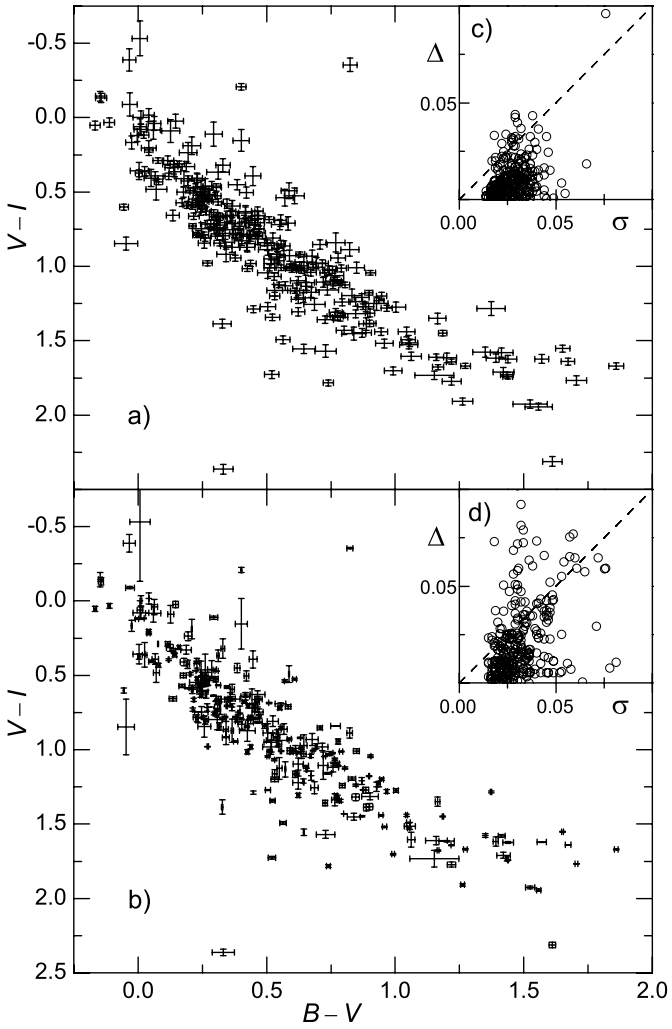

Fig. 1.12. The same as in Fig. 1.11, but $V-I$ vs. $B-V$ diagrams are plotted. Panel (c) is the same as in Fig. 1.11; in panel (d) $\Delta(V-I)$ vs. $\sigma(V-I)$ is shown.

HST by Krienke & Hodge (2007). They provide a catalog of BVI photometry (transformed from the *HST* to the Johnson-Cousins system) for 343 star clusters detected in the Wide Field and Planetary Camera 2 (WFPC2) images. Krienke & Hodge (2007) measured integrated magnitudes of star clusters through individual isophotal apertures. Note that the aperture size distribution, provided in their Fig. 7, peaks at $\sim 3''$ and is equal to a typical aperture diameter used for photometry of our cluster sample.

In total, 36 common objects were cross-identified in our and Krienke & Hodge (2007) studies. Differences of V (34 objects), $B-V$ (14) and $V-I$ (25) are shown in Fig. 1.13 vs. V magnitude. The error bars indicate photometric errors from Krienke & Hodge (2007); for objects without provided errors we assumed representative errors of V magnitude. Faint objects show a larger magnitude and color difference scatter. Two bright

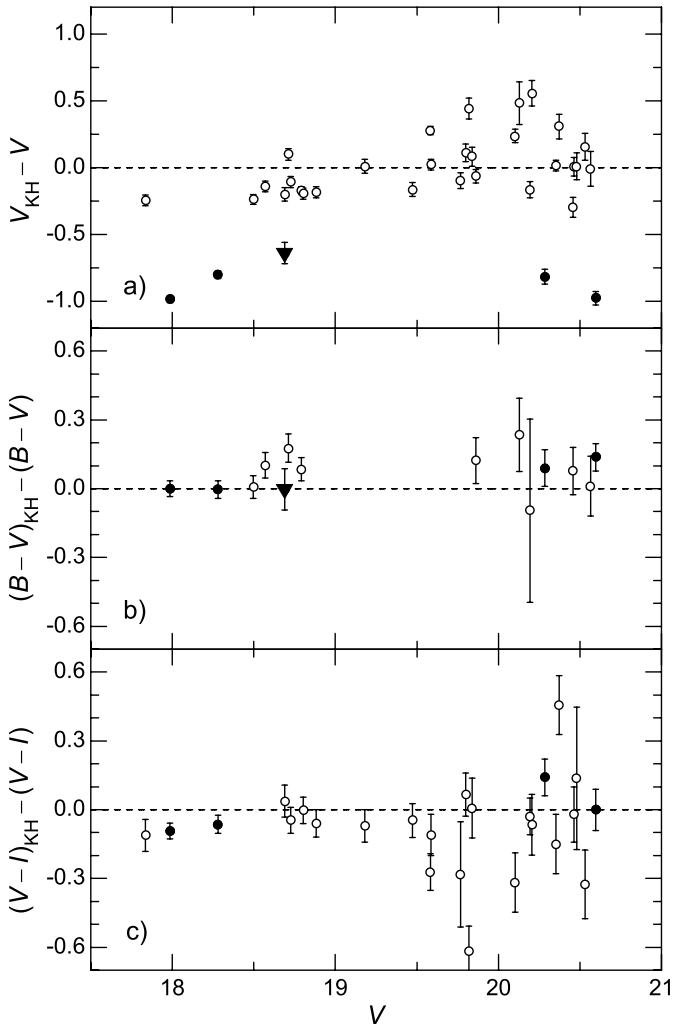

Fig. 1.13. Differences of V magnitudes and colors from Krienke & Hodge (2007) (marked with KH) and Narbutis et al. (2008) are shown for 34, 14 and 25 clusters in panels (a), (b) and (c), respectively. Error bars indicate photometric errors from Krienke & Hodge (2007). The deviations of V magnitudes of four objects (filled circles), residing in the same *HST* field, are presumably subject to zero-point inaccuracy. However, this does not affect their colors. A significantly smaller aperture size was applied in our study for a cluster marked by a filled triangle.

objects with $V \sim 14.3$ mag and $V \sim 15.7$ mag, not shown in Fig. 1.13, have V magnitude differences of 0.08 and 0.03 mag, respectively. Four objects, all residing in one *HST* field, have a significant V magnitude difference, presumably due to a zero-point inaccuracy. However, their colors do not show significant discrepancies. A much smaller aperture size was used in our study for the semi-resolved star cluster indicated by a filled triangle, however, the measured $B-V$ color matches well between both studies.

Color differences are shown as a function of colors in Fig. 1.14. Vertical and horizontal error bars show photometric errors from Krienke & Hodge (2007) and our study, respectively. The $B-V$ colors are mostly affected by blue contaminants and the $V-I$ colors – by red contaminants due to differing aperture centers, shapes and sizes. Different photometric background determination strategies used in both studies might also be responsible for

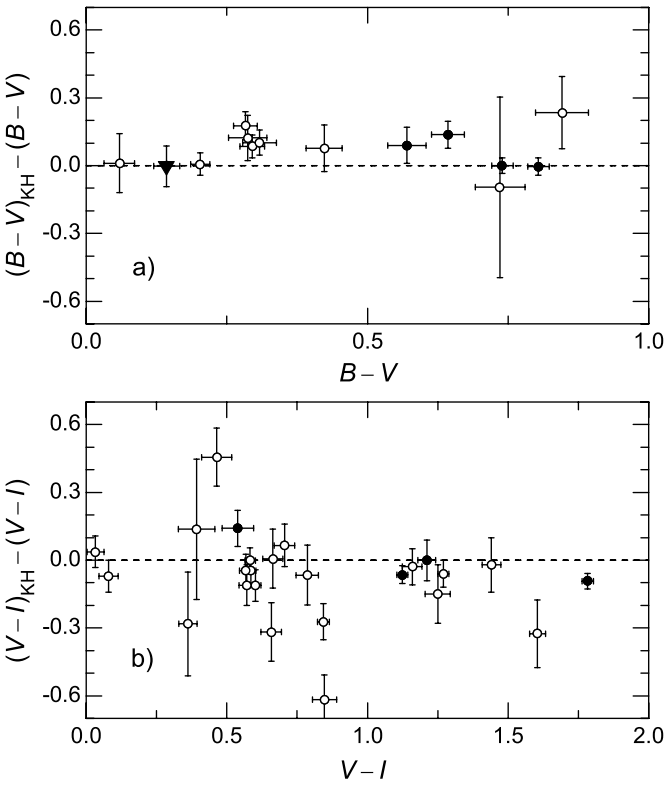

Fig. 1.14. The same as in Fig. 1.13, but color differences are plotted vs. corresponding colors. Vertical and horizontal error bars show photometric errors from Krienke & Hodge (2007) and Narbutis et al. (2008), respectively. Due to differing aperture centering, shapes and sizes used in both studies, the $B-V$ colors are predominantly affected by blue contaminants, and $V-I$ colors by red contaminants. Note that four objects, making a compact group in panel (a), $B-V \sim 0.3$, reside in one *HST* field. For description of the objects, shown by filled circles and a filled triangle, see Fig. 1.13.

the observed scatter. Note that four objects, shown in Fig. 1.14 (a) with $B-V \sim 0.3$, all reside in one *HST* field. Therefore, the difference of colors could be of systematic origin. Variable stars residing close to the studied objects might contaminate aperture magnitudes and colors, when observations from multiple epochs are compared. However, objects with the smallest error bars show a reasonably good match between LGGS and *HST* photometry data over a wide range of star cluster colors.

Photometric errors for 4% (for $U-B$), 7% (for $B-V$) and 21% (for $V-I$) of clusters are smaller than the errors arising due to the influence of contaminating background stars. The $U-B$ color of red objects tends to be systematically bluer (contaminated by blue stars), and an opposite effect is observed for $V-I$ of blue objects (contaminated by red stars).

We cross-identified 36 objects from our sample (LGGS) with the star clusters from Krienke & Hodge (2007, *HST)*. Despite different apertures (sizes, shapes and centering), photometric background determination and photometric calibration strategies used in both studies, V magnitudes and $B-V$, $V-I$ colors show a reasonably good agreement.

The aperture size test allows us to identify star clusters which have

integrated colors affected by background contaminants. The influence of background objects can be eliminated (to some degree) by measuring clusters through individually selected isophotal apertures on high-resolution images (e.g., *HST*; Krienke & Hodge 2007). However, the influence of contaminants, projected on star clusters within the applied aperture, can be estimated only statistically. Using ground-based (lower resolution) images for aperture photometry of faint star clusters it is difficult to avoid a strong contamination of colors by neighboring stars. Therefore, biases of the object colors have to be accounted for prior to deriving cluster parameters via a comparison of the observed colors with the SSP model data.

1.2.4 Catalog

The photometric catalog of 285 star cluster candidates up to $V \sim 20.5$ mag in the M31 southwest field is presented in Tab. 1.2, the full form of which is available in the electronic edition of Narbutis et al. (2008) available online[13]. Object coordinates, V passband aperture magnitudes, $U-B$, $B-V$, $V-R$, and $R-I$ colors with their photometric errors, a flag for 77 objects located in *HST* frames, and cross-identifications with Galleti et al. (2007), Krienke & Hodge (2007), and Kodaira et al. (2004) (69, 24, and 58 clusters, respectively) are provided.

All catalog objects, overlaid on the *Spitzer* 24 μm image, are shown in Fig. 1.1. Elliptical ring segments, indicating distances (6–18 kpc) from the M31 center in the galaxy's disk plane, were drawn.

V passband magnitude and $B-V$ color histograms of the catalog objects are shown in Fig. 1.6. Shaded histograms show a sub-sample of 77 objects identified in the *HST* frames.

Observed color-color diagrams of star cluster candidates, overplotted with SSP models of metallicity $Z = 0.008$ and ages ranging from 1 Myr to 15 Gyr, computed with PEGASE (Fioc & Rocca-Volmerange 1997), are presented in Fig. 1.7. Default PEGASE parameters and a universal initial mass function (Kroupa 2002) were applied. Reddening vectors are depicted by applying the standard extinction law: a V passband extinction to color excess ratio $A(V)/E(B-V) = 3.1$ and color excess ratios $E(U-B)/E(B-$

[13]M31 cluster photometry: `http://dx.doi.org/10.1086/586736`.

$V) = 0.72$, $E(R-I)/E(B-V) = 0.69$. The MW interstellar extinction in the direction of the M31 southwest field is $E(B-V) = 0.062$ (Schlegel et al. 1998).

Fig. 1.7 together with multi-band color maps suggest that the present sample covers a wide range of stellar populations, from old GCs through young massive clusters. Some objects, suspected to be young and heavily reddened in the $U-B$ vs. $B-V$ diagram, are displaced in opposite $R-I$ directions from the bulk of objects in the $R-I$ vs. $B-V$ diagram, introducing a large scatter. A detailed color analysis of these cases, taking into account multi-band color maps, reveals two main reasons: $R-I$ is increased due to an additional flux from red background stars in the I passband, and $R-I$ is decreased by an additional contribution from the Hα emission in the R passband.

Multi-band color maps (see Fig. 1.5) combined from LGGS (U, B, V, I, and Hα passbands), *GALEX* (NUV, FUV), 2MASS (J, H, and $K_{\rm s}$ passbands), *Spitzer* (24 μm), and HI (21 cm) images, are available in the electronic edition of Narbutis et al. (2008).

This catalog contains an almost complete homogeneous sample of target objects in the surveyed area and will serve as a basis for follow-up imaging or spectroscopic studies. The presented materials suggest that the sample in the catalog covers a wide range of stellar population – from old GCs through young massive clusters.

Tab. 1.2. *UBVRI* Photometry Data of the Star Cluster Candidates in the M31 Southwest Field.

ID[a]	α_{J2000}	δ_{J2000}	V[b]	$U-B$	$B-V$	$V-R$	$R-I$	σ_V	σ_{U-B}	σ_{B-V}	σ_{V-R}	σ_{R-I}	n[c]	Ap[d]	*HST*[e]	CrossID[f]
KW001.....	10.042834	40.607317	18.791	−0.259	0.295	0.306	0.450	0.012	0.022	0.022	0.016	0.025	3	3.2	W	1:BH02
KW002.....	10.044094	40.580988	19.963	0.197	0.636	0.473	0.524	0.016	0.027	0.025	0.022	0.028	3	3.0	W	...
KW003.....	10.045193	40.897594	19.575	−0.256	0.211	0.241	0.353	0.013	0.035	0.022	0.018	0.022	2	3.0	...	...
KW004.....	10.045684	40.603264	18.497	−0.419	0.203	0.222	0.268	0.013	0.031	0.017	0.017	0.017	3	3.0	W	2:37, 3:C01
KW005.....	10.049319	40.585042	19.467	−0.599	0.945	0.690	0.750	0.019	0.025	0.025	0.023	0.020	3	3.0	W	...

NOTES. R.A. and Decl. (J2000) coordinates of aperture centers are in the USNO-B1.0 catalog system (degrees). An entry "99.999" is for $R-I$ and σ_{R-I} of 5 objects saturated in the I passband images.

[a] ID number of the star cluster candidate.

[b] Aperture magnitude (note that it is not a total magnitude).

[c] Number of independent measurements in the LGGS fields F6–F9.

[d] Diameter of circular aperture or major axis length of elliptical aperture (arc-seconds). Elliptical apertures (ratio of minor to major axis; position angle of the major axis, calculated counterclockwise from the north direction) are used for objects KW102 (0.75; 120°) and KW141 (0.70; 30°).

[e] Identification of 77 objects in the *HST* instrument frames: W – WFPC2 (71); A – ACS (6).

[f] Cross identifications "catalog:id". (1) – The Revised Bologna Catalog of M31 GCs and candidates V.3.2, July 2007 (Galleti et al. 2007) – 69 objects. KW128 is identified with V203 and KW129 – with V202, however, coordinates are offset; KW271 and KW273 are identified as one object – G099. (2) – Krienke & Hodge (2007) "KHM31" numbers are given only for 24 objects not listed in (1). KW154 has two identifications: KHM31-79 and KHM31-80. (3) – Kodaira et al. (2004) "KWC" and "KWE" numbers are given for 58 objects. KW063 is identified with KWE09 and KW095 – with KWE19, however, center coordinates and apertures are slightly different.

Full version of table is available in Narbutis et al. (2008).

Chapter 2

Analysis Methods and Software

Here we present analysis methods and software developed to process wide-field mosaic images suitable for high precision photometry, to derive structural parameters of semi-resolved star clusters in crowded stellar field, and to determine evolutionary parameters of clusters based on their integrated broadband photometry.

2.1 Wide-Field Mosaic Image Reductions

2.1.1 Corrections of CCD Image Defects

Among various types of defects contaminating astronomical images, saturation of bright stars is yet unavoidable regardless of a wide dynamical range of modern CCD detectors. The well-known "blooming streaks" degrade image quality even in cases when CCDs with anti-blooming capability are used.

Although there are methods to perform photometry of saturated stars (see, e.g., Gilliland 1994; Maiz Apellaniz 2002), generally information present in the defected area, which may cover up to ∼5% of CCD, is lost. Since a defect has pixel values deviating significantly from its surroundings, a non-linear interpolation[1], used for combining images, expands the size of the defect making photometry impossible on a large area. This results in additional loss of information and can be avoided if defects are identified and removed in raw images prior combination.

Some saturated stars overlap in crowded fields, thus deblending might be considered, especially if PSFs of images will be homogenized to produce high quality color mosaics. In these cases defects should be treated properly in individual images prior to stacking. However, image corrections require time consuming interactive work and an automated procedure is necessary.

[1]Commonly used sinc function, $\sin(x)/x$, produces extended moire pattern around "blooming streaks" of saturated stars.

We have developed a program tool, StarL, designed for automatic detection and correction of CCD image defects. The program is specifically targeted for "streaks" of saturated stars and genetic algorithm based on restoration of their "cores" in crowded fields. StarL was successfully applied for Suprime-Cam images and may be implemented in the data processing pipe-lines to produce defect-free images suitable for stacking and making of wide-field color mosaics. Here we describe the algorithm implemented in the StarL, evaluate its performance, and compare with analogous programs. The source code and examples are available at the StarL website[2].

There are numerous types of image artifacts and defects[3], which originate due to faults in CCD or observing conditions. They can be classified as: (1) CCD defects, e.g., bad pixels/columns; (2) "random" defects, e.g., cosmic rays, meteor/satellite tracks; (3) saturated stars. A bad pixel mask can be constructed to indicate defects intrinsic to the CCD detector and be used for science image correction of the entire observing run. If multiple dithered exposures are stacked, bad pixel rejection procedure can be used to eliminate "random" defects, however, saturated stars will remain in the stacked mosaic, unless the camera position angle is changed for every exposure.

The StarL algorithm follows assumptions based on the CCD design, which should be reasonable for images in optical and near-infrared wavelengths: (1) pixel values above the detector linearity limit are saturated and unreliable; (2) "streaks" are elongated along the read-out direction; (3) images are bias subtracted and flat-fielded.

The block-scheme of StarL is shown in Fig. 2.1. The program loads input image and CCD bad pixel mask, and reads configuration parameters – lower and upper linearity limits of the detector, *datamin* and *datamax*, which are used to identify bad pixels. The standard deviation of image pixel values, σ, is determined by selecting good pixels within this range.

The image defects are defined as pixels outside the range (*datamin*, *datamax*) or marked in the optionally provided CCD bad pixel mask; they

[2]StarL: `http://www.astro.ff.vu.lt/software/starl/`.

[3]Examples of image defects: `http://www.eso.org/~ohainaut/ccd/CCD_artifacts.html`.

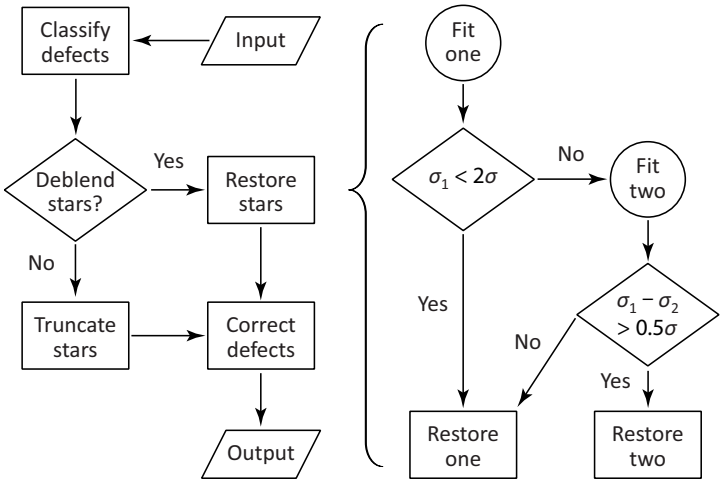

Fig. 2.1. A block-scheme of the StarL algorithm (left) and procedure to restore "cores" of saturated stars (right).

all are indicated in the defect map by the program internally. This map is analyzed to select spatially connected structures and, based on their morphology, to classify pixels into the following categories: (1) "cores" of saturated stars; (2) "streaks" of saturated stars; (3) other bad pixels.

The morphological classification starts with an assumption that a defect with pixel values larger than *datamax* is a saturated star with "streaks". The width, w_X, and the height, w_Y, of the defect are measured, while its center coordinates, $(x_0,\ y_0)$, are set where w_X reaches maximum value. Pixels inside a circle of radius $r_C = w_X/2$, placed at the defect's center, are assigned to the "core" of saturated star, while pixels outside of the "core" – to the "streaks" of saturated star.

Our tests with Suprime-Cam images show that this procedure allows to robustly identify saturated stars. Morphological classification can identify "cores" of two saturated stars if they are aligned "vertically" and their "streaks" are overlapping. In case when two overlapping saturated stars aligned "horizontally", only one "core" is identified initially, however, deblending is successfully used to resolve this case.

If a defect is elongated "horizontally", i.e., $w_X > 2w_Y$, or has pixel values less than *datamin*, or is indicated in the CCD bad pixel mask, it is assigned to the category of "other bad pixels".

Although it is fast and performs reasonably well in sparse stellar fields, morphological analysis of the defect map allows to reliably identify positions of single saturated stars only. In crowded fields, however, saturated stars overlap and have to be deblended. StarL performs deblending by fitting a

one component star model to the data and then, depending on the scatter of the residuals, by fitting a two component model (see Fig. 2.1).

A rectangular sub-image of $(w_X + 5) \times (w_X + 5)$ in size centered on the "core" of saturated star, (x_0, y_0), is used to fit a star model to pixels which are not saturated, i.e., outside of the "core" and "streaks". A one component model consists of a circular Gaussian or Moffat function defined in the image by the center coordinates (x, y), the FWHM, p, and the central height, I, plus the flat sky background, I_{sky} – five free parameters in total. A two component model consists of two Gaussian or Moffat functions plus sky background – nine free parameters.

We use PIKAIA[4] genetic algorithm (Charbonneau 1995) to extensively search the free parameter space. PIKAIA fits a model to data by generating a variety of star models with parameters (x, y, p). For every model the central height, I, and the sky background value, I_{sky}, are determined by singular value decomposition routine. Tests show that PIKAIA finds the best solution by computing $\sim 2 \times 10^4$ models converging close to the point of the global minimum, unless saturated star is located at the image's edge. Default PIKAIA parameters were found to be the best suited for this problem.

The standard deviation of pixel values computed on the residual sub-image after subtracting the best fitted single component model, σ_1, is compared to the standard deviation of the image, σ. If $\sigma_1 > 2\sigma$, a two component model fitting is attempted. In this case $\sim 5 \times 10^4$ models are usually computed by PIKAIA to find the best solution. If the standard deviation computed after subtracting the two component model, σ_2, is significantly smaller than σ_1, i.e., $\sigma_1 - \sigma_2 > 0.5\sigma$, the two component model is used for image correction, otherwise the single component model is applied. Users can choose the threshold to switch between one or two component models.

To ensure accurate image correction results, the best fitted model is accepted if: (1) $I > I_{sky} + 3\sigma$ is determined, allowing to identify unsaturated stars in the close vicinity to the saturated ones; (2) FWHM of the fitted model is in the range of 1–10 pixels, allowing variable PSF across the image and taking into account saturated background galaxies as well.

[4]PIKAIA: `http://www.hao.ucar.edu/modeling/pikaia/pikaia.php`.

We have simulated overlapping saturated stars with the SkyMaker program[5] (Bertin 2009) to examine the performance of StarL in deblending saturated stars. StarL can resolve two overlapping stars of magnitude difference up to ∼2 mag if distance between their centers is larger than 0.5 of the stellar FWHM. Although it is time consuming, use of the genetic algorithm to deblend saturated stars ensures unbiased fitting of the parameters avoiding to be trapped in local minima of the parameter space.

The best fit model of saturated star is used to replace its "core" and is smoothed with Gaussian filter of 3×3 pixels in size to ensure continuity between the data and the model. If the user rejects to use deblending, the "cores" of saturated stars are simply truncated at the $I = datamax$ limit and smoothed with Gaussian 5×5 pixels filter to avoid sharp jumps of pixel values.

Once the "core" of the saturated star is restored, the "streaks" are corrected. If the pixel in the "streak" is within a distance of $4 \times r_C$ from the star center, it is replaced by a median value calculated in a circular annulus of 3 pix in width, centered on the saturated star. This procedure ensures that bad pixels located nearby to the saturated star, which are affected by the star "wings" and have values higher than sky background, are replaced by smoothly decreasing values to the background sky level as going further away from the star.

For pixels located further than $4 \times r_C$ from the star center and classified as "streaks" or "other bad pixels", a median value computed in a rectangular box is substituted. Finally, for all pixels, which were introduced in the defect map and corrected, the Gaussian noise of σ, characteristic to the standard deviation of image pixel values, is added.

StarL program is written in the C++ language and can be compiled under the UNIX/Linux systems. The configuration file, which contains user-defined parameters, and, optionally, a CCD bad pixel mask have to be passed to the program together with the FITS image to be corrected. The output of StarL is a corrected image and a defect classification map, which can be used as a bad pixel map for photometry.

The StarL program recognizes all data types of FITS files, performs

[5]SkyMaker: `http://www.astromatic.net/software/skymaker`.

calculations using double type variables, and writes corrected image to the file of the same data type as it was at the input; CFITSIO[6] routines are used for this purpose. For random number generation and singular value decomposition routines we use the GNU Scientific Library[7].

There are several CCD image processing programs of different sophistication level capable of removing bad pixels/columns, satellite/meteors tracks and cosmic ray hits. These "random" defects can be neglected in wide-field surveys, typically producing sets of five or more dithered exposures, since defects vanish when median or sigma-clipping algorithm is used for image stacking. However, based on the tests with Suprime-Cam data, we recommend to remove saturated "random" defects before image distortion corrections are made.

"Streaks", which are not removed by stacking, can be corrected by using the programs, e.g.: (1) Mira[8] – proprietary, interactive supervision is necessary; (2) EyE[9] – requires training of neural-network based algorithm; (3) PIXY System 2[10] – limited to non-overlapping saturated stars. Restoration of the "cores" of saturated stars is implemented in the *Spitzer* telescope data processing pipeline (Schuster et al. 2006), but it relies on external stellar catalog to identify candidates for saturation.

To process images of Local Group galaxies obtained with the Suprime-Cam, we have developed StarL – a stand-alone program for correction of saturated stars and other defects. It is assumed that individual images are going to be stacked, i.e., "random" defects, like cosmic rays, will be rejected by a median algorithm. The fast and simple defect detection algorithm is based on the analysis of spatial structures in the map of saturated pixels. The genetic algorithm used for deblending of the saturated stars ensures robust and accurate performance even in crowded fields.

Here we list some image examples based on the Suprime-Cam observations, illustrating the need to apply StarL:

[6]CFITSIO: `http://heasarc.nasa.gov/fitsio/`.

[7]GSL: `http://www.gnu.org/software/gsl/`.

[8]Mira: `http://www.mirametrics.com/`.

[9]EyE: `http://astromatic.iap.fr/software/eye`.

[10]PIXY System 2: `http://www.aerith.net/misao/pixy/`.

- The southwest field of the M31 galaxy[11] by Kodaira et al. (2004) is a good example of crowded field with superimposed bright stars of the MW. The image with "streaks" removed was produced for star cluster analysis in Narbutis et al. (2008) and Vansevičius et al. (2009).
- The wide-field mosaic of the Leo A galaxy[12] by Vansevičius et al. (2004) was created using software package SDFRED by Yagi et al. (2002), dedicated to the Suprime-Cam data.
- The wide-field mosaic of the M33 galaxy[13] covers a $100' \times 65'$ field of variable crowding and is based on ∼2000 individual images, processed with StarL without restoration of the "cores" of saturated stars.

StarL highly reduces the amount of time and work necessary to correct defects in CCD images and can be used as a stand-alone program or can be implemented in the wide-field survey data processing pipelines to produce defect-free color mosaics. It was used to process images for creation of multi-band (Fig. 1.5) images of M31 star cluster sample in this study.

2.1.2 Coordinate System

Once individual images are bias subtracted, flat-fielded and, optionally, processed with StarL to remove image defect, they have to be registered to the common coordinate system, which would allow object cross-identification and image stacking to produce mosaics.

For object cross-identification between images of different Suprime-Cam CCDs, exposures, and passbands, their positions in an image, (x, y), should be first transformed to a global coordinate system, (X, Y). For ground-based observations with typical FWHM $\sim 1''$, the coordinate transformation error of $\lesssim 0.2''$ is imperative. In many wide-field surveys (e.g., Massey et al. 2006) it was common to find an astrometric solution for individual CCD images based on bright astrometric standards, and then to perform such cross-identification of objects in the sky coordinate system, (α, δ).

We refused this approach, however, due to considerable distortions of Suprime-Cam images, which cannot be corrected empirically due to a lack of sufficient number of astrometric standards in the USNO-B1.0 catalog,

[11] M31: `http://subarutelescope.org/Pressrelease/2001/09/07/`.

[12] Leo A: `http://subarutelescope.org/Pressrelease/2004/08/05/`.

[13] M33: `http://subarutelescope.org/Pressrelease/2009/01/22/`.

most of which were saturated in our "long" exposure images. Instead, we adopted the SDFRED (Yagi et al. 2002) software package to create a reference stacked V passband mosaic image and then to find transformation equations from each image, (x, y), to the pixel coordinate system of the mosaic, (X, Y), fitting individual transformation equations for each image.

The SDFRED automatically corrected image distortions according to the prescription from the optical ray-tracing of Suprime-Cam and differential atmospheric refraction dependence on airmass (Miyazaki et al. 2002). By relying on the approximate astrometric information written into FITS headers during observations, the SDFRED searched for the overlapping pairs of distortion corrected images. Relative shifts and rotations in a set of image pairs was computed by cross-correlating accurately determined center coordinates of bright objects.

Resulting matrix of relative shifts/rotations of all image pairs was then used to find a solution for positions of all individual images in respect to the arbitrary selected image in the center of the survey field. The accuracy of $\lesssim$1.5 pix ($0.3''$) was achieved by this procedure between different passbands and exposures, but it was still not suitable to cross-identify objects accurately enough for a photometric catalog. Since these positional errors were smaller than the typical stellar FWHM $\sim 0.8''$, the center coordinates of objects in the stacked mosaic could be measured accurately despite possible relative shifts of individual images before stacking, i.e., in this case the sum of shifted PSFs results in a broader PSF with a single center.

Therefore, we performed stacking of distortion corrected images to make a reference V passband[14] mosaic, defined its pixel coordinates as a global coordinate system, (X, Y), and created a list of reference objects detected there. Lists of objects from the original[15] images were cross-identified with a reference list. Using IRAF's `geomatch`, we have computed coordinate transformation equations, $T(x, y)$, for each image by interactively fitting 5^{th}-order polynomial to a sample of points distributed uniformly over an image, i.e., $(x, y) * T(x, y) \rightarrow (X, Y)$. This procedure improved the accuracy of coordinate match between different passbands and exposures, leaving

[14]Blue and red objects should be detected in V passband.

[15]Without distortion correction.

residuals of $\lesssim$0.4 pix (0.08″). Therefore, we adopted an upper limit of 2 pix (0.4″) for coordinate difference in object cross-identification.

The astrometric World Coordinate System (WCS) solution of the reference V passband mosaic was derived by cross-correlating a list of reference objects with the USNO-B1.0 catalog of standard astrometric stars using IRAF's `ccmap`. Since this mosaic, stacked with the SDFRED, was in the tangential sky projection, only linear terms were needed. The fitting was performed by iteratively removing outliers and resulted in ∼150 uniformly distributed stars used to fit astrometric solution; the rms was ∼0.2″. The pixel coordinate system of the reference mosaic, (X, Y), was tied to the equatorial sky (J2000) coordinate system, (α, δ), and mosaic FITS header was updated to include this information.

2.1.3 Global Photometric Solution

Since the telescope was dithered between exposures, the same object was measured in several individual images, in some cases obtained with different CCDs. This allowed to perform an internal calibration of photometry over the survey field using "overlapping" stars, and to take into account different CCD sensitivities and variable atmospheric transparency between exposures.

It is known that wide-field cameras have vignetting effects and accurate flat-fielding is necessary to ensure a uniform response of the detector across the field. In some cases even flat-fielding based on multiple measurements of stars is required to derive a photometric zero-point correction map for mosaic camera, which has coordinate-dependent variation of typical amplitude of ∼0.05 mag (see, e.g., Magnier & Cuillandre 2004, and references therein).

Therefore, dithering of telescope with offset more than half the field of view away from central position and even rotating camera are very helpful to obtain such map. Ideally, one would like to have a set of multiple overlapping observations and to apply a technique similar to the one presented by Padmanabhan et al. (2008) used for the internal calibration of SDSS photometry.

In case of Suprime-Cam M31 survey, such correction map could not be

derived due to small relative shifts between exposures, therefore, we have used a photometric calibration procedure to derive relative zero-points of individual CCD images based on aperture photometry of bright isolated stars.

Having measured instrumental magnitude, $m_{j,o}^{\rm total}$, of object, o, in image, j, we obtain a global photometric solution for the whole image set of the survey field, i.e., find a set of zero-points, z_j, for all images, j, of the same passband. Therefore, a global minimum of sum, $\sum_{j,k}\sum_o(m_{j,o}^{\rm total}+z_j-m_{k,o}^{\rm total}-z_k)$, over all possible image overlaps, (j,k) and over all cross-identified stars, o, in the overlap, is found.

While the accuracy of the determined z_j depends on the number of stars used, for practical purposes, however, only objects with small photometric errors, $\sigma \lesssim 0.05\,$mag, were used. Also, one of the zero-points of the arbitrary selected image (in the center of mosaic) is fixed, e.g., $z_1 = 0\,$mag, and calibrated later using local photometric standards.

We note that the global photometric solution and coordinate-dependent linear transformation equations for zero-points were based on analysis of single passband photometry, i.e., without taking into account color equations, since this would complicate the procedure. The quantum efficiency curves of individual CCDs (Miyazaki et al. 2002) differ only by 3–4% and make this procedure reasonable.

2.1.4 Image Stacking

The defect-free stacked mosaic images, suitable for object identification and photometry, were created by the following procedure:

1. Individual "long" exposure images were processed with StarL software program, which performed automatic correction of CCD image defects, e.g., "blooming streaks" of saturated stars were replaced by surrounding background pixel values and their truncated cores – by Moffat function. It produced corrected images without any sharp jumps of pixel values (except for cosmic ray hits, which were removed by median stacking), and their bad pixel masks.
2. Photometric background was determined for each image from histograms with IRAF's `imhist` and was subtracted. Using the relative

sensitivities of CCDs and exposures determined, we have multiplied image pixel values to homogenize the registered flux.

3. Images were transformed/resampled to the pixel coordinate system, (X, Y), of the reference V passband mosaic using IRAF's `geotran` and adopting sinc interpolation to ensure that PSF and image noise statistics are preserved well. Resampled images are in the tangential sky projection and have uniform scale of $0.2''\,\mathrm{pix}^{-1}$.
4. Images of the same passband were stacked with IRAF's `imcombine` using median to reject cosmic rays and meteor tracks. Non-photometric areas in the mosaic are indicated by combined bad pixel masks. The typical FWHM of mosaic images is $0.8''$.
5. Flux calibration of mosaic images was performed and magnitude zero-point information is provided in FITS headers. Note that they can be used for crude calibration only, since color dependence of CCDs is not taken into account. Image WCS is in USNO-B1.0 (J2000) coordinate system.

We note that degraded PSF quality due to stacking of slightly different PSF shapes has little influence on photometric accuracy of star clusters and determination of their structural parameters. Additionally, stacked mosaic is free of defects and the S/N of objects is enhanced.

2.1.5 PSF homogenization

LGGS mosaic images (Massey et al. 2006) of different passbands employed for aperture photometry of star clusters have different widths of stellar PSF. FWHM ranges from $0.7''$ to $1.3''$ (pixel size is $0.27''$; see Tab. 1.1). Four mosaic images have coordinate dependent PSFs with FWHM varying more than $0.2''$ and reaching maximum of $0.3''$ for the field's F7 I passband mosaic image.

Consequently, this could lead to variable aperture corrections and star cluster color bias when measured with aperture sizes as small as $\sim 3''$ used here. Therefore, we applied the DAOPHOT package (Stetson 1987) of IRAF to compute PSF for every mosaic image. The widest PSF (FWHM = $1.3''$) was convolved with the Gaussian kernel producing the reference PSF of FWHM = $1.5''$. IRAF's `psfmatch` was employed to compute required

convolution kernels for individual mosaic images in respect to the reference PSF. The kernels were symmetrized by replacing cores with the best fitting Gaussian profiles, and the kernel wings with the best fitting exponential profiles truncated at 3.5″.

IRAF's `convolve` was employed to produce mosaic images possessing the unified PSF (FWHM = 1.5″). Finally, we achieved uniform and coordinate-independent PSF across all convolved images. The maximum difference of the aperture corrections among different photometric passband and observed field mosaic images is less than 0.02 mag. A test of photometric accuracy of the entire PSF homogenization procedure suggests that errors do not exceed 0.01 mag. The convolved images were photometrically calibrated and used for star cluster photometry.

2.1.6 Photometric Standards

The interpretation of star cluster photometry via SSP model fitting relies primarily on the accuracy of photometric calibration. Therefore, we compared stellar photometry data in the southwest field of the M31 disk published by Magnier et al. (1992, hereafter Mag92), Mochejska et al. (2001, hereafter Moc01) and Massey et al. (2006, hereafter Mas06) as the local photometric standards for the calibration of star cluster aperture photometry.

The area selected from Mag92 for our investigation is bounded by the following J2000.0 coordinates: right ascension from $0^{\rm h}39^{\rm m}57.5^{\rm s}$ to $0^{\rm h}42^{\rm m}26.5^{\rm s}$ and declination from 40°32′24″ to 41°04′12″ ($\sim 28' \times 32'$), covering parts of the fields F7 and F8 from Mas06, the area of this study, and the field F from Moc01 (see Fig. 2.2 for area limits).

The Mag92 and Moc01 photometry data were taken from the VizieR[16] catalog service (Ochsenbein et al. 2000). The Mas06 catalog was taken from their Tab. 4.

The typical seeing (FWHM) of the published photometric data were as follows:

- Mag92 – 2.3″ (from 1.4″ to 4.0″);

[16] VizieR: `http://vizier.u-strasbg.fr/`.

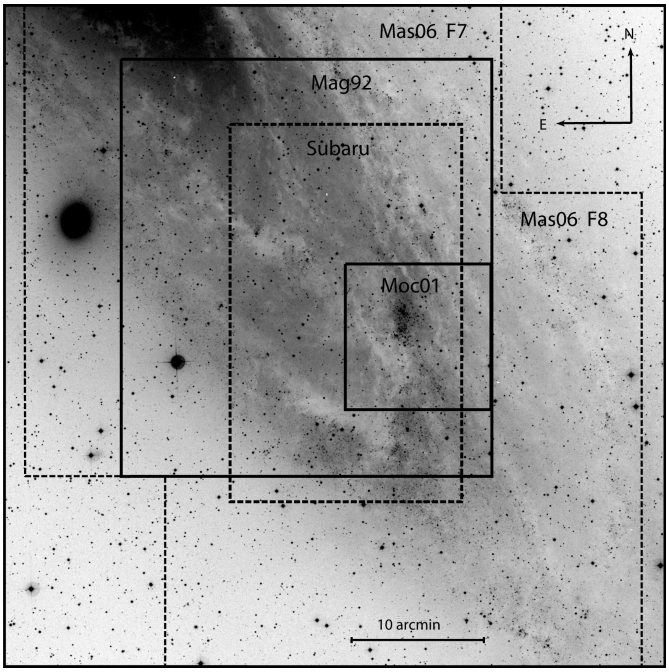

Fig. 2.2. Southwest area of the M31 galaxy disk (DSS B passband image) with indicated fields under consideration. "Subaru" marks the field of this study.

- Moc01 – 1.0″ in V passband, 1.1″ in I passband and 1.7″ in B passband;
- Mas06 – 1.0″ (from 0.8″ to 1.4″).

The selection criteria of stellar objects from the compared catalogs were as follows:

- Mag92 – photometric error <0.06 mag in V passband and <0.08 mag in B and I passbands, at least two observations in each passband available and the object is classified as a star;
- Moc01 – photometric error <0.05 mag in each passband and variability index $Js < 1.5$ (Stetson 1996);
- Mas06 – photometric error <0.015 mag, at least four observations in each passband available and faint magnitude limit $V = 19.5$ mag.

Systematic object coordinate differences of Mag92, Moc01 and Mas06 data sets exceeding 1″ were found by examining regions, overplotted on the F7 field mosaic image from Mas06. IRAF's `geoxytran` procedure was used for nonlinear transformation of the object coordinates given by Mag92 and Moc01 to the Mas06 field's F7 V passband mosaic image coordinate system. Finally, we achieved well matching (<0.2″) homogeneous coordinate systems of all three datasets and cross-identified the stars. Maximum object

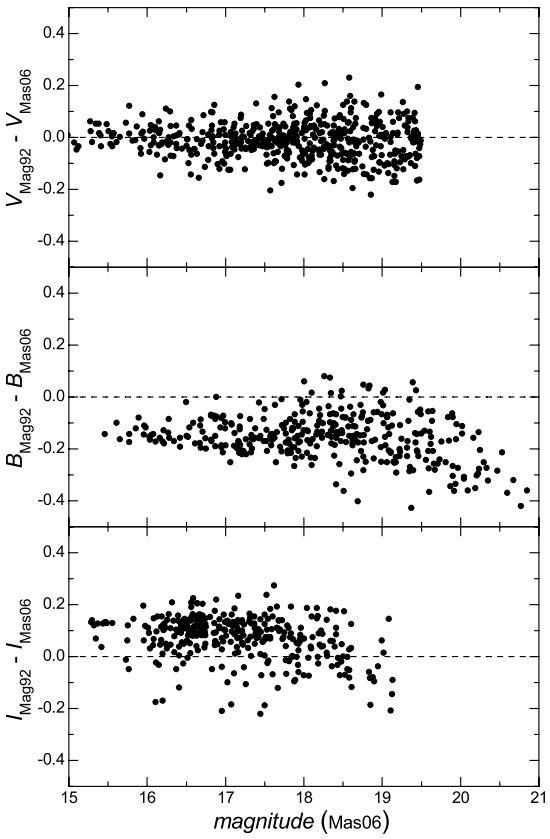

Fig. 2.3. Differences of B, V and I magnitudes from Mag92 and Mas06 plotted vs. corresponding magnitudes from Mas06.

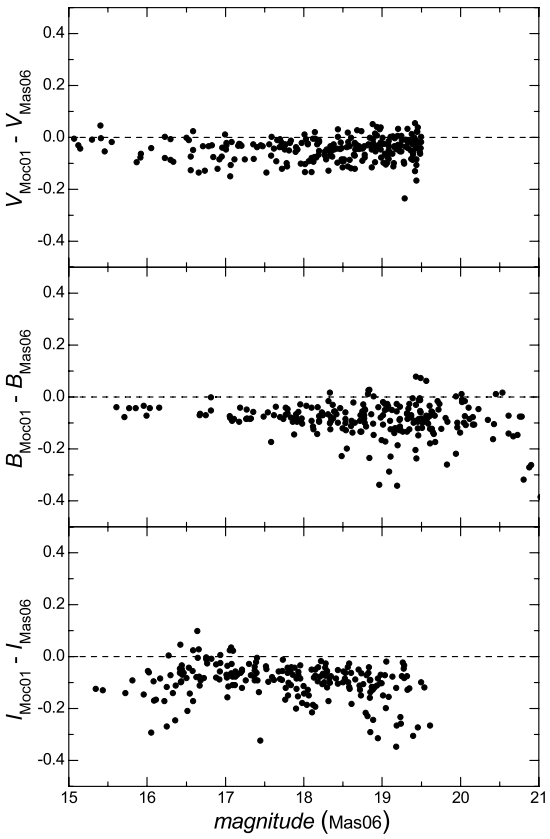

Fig. 2.4. Differences of B, V and I magnitudes from Moc01 and Mas06 plotted vs. corresponding magnitudes from Mas06.

coordinate deviations of $0.5''$ and $0.7''$ were allowed for Moc01 and Mag92 star identification with the Mas06 dataset, respectively.

The selection criteria and star coordinate matching limits applied predetermined the final data sets used for further photometry comparison consisting of: 343 and 336 stars from Mag92 possessing $B-V$ and $V-I$ colors, respectively (Fig. 2.3), and 233 and 213 stars from Moc01 possessing $B-V$ and $V-I$ colors, respectively (Fig. 2.4). In the next section we show and briefly discuss the B, V, and I magnitude and color differences (Mag92 and Moc01 minus Mas06) vs. corresponding magnitudes and colors from Mas06.

Initially we tested the coordinate dependence of magnitude and color differences of datasets Mag92 and Moc01 vs. Mas06. The Moc01 photometric data obtained with a single CCD and covering a rather small field of $11'\times11'$ show no systematic differences larger than 0.05 mag. The Mag92

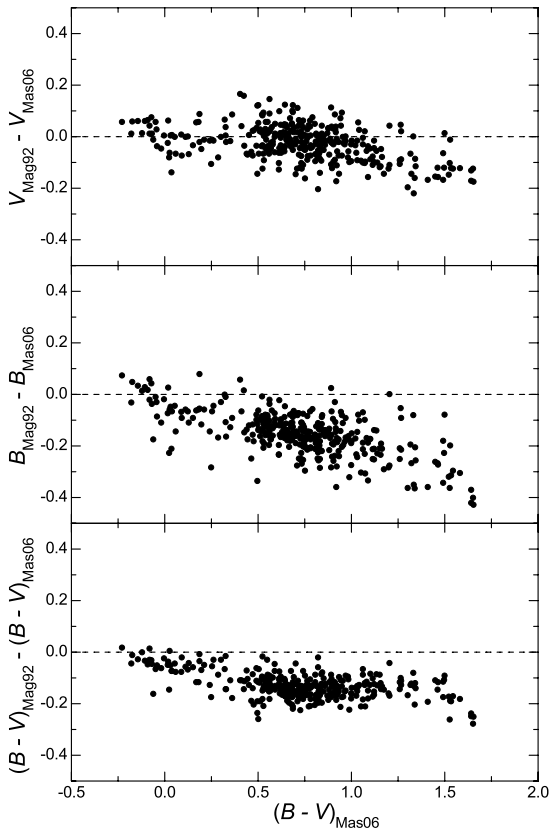

Fig. 2.5. Differences of B and V magnitudes and $B - V$ colors from Mag92 and Mas06 plotted vs. $B - V$ from Mas06.

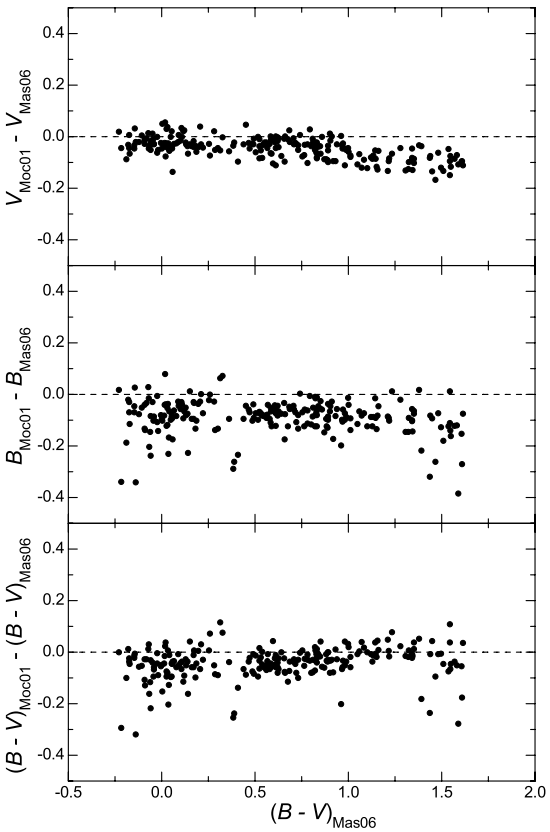

Fig. 2.6. Differences of B and V magnitudes and $B - V$ colors from Moc01 and Mas06 plotted vs. $B - V$ from Mas06.

data were obtained with a CCD of a small size field-of-view ($6.5' \times 5.7'$), and our comparison area (see Fig. 2.2) contains $\sim$20 different Mag92 fields. However, we notice only one break in $V - I$ color differences and it is less than 0.1 mag. Relatively small coordinate dependencies of magnitude and color differences do not alter significantly the results presented in Figs. 2.3–2.8.

As it can be easily seen in Figs. 2.3 & 2.4, V passband magnitude data are well calibrated and show no significant zero-point deviations. However, large systematic discrepancies of the Mag92 and Moc01 zero-points with respect to Mas06 are obvious for B and I magnitudes. This effect, most probably, occurs because of $B - V$ and $V - I$ color reduction inaccuracy due to considerable color equations of the instrumental systems and narrow color range of the standard stars used.

The differences of magnitudes and colors of the Mas06 and Mag92 from

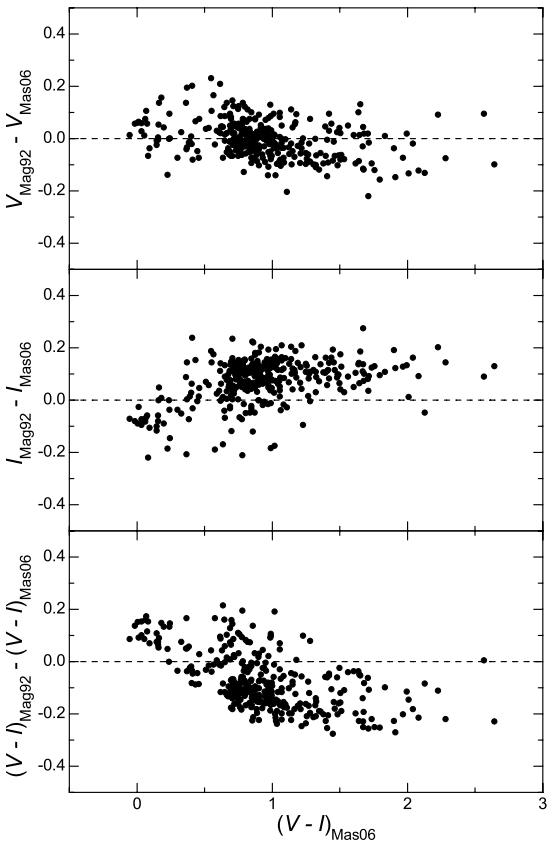

Fig. 2.7. Differences of V and I magnitudes and $V-I$ colors from Mag92 and Mas06 plotted vs. $V-I$ from Mas06.

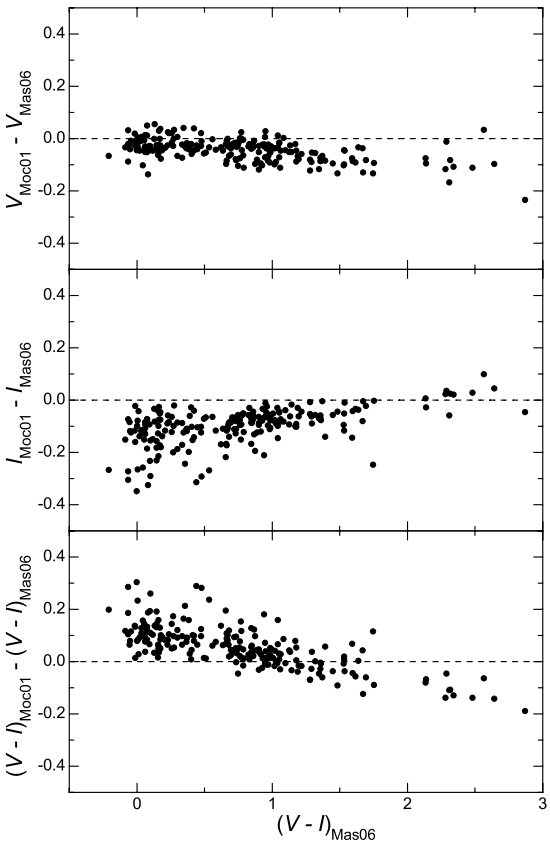

Fig. 2.8. Differences of V and I magnitudes and $V-I$ colors from Moc01 and Mas06 plotted vs. $V-I$ from Mas06.

one side and of Moc01 from the other side (plotted vs. $B-V$) are shown in Figs. 2.5 & 2.6. Corresponding plots vs. $V-I$ are shown in Figs. 2.7 & 2.8. These plots confirm the above-stated assumption about color equation determination difficulties and strongly imply that even carefully calibrated CCD photometry cannot guarantee reliable photometric data suitable, e.g., for star formation history analysis even in such a well-studied galaxy as M31.

Kaluzny et al. (1998) discussed the discrepancy and nonlinearity of their $V-I$ colors in respect to Mag92 data. We show that this discrepancy is easily seen in Fig. 2.7 as well, where Mag92 and Mas06 photometric data are compared. However, $V-I$ colors of Moc01 also show large systematic deviations from Mas06. In both cases, huge color deviations, as large as $\sim$0.3 mag, can hardly be accounted by color equation, crowding and seeing or non-photometric weather effects.

The surprisingly large magnitude and color differences between the care-

fully calibrated Mas06, Mag92 and Moc01 catalogs found here suggest that users should be cautious using the published photometric data as local photometric standards for calibration of the new photometry.

Solely on the ground of Figs. 2.3–2.8 it is rather difficult to decide which of these three datasets is the most reliable. The careful reduction and calibration method used by Massey et al. (2006), as well as internal consistency check of overlapping fields, makes us believe that this is the most accurately calibrated photometry dataset in the M31 galaxy to date.

2.1.7 Photometric Calibrations

We carefully selected well-isolated stars from Massey et al. (2006) Tab. 4 for calibration of the *UBVRI* magnitudes of LGGS images with homogenized PSFs. The selection criteria were as follows: the photometric error $\sigma < 0.03$ mag and the number of observations >3 in each passband. The total fluxes of the calibration stars were measured by employing IRAF's `phot` through a circular aperture of $3.0''$ in diameter and by applying the same aperture correction of 0.27 mag for all mosaic images.

Massey et al. (2006) in Tab. 2 provide color terms for individual CCD chips of their mosaic camera and color equations. We solved those equations by fitting photometric zero-points for every individual CCD chip of the mosaic images. Typically 80 (ranging from 20 to 140) calibration stars per chip were used. The final errors of the derived zero-points are less than 0.01 mag with typical fitting rms <0.03 mag for the *I* passband and <0.02 mag for other passbands.

Color equations given by Massey et al. (2006) supplemented with derived zero-points were used to transform instrumental magnitudes to the standard system. For objects located in the mosaic image areas combined from different CCDs, we used color equations of corresponding CCDs and performed independent transformations to the standard system.

A comparison of three published stellar photometry data sets in the southwest field of the M31 disk suggests caution when using tertiary standards as local photometric standards. However, a careful reduction, calibration, and internal consistency check performed by Massey et al. (2006) resulted in millimagnitude differences between the photometry results of

overlapping fields. To our knowledge, this is the most accurately calibrated photometry data set in the M31 galaxy.

2.2 Determination of Structural Parameters

The structure properties of MW GCs can be studied accurately due to a large number of stars and low background contamination. Derivation of structural parameters of MW OCs is complicated by statistical subtraction of background, unless stars are selected by their motions. For more distant star clusters, depending on the image resolution, only photometry of individual stars can be obtained, transiting to semi-resolved clusters, where the core of the object is unresolved due to seeing effects, and finally – to unresolved extragalactic star clusters, observed as extended point sources even with *HST*.

Star cluster candidates of our sample are unresolved or semi-resolved objects in the ground-based images, most of them are projected on the crowded disk of M31. Therefore, background and/or cluster's own bright stars (hereafter contaminants) are superimposed on cluster's surface brightness distribution. Consequently, the structural parameters of cluster derived by a direct fit of analytical model to such data are biased due to contaminants. To avoid this, we have developed a method to derive structural parameters of contaminated star clusters by including contaminants as point sources in a structure model fitting process.

Usually the surface brightness distribution of star cluster is well described by radial surface brightness profile of circular/elliptical tidal-cut-off King King (1962) and power-law EFF Elson et al. (1987) models. The most accurate fits of structure models are obtained for clusters resolved into individual stars and superimposed onto uniform background.

The assumption that stars are point sources of same luminosity is essential for fitting King/EFF models to unresolved star clusters. It is broken for low-mass young objects, where individual bright star dominate the luminosity profile. If cluster is projected onto the crowded field, e.g., OB association, individual stars additionally contaminate the observed surface brightness distribution.

A program ISHAPE developed by Larsen (1999) to determine structural

parameters of star clusters has been successfully applied in various studies of unresolved extragalactic star clusters based on *HST*. It uses a down-hill simplex minimization, starting from given initial parameters, to search for the best fit solution of model, and can mask out regions of cluster, significantly deviating from the model fit.

Employing ISHAPE in our study of semi-resolved clusters in the M31 galaxy, we have found two possibilities to improve this algorithm: (1) masking of deviating pixels should be replaced by simultaneous fitting of resolved stars, since a bright star, superimposed onto the compact cluster (i.e., $\mathrm{FWHM_{PSF}}$ is comparable to the FWHM of cluster), cannot be simply masked out; (2) the sensitivity to the initial parameters of fitting can be overcome if down-hill simplex, which usually gets trapped in the local minima, is replaced by PIKAIA (Charbonneau 1995) genetic algorithm to extensively search the free parameter space.

2.2.1 FitClust Algorithm

We present a new structure model fitting program tool, FitClust, designed to derive structural parameters of extragalactic star clusters, with emphasis on closely modeling their observed semi-resolved surface brightness distributions.

This algorithm improves previous techniques by: (1) being able to fit a star cluster model with arbitrary number of free parameters and simultaneously accounting for individual contaminating stars; and (2) using genetic algorithm to extensively search the free parameter space for a global solution. Star cluster is modeled by smooth King or EFF surface brightness distribution, observational effects are taken into account by convolving the model with a PSF, while individual resolved stars are modeled with a plain PSF. The extensive free parameter space is searched using a genetic algorithm, which provides the global solution.

FitClust program tool is written in Fortran 77, the wrapper with Python and IRAF CL scripts. The following data is passed into model fitting program: (1) image of object; (2) mask image; (3) PSF image; (4) initial center coordinates of object, x_{in}, y_{in}; (5) radius, r_{fit}, defining a fitting area; and (6) photometric background, μ_{sky}, which is kept constant during

iterative fitting process, and its uncertainty rms, σ_{sky}. FitClust has an option to fit photometric background and model simultaneously, however, it is more reliable to determine μ_{sky} interactively in case of crowded environment. For example of the influence of sky background subtraction on the derived cluster parameters see Hill & Zaritsky (2006).

Object sub-images are cut from mosaic and used to derive structural parameters. The representative photometric background, μ_{sky}, which is set constant during model fit, is estimated from the histogram of pixels inside individually selected circular annulus, centered on the object's position.

The model fitting radius, r_{fit}, is chosen by referring to object's flux curve of growth, seeking to enclose extended wings of the surface brightness distribution profile, yet to avoid very bright contaminants in crowded environment. For objects possessing saturated stars outside r_{fit} or image defects inside circular fitting region bad pixel masks are generated.

2.2.2 Analytical Models

Star clusters are modeled with circular/elliptical King (King 1962) and EFF (Elson et al. 1987) profiles. The King model (see Fig. 2.9 (b)) is defined by the central surface brightness, μ_0, the core radius, r_c, and the tidal radius, r_t:

$$\mu(r) = \mu_0 \left[\left(1 + \frac{r^2}{r_c^2}\right)^{-1/2} - \left(1 + \frac{r_t^2}{r_c^2}\right)^{-1/2} \right]^2 . \tag{2.1}$$

The concentration parameter is $c = \log(r_t/r_c)$. The EFF model is defined by μ_0, the effective radius, r_e, and the power-law index, n:

$$\mu(r) = \mu_0 \left(1 + \frac{r^2}{r_e^2}\right)^{-n} . \tag{2.2}$$

In case of the elliptical models, radius, r, is defined along the major axis of ellipse.

Such a model is placed into a 2D pixel array[17] and convolved[18] with PSF to account for the observational effects on the light distribution of cluster. Superimposed contaminating stars are identified automatically and modeled

[17]FITSIO: `http://heasarc.nasa.gov/fitsio/`.

[18]FFT: `http://www.kurims.kyoto-u.ac.jp/~ooura/fft.html`.

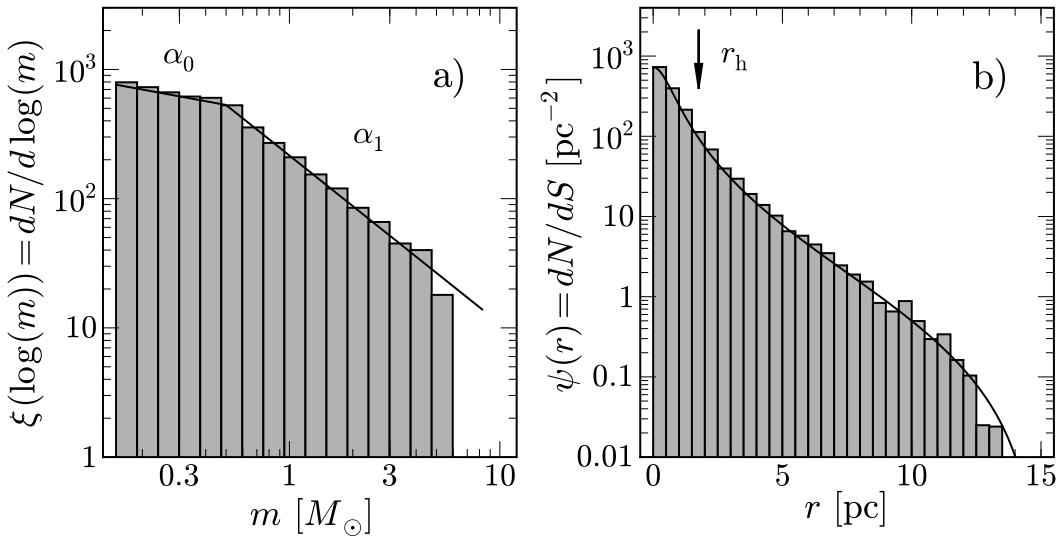

Fig. 2.9. Properties of a model star cluster with $t = 100\,\mathrm{Myr}$ and luminous mass $M_{\rm lum} = 3000\,\mathrm{M}_\odot$, consisting of $N_{\rm lum} = 5300$ stars. The stellar mass distribution, $\xi(\log(m)) = dN/d\log(m)$, is displayed vs. mass, m, in panel (a), overplotted with slope $\alpha_0 = -1.3$ and $\alpha_1 = -2.3$ lines of IMF (see Eq. 2.4). The lower and upper mass limits are defined by the isochrone. The surface number density of stars, $\psi(r) = dN/dS$, is plotted vs. radial distance, r, in panel (b), obeying King (1962) model profile of $r_{\rm c} = 0.75\,\mathrm{pc}$ and $r_{\rm t} = 15\,\mathrm{pc}$ (see Eq. 2.1); half-light radius $r_h \sim 1.7\,\mathrm{pc}$ is indicated by an arrow.

with plain PSF.

2.2.3 Model Parameter Space

Two sets of free parameters are used to define: (1) a model of star cluster $\{x, y, \epsilon, \theta, p_1, p_2, \mu_0\}$; and (2) superimposed s contaminants $\{x_1^*, y_1^*, m_1^*, \ldots, x_s^*, y_s^*, m_s^*\}$; $7 + 3 \times s$ free parameters in total. They are:

- x, y – center coordinates of cluster;
- ϵ, θ – ratio of the major and minor axes (b/a) of ellipse and position angle of the major axis counterclockwise from the x axis of image;
- p_1, p_2 – the core radius, r_c, and the concentration parameter, c, of King model, or the effective radius, r_e, and the power-law index, n, of EFF model, respectively;
- μ_0 – central surface brightness;
- x^*, y^*, m^* – center coordinates and magnitude of contaminant.

When all other parameters are fixed and μ_{sky} is subtracted from the image, μ_0 and $\{m_1^*, \ldots, m_s^*\}$ are determined simultaneously as the linear

least squares solution[19], yielding the pixel value rms, σ_{fit}, which is computed for pixels inside r_{fit}, but not marked in the bad pixel mask. Weights of all pixels inside r_{fit} for σ_{fit} computation were fixed to be equal.

Since μ_0 and $\{m_1^*, \ldots, m_s^*\}$ are indirect free parameters, search for the best fit (i.e., global) solution in lesser $6 + 2 \times s$ free parameter space is a minimization of the goodness criterion, σ_{fit}, problem, complicated by noise, initially unknown positions of s contaminants, and time consuming convolution procedure.

Therefore, we adopt an iterative approach:

1. Start with no contaminants ($s = 0$), fit only the cluster model and identify s contaminants in the remnant[20] image.
2. Fit model and s contaminants simultaneously while keeping contaminant positions fixed, identify s_{new} contaminants anew.
3. Repeat previous step two times, noting that number of contaminants might change, $s_{new} \neq s$, and their positions shift in respect to the preceding iteration.
4. Exit with the best fit parameters $\{x, y, \epsilon, \theta, p_1, p_2, \mu_0\}$.

When s contaminants are identified and their positions $\{x_1^*, y_1^*, \ldots, x_s^*, y_s^*\}$ are fixed, the parameters of star cluster $\{x, y, \epsilon, \theta, p_1, p_2\}$ are determined by employing the PIKAIA genetic algorithm (see Charbonneau 1995 for the detailed description). PIKAIA searches this six parameter space by computing $\sim 10^4$ models and converges close to the point of global minimum. For the fine-tuning of the solution we use Levenberg-Marquardt nonlinear least square algorithm.

2.2.4 Identification of Contaminants

The IRAF's `allstar` is used to automatically identify star-like objects (i.e., contaminants) in the remnant image. The criteria for contaminants are: (1) distance from cluster's center $r < r_{fit} + 2 \times \mathrm{FWHM_{PSF}}$; and (2) magnitude difference $m^* - m_{r_{fit}} < 3\,\mathrm{mag}$, where m^* is magnitude of contaminant, and $m_{r_{fit}}$ – magnitude of cluster, measured through a circular aperture of radius r_{fit}.

[19] LAPACK: `http://www.netlib.org/lapack/`.

[20] Image minus cluster model; contaminants remaining.

2.2.5 Determination of Half-Light Radii

The true half-light radii, r_h, of star clusters are derived from King and EFF model images, before they are convolved with PSF. IRAF's `phot` is employed to obtain the curve of growth of model, integrating through circular apertures up to the truncation radius, r_{max}, where the surface brightness, μ, of model reaches 1% of its central value, μ_0.

For most, except for the brightest sample clusters, signal μ is below rms of photometric background, μ_{sky}. The use of r_{max} ensures the consistency between $r_h^{\rm E}$ of EFF model and $r_h^{\rm K}$ of King model, and solves inconvenience of EFF model, that for $n \to 1$, $r_h^{\rm E}$ becomes unreasonably large.

We have applied FitClust program to derive structural parameters of sample of star clusters in the crowded field of the M31 galaxy disk southwest field by fitting circular King/EFF models. We have performed various tests of artificial star clusters to evaluate the performance of FitClust and assess the accuracy of structure model fitting.

2.3 Photometric Quantification

We employ the PEGASE (V.2.0) program package (Fioc & Rocca-Volmerange 1997), applying its default options and stellar initial mass function (IMF; Kroupa 2002), to compute SSP models ($U-V$, $B-V$, $V-R$ and $V-I$ color indices) of various star cluster ages and metallicities. The reddened color indices are calculated as a function of color excess, $E(B-V)$, assuming the standard extinction law (Cardelli et al. 1989).

The stellar IMF defines a number of stars, dN, within a stellar mass range, dm. The universal IMF (Kroupa 2001), defined as the multi-power law, has a general form of

$$\xi(m) = dN/dm = A_{\rm IMF} \cdot b_i \cdot m^{\alpha_i} \,, \tag{2.3}$$

where α_i is the IMF slope for the stellar mass interval $[m_{i-1}, m_i]$, $A_{\rm IMF}$ and b_i are the normalization and function continuation constants, respectively.

The IMF slope (Eq. 2.3, Kroupa 2001) transforms into a simple equation:

$$\begin{cases} \alpha_0 = -1.3, & m/\mathrm{M}_\odot < 0.50\,; \\ \alpha_1 = -2.3, & m/\mathrm{M}_\odot \geq 0.50\,. \end{cases} \tag{2.4}$$

An example of the resulting stellar mass distribution, $\xi(\log(m)) = dN/d\log(m)$, displayed vs. mass, m, of $t = 100\,\mathrm{Myr}$ model star cluster of luminous mass $M_{\mathrm{lum}} = 3000\,\mathrm{M}_\odot$, consisting of $N_{\mathrm{lum}} = 5300$ stars, is shown in Fig. 2.9 (a), overplotted with the IMF slope lines (see Eq. 2.4).

The three-parameter SSP model grid is constructed at the following nodes: (1) 75 age, t, values from 2 Myr to 20 Gyr, with a constant step of $\log(t/\mathrm{Myr}) \approx 0.05$, starting from $t = 6\,\mathrm{Myr}$ (for younger ages grid nodes are located at 2, 3, 4, 5 Myr); (2) 31 metallicity, [M/H], values from -2.3 to $+0.7$, with a step of 0.1 dex; (3) 199 color excess, $E(B-V)$, values from 0.02 to 2.0, with a step of 0.01; $\sim 5 \times 10^5$ models in total.

A star cluster parameter quantification code, using a technique similar to the one developed for star quantification (Vansevičius & Bridžius 1994), was implemented in the environment of data analysis and graphing software package OriginLab[21]. The parameter quantification is based on a comparison of the observed color indices of star cluster with those of the SSP models from the model grid. For this purpose we use the quantification criterion, δ, which is calculated as:

$$\delta = \sqrt{\frac{\sum_{i=1}^{m} w_i (CI_i^{\mathrm{obs}} - CI_i^{\mathrm{mod}})^2}{\sum_{i=1}^{m} w_i}}\,, \tag{2.5}$$

where CI_i^{obs} stands for the observed color indices, CI_i^{mod} – the corresponding color indices of SSP model, m – the number of color indices used, w_i – the weights of the observed color indices, which depend on the photometric error, σ_{phot}, and were assigned to 1 or $10^{-4}/\sigma_{phot}^2$ for $\sigma_{phot} \leq 0.01$ and $\sigma_{phot} > 0.01$, respectively.

Object color indices were compared with those of SSP models from the model grid, δ was calculated at each grid node, and its distribution maps in

[21] OriginLab: `http://www.originlab.com/`.

the parameter space were analyzed. In some cases one deviating color index in poor agreement with models, probably due to background contaminants or stochastic bright stars, was excluded from δ calculation by assigning $w_i = 0$.

The quantified best fit parameters t, [M/H], and $E(B-V)$, and their standard deviations σ_t, $\sigma_{[\mathrm{M/H}]}$, and $\sigma_{E(B-V)}$ were calculated as the SSP model parameter weighted averages, using only models which have δ lower than the applied threshold, $\delta \leq \delta_{max}$. The weights for parameter averaging were assigned to 1 or $10^{-4}/\delta^2$ for the models with $\delta \leq 0.01$ and $\delta > 0.01$, respectively. The δ_{max} value was adopted considering the σ_{phot} values of object's color indices, and was roughly equal to the average photometric error. The standard deviation of each quantified parameter was estimated by measuring a size of the "island" formed in the parameter space below the δ_{max} threshold.

2.3.1 Parameter Degeneracy Constrains

The well known age-metallicity-extinction degeneracy makes the procedure described above a non trivial task, because of a few possible isolated $\delta \leq \delta_{\max}$ "islands" of minima (global and local) in the 3D parameter space. Therefore, formal averaging could yield parameters between the "islands".

To reduce this problem following steps were adopted:

1. We have initially assorted cluster candidates into 9 age/metallicity groups.
2. We have referred to their multi-band images checking the validity of the initial group assignment.
3. We have defined the limits of age/metallicity for each group, rejecting unreasonable secondary "islands".
4. We have checked the consistency of $E(B-V)$ with extinction assessed from *Spitzer* (24 μm) warm dust emission distribution and surrounding dust lanes, observed in U and B passband images.
5. For very uncertain solutions of metallicity, we have adopted lower and upper boundaries of [M/H] as a function of age, which come from the chemical evolution model prediction for the M31 disk (Renda et al. 2005).

The mass of cluster in the solar mass unit, $m/\mathrm{M}_{\odot}$, was calculated equating the mass-to-luminosity ratio of the best fit SSP model of age, t, and metallicity, [M/H], to the de-reddened cluster's absolute aperture V passband luminosity, M_V. The mass of the cluster derived by the SSP model fitting and used in population analysis is usually the initial mass at the cluster's birth.

In the following we study performance of *UBVRI* photometric system to quantify star cluster parameters from integrated photometry and compare the results to that of *UBVRIJHK* system.

2.3.2 Cluster Parameters From *UBVRI*

We investigate the possibility to quantify star cluster parameters (age t, metallicity [M/H] and color excess $E(B-V)$) comparing their integrated color indices $U-V$, $B-V$, $V-R$ and $R-I$ with the simple stellar population (SSP) models. The purpose of this study is to evaluate the reliability of the derived parameters assuming different levels of photometric accuracy, and to identify parameter ranges susceptible to degeneracies.

For similar purposes various χ^2 minimization techniques have been used (e.g., Bik et al. 2003; Maiz Apellaniz 2004; de Grijs et al. 2005). The systematic uncertainties of quantified parameters, associated with the selection of photometric passbands, have been studied in detail by Anders et al. (2004). The importance of interstellar extinction and star cluster metallicity has been widely discussed based on various SSP models and parameter quantification techniques by de Grijs et al. (2005). These studies concentrated on a statistical analysis of the derived parameters for large samples of artificial or real star clusters.

The sample of 54 SSP models was selected from the model grid for further analysis as the test star clusters ($t = 20, 50, 100, 200, 500\,\mathrm{Myr}$ and 1, 2, 5, 10 Gyr; [M/H] $= 0.0, -0.7, -1.7$ dex; $E(B-V) = 0.1, 1.0$). The first color excess value was chosen to represent a typical foreground MW extinction, inherent to extragalactic objects, and the second – substantially obscured star clusters in the spiral galaxy disks.

In the present study CI_i^{obs} represents color indices ($n = 4$) of the test star clusters (see Eq. 2.5), and weights assigned to color indices are equal

($w_i = 1$). The quantification criterion δ mimics the effect of photometric accuracy. In general, it represents average observation errors of color indices. Therefore, we use δ to study star cluster parameter degeneracies and, by setting different $\delta_{\max}$ thresholds, determine parameters and estimate their accuracy for a corresponding photometric error budget.

The test star cluster colors are compared with the colors of all SSP models from the model grid and δ is calculated at each grid node. Then the test star cluster parameters (t, [M/H] and $E(B-V)$) are calculated as the SSP model parameter weighted averages, using only those models, which have δ lower than the applied threshold ($\delta \leq \delta_{\max}$). We use five $\delta_{\max}$ values (0.01–0.05 mag, with a step of 0.01 mag) and provide the quantification results as well as their standard deviations in Figs. 2.10 & 2.11 for color excess values $E(B-V) = 0.1$ and 1.0, respectively. The weights for parameter averaging and calculation of standard deviations were assigned to 1 and to $(10^{-4}/\delta^2)$ for the SSP models with $\delta \leq 0.01$ and $\delta > 0.01$, respectively.

The well known age-metallicity-extinction degeneracy makes the procedure described above not a trivial task, because of a few possible isolated $\delta \leq \delta_{\max}$ "islands" in the parameter space. To overcome this problem we have chosen to select interactively a proper "island" for calculations of the parameters and their standard deviations. In reality such an improvement of the blind quantification procedure could be based on multi-band star cluster environment images or other a priori information, e.g., metallicity estimated by spectroscopic methods. Therefore, to calculate the weighted averages of parameters and their standard deviations we used only the SSP models, which reside in a single selected "island", satisfying the $\delta \leq \delta_{\max}$ criterion. This procedure excludes the models located in secondary δ minima, which arise due to parameter degeneracies. For purposes of the present study, boundaries of a continuous $\delta \leq \delta_{\max}$ "island" were determined by starting the search from the global δ minimum, i.e., from the position of the test star cluster under consideration in the SSP model grid. The parameter quantification maps for some characteristic test star clusters are shown in Figs. 2.12–2.17.

The summary of the parameter quantification results of the 54 test star clusters is provided in Figs. 2.10 & 2.11. In each panel the differences of pa-

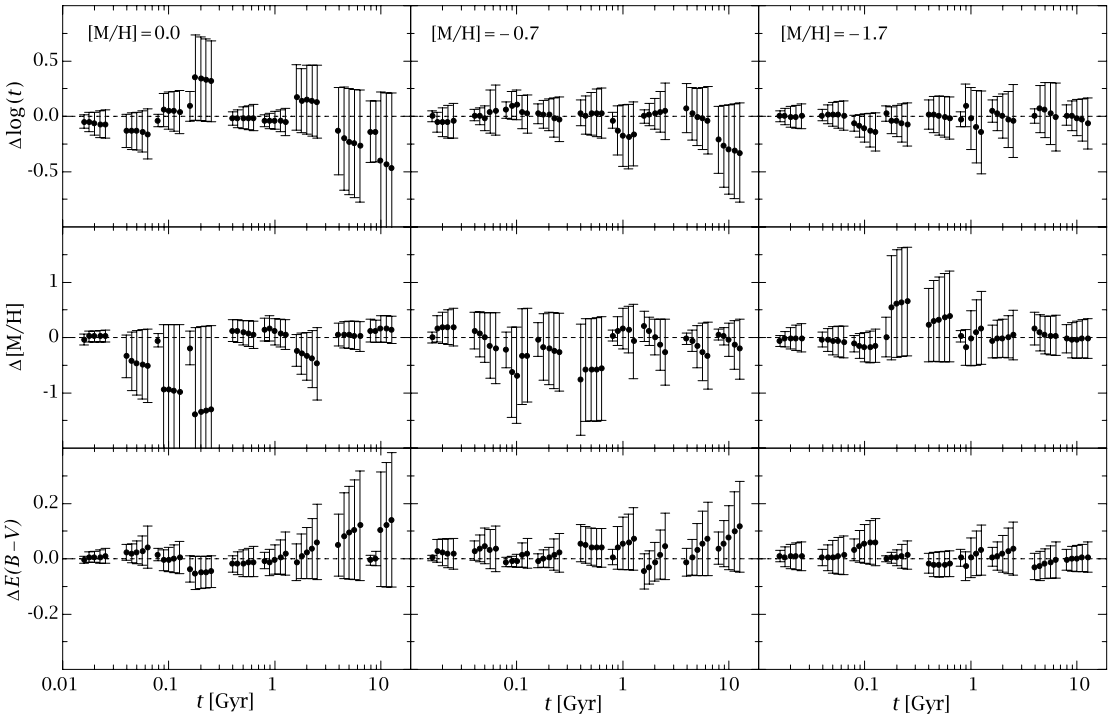

Fig. 2.10. Summarized test star cluster parameter quantification results for the case of color excess $E(B-V) = 0.1$. Different metallicity ([M/H] $= 0.0, -0.7, -1.7$ dex) cases are shown in the left, middle and right panels, respectively. Differences of the parameters (determined minus true) are shown in groups of five filled circles, centered at the true test star cluster ages; within a group from left to right the circles correspond to the quantification results derived at $\delta_{\rm max} = 0.01$–0.05 mag, with a step of 0.01 mag. Error bars indicate standard deviations of the derived parameters.

rameters (determined minus true) are shown in groups of five filled circles (centered at their true age on t-axis), corresponding to the quantification criterion values of $\delta \leq 0.01$–0.05 mag, with a step of 0.01 mag (plotted from left to right). Error bars indicate standard deviations of the determined parameters and characterize sizes of the $\delta \leq \delta_{\rm max}$ "islands" in the parameter space. Note that higher metallicity (Fig. 2.10) and larger extinction (Fig. 2.11) make the quantification procedure less accurate.

The parameter quantification maps of the representative star clusters of age $t = 50$ Myr, 500 Myr and 5 Gyr are displayed in Figs. 2.12–2.17; different shades of gray represent $\delta \leq 0.01$, 0.03 and 0.05 mag (from the darkest to the lightest). The analysis of parameter quantification map patterns reveals that the test star clusters can be subdivided into three broad age groups according to the shape of the age-metallicity degeneracy: (1) younger than

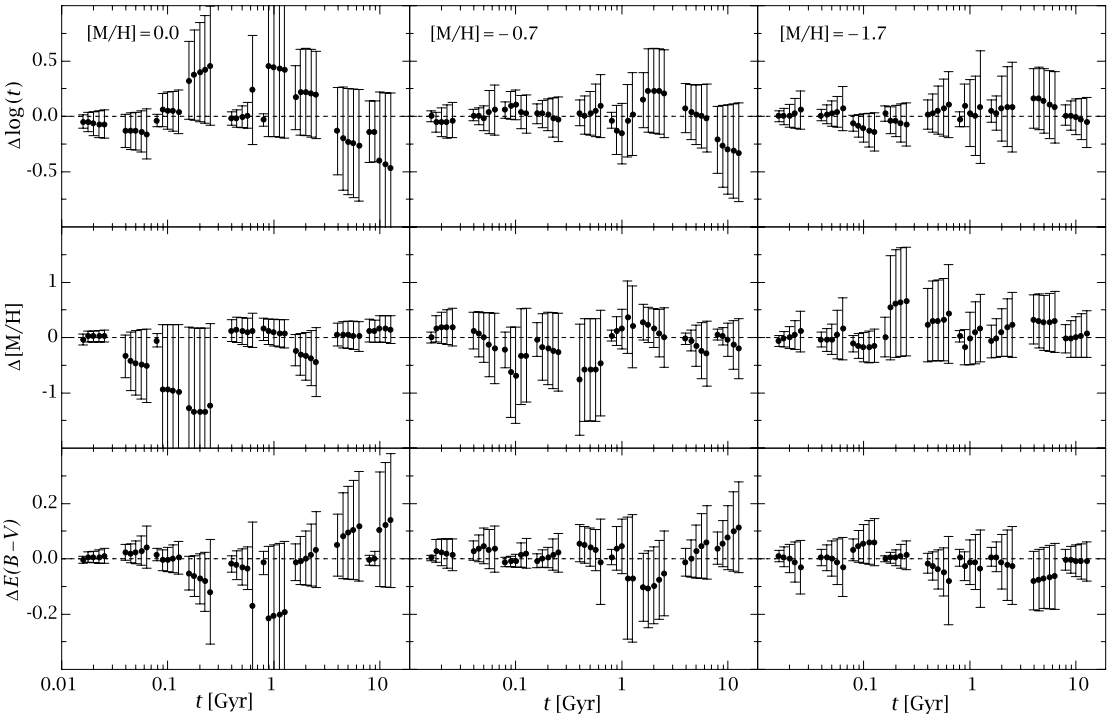

Fig. 2.11. The same as in Fig. 2.10, but for the case of color excess $E(B-V) = 1.0$.

$\sim$100 Myr (Figs. 2.12 & 2.13); (2) older than $\sim$100 Myr and younger than $\sim$1 Gyr (Figs. 2.14 & 2.15); (3) older than $\sim$1 Gyr (Figs. 2.16 & 2.17). Note, however, that the age-extinction maps are much more regular, than the age-metallicity maps, and the shape of δ "islands" gradually changes from the youngest to the oldest cluster ages. In general, the parameter degeneracies seen in Figs. 2.12–2.17 are mainly preconditioned by the properties of the *UBVRI* photometric system itself, and should not depend strongly on the PEGASE SSP models used for the construction of the model grid.

The ultraviolet (UV) and infrared (*JHK*) passbands are known to be helpful for breaking the age-metallicity degeneracy, see, e.g., de Grijs et al. (2003). However, the accuracy of the UV and *JHK* photometry is usually lower than the accuracy, which can be achieved in *UBVRI* passbands. Therefore, the information on metallicity – at least a rough estimate from spectroscopy – is of high importance for improving the accuracy of the quantification procedure. Even a realistic assumption, used in various star cluster studies (e.g., a study of the M51 galaxy by Bik et al. 2003), helps to constrain cluster ages.

We conclude that the *UBVRI* photometric system enables us to estimate

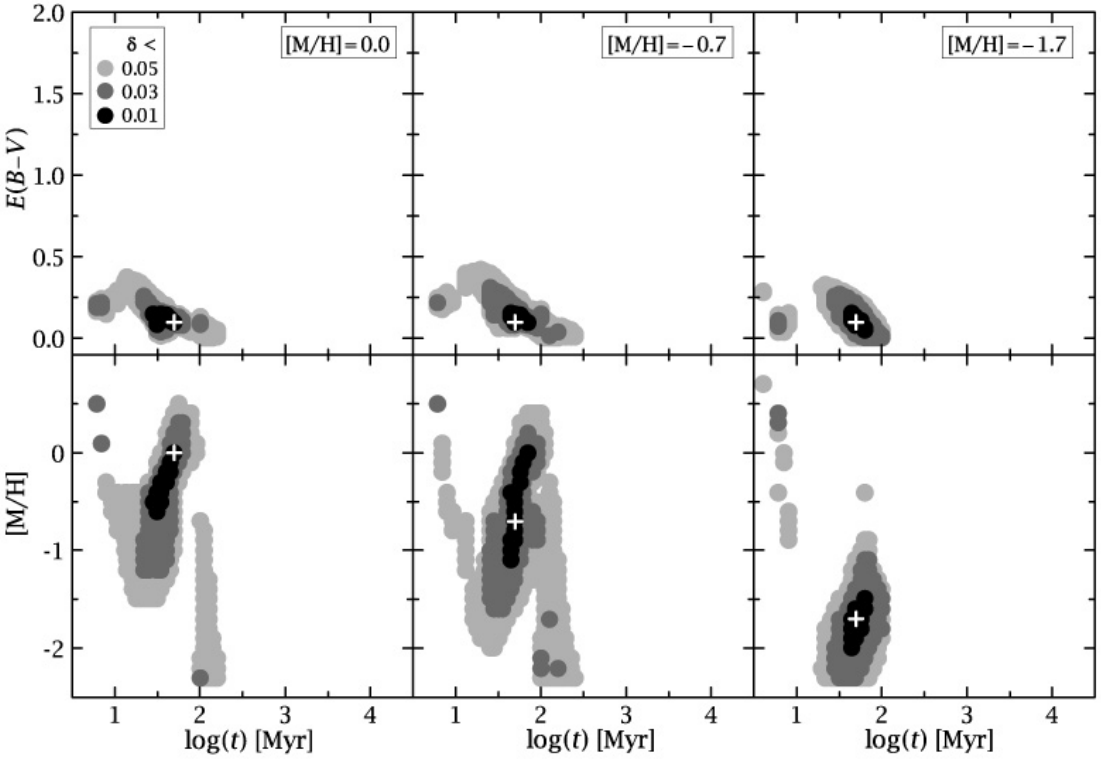

Fig. 2.12. Parameter quantification maps of the test star clusters of age $t = 50\,\mathrm{Myr}$, color excess $E(B-V) = 0.1$ and metallicity $[\mathrm{M/H}] = 0.0, -0.7, -1.7\,\mathrm{dex}$ (left, middle and right panels). True parameter values are marked with a white "plus" symbol. Gray levels correspond to a quantification criterion of $\delta \leq 0.01, 0.03, 0.05\,\mathrm{mag}$.

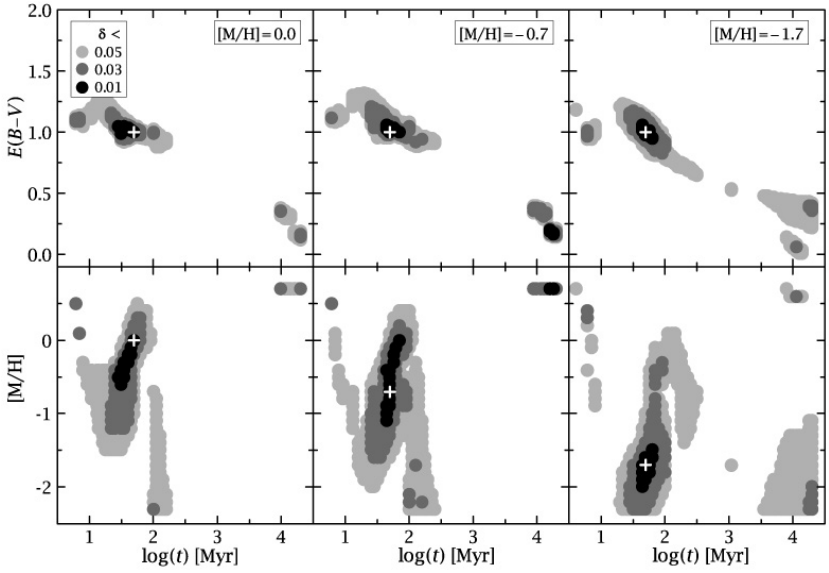

Fig. 2.13. The same as in Fig. 2.12, but for the case of color excess $E(B-V) = 1.0$.

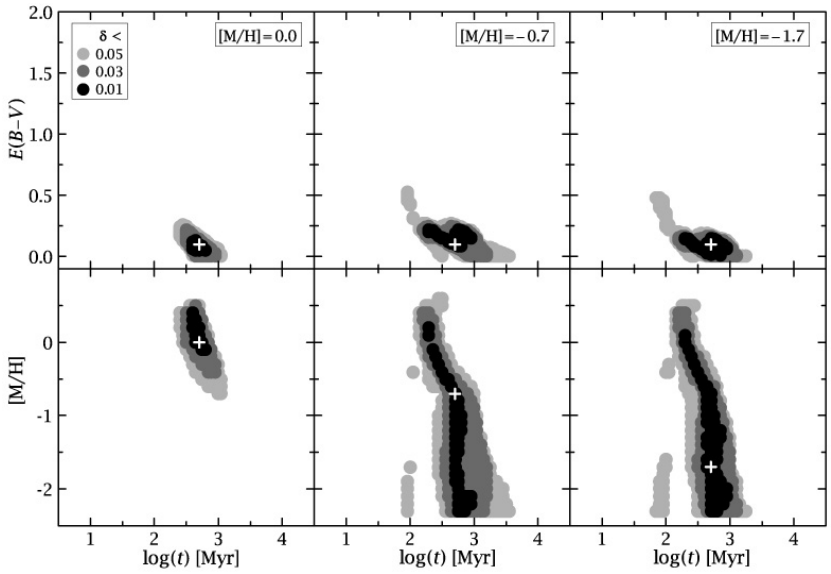

Fig. 2.14. The same as in Fig. 2.12, but for the case of age $t = 500\,\mathrm{Myr}$.

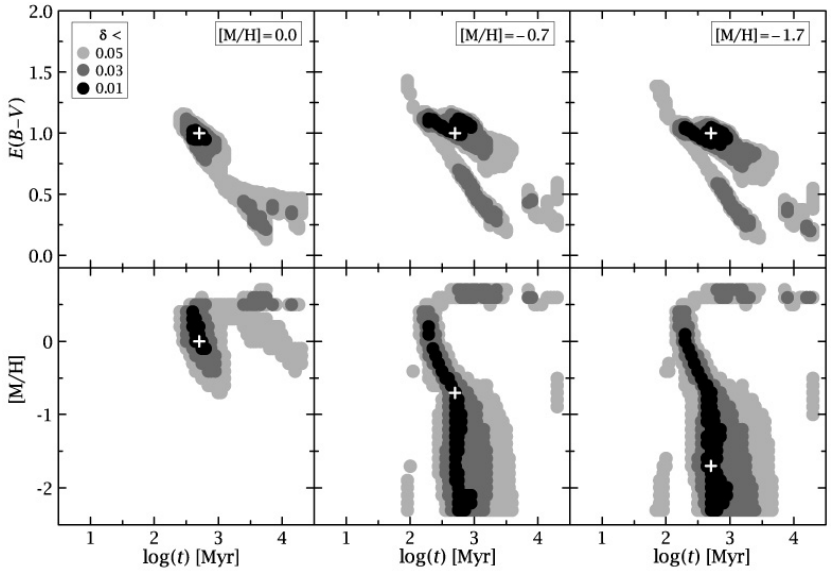

Fig. 2.15. The same as in Fig. 2.13, but for the case of age $t = 500\,\mathrm{Myr}$.

star cluster parameters over a wide range, if the overall accuracy of color indices is better than $\sim$0.03 mag.

2.3.3 Cluster Parameters From *UBVRIJHK*

Broadband photometric data of extragalactic star clusters are applicable to derive their evolutionary parameters via comparison with SSP models. However, this procedure is restricted by the fact that in some parameter domains strong age-metallicity-extinction degeneracies (see, e.g., Worthey 1994) remain unsolved. For a study of broadband color indices, most sensitive to various star and cluster parameters, see, e.g., Jordi et al. (2006) and Li et al. (2007).

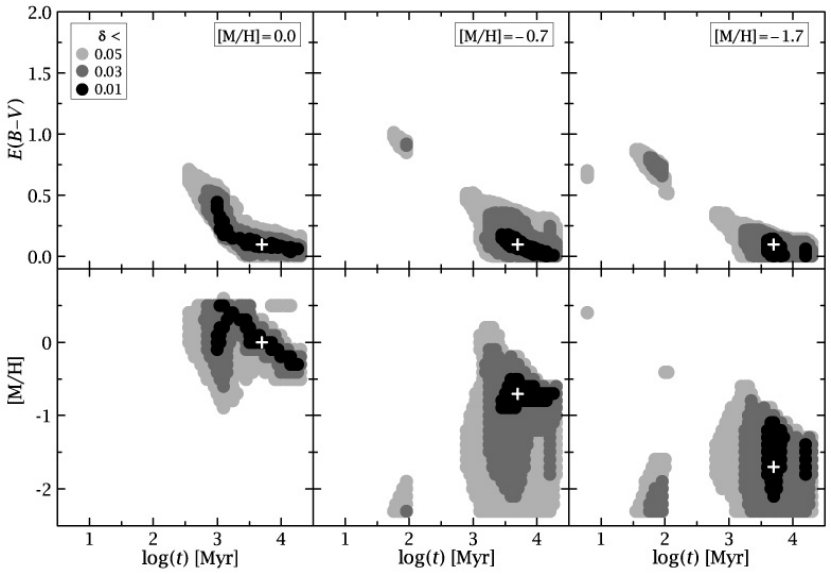

Fig. 2.16. The same as in Fig. 2.12, but for the case of age $t = 5\,\mathrm{Gyr}$.

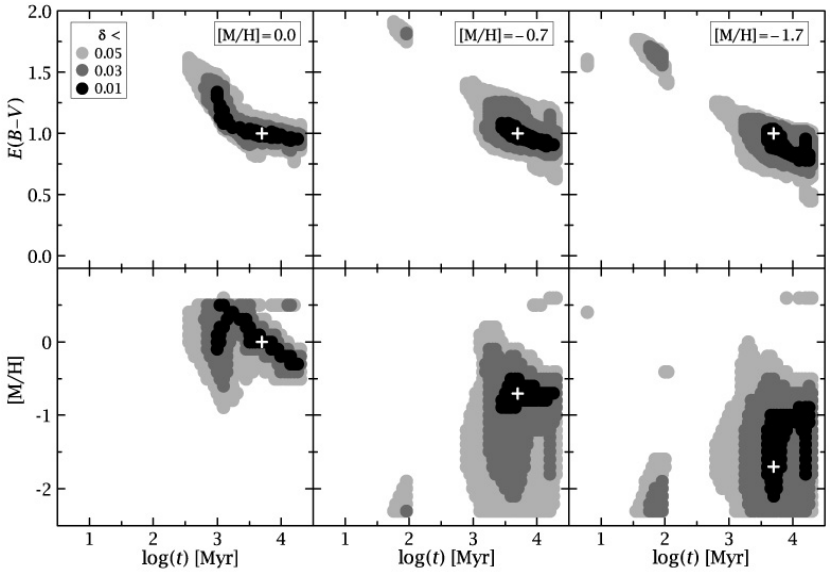

Fig. 2.17. The same as in Fig. 2.13, but for the case of age $t = 5\,\mathrm{Gyr}$.

It is known (Anders et al. 2004; Kaviraj et al. 2007) that infrared and ultraviolet passbands are helpful for breaking the age-metallicity-extinction degeneracies. In this respect infrared observations have the priority: in some atmospheric windows they are accessible for ground-based telescopes, while ultraviolet photometry shorter than 300 nm is possible only from space.

However, in comparison to photometry in the optical range, ground-based infrared photometry usually has larger errors due to variable humidity, and this requires careful calibration (e.g., Kodaira et al. 1999; Kidger et al. 2006). The reliability of secondary standards used for photometric calibration of wide-field images, should be verified by several independent

sources, if they are available.

Here we investigate a possibility of determining star cluster parameters and discuss how the addition of the *JHK* passbands affects the accuracy of cluster parameter. We analyze degeneracies at various accuracy levels of photometry for the same values of cluster parameters. We have assigned the weights (see Eq. 2.5) of $w_i = 1$ for $U-V$, $B-V$, $V-R$ and $V-I$ color indices, and $w_i = 1/9$ for $V-J$, $V-H$ and $V-K$ of the "observed" star clusters. Such weighting scheme assumes that the accuracy of the infrared *JHK* observations is $\sim$3 times lower than that of the optical *UBVRI* – a typical condition in photometry of extragalactic star clusters.

Anders et al. (2004) in a similar study have extensively analyzed the possibilities of their AnalySED method, which has a different approach to the degeneracy problem, comparing to the method presented here. First, AnalySED is based on the comparison of observed magnitudes with the model magnitudes, while for the same aim we are using color indices. This allows us to avoid fitting an additional free parameter – the cluster mass. Second, Anders et al. (2004) define the "observed" magnitudes of model clusters by assigning random errors to them. However, we did not apply "observation errors" to color indices, since it is reasonable to assume that the quantification quality criterion, δ, reflects the effect of photometric accuracy sufficiently well. In general, δ represents the lowest possible average photometric error of all color indices, which in the case of real clusters can be larger, mostly due to the influence of crowding by contaminating field stars. Therefore, the parameter degeneracy analysis presented in this study is based on minimum assumptions.

We have used several $\delta_{\max}$ values as the upper threshold levels of photometric errors. The cluster parameters were determined independently at each accuracy level by averaging the corresponding parameter values of SSP models at the grid nodes, which have $\delta \leq \delta_{\max}$. The weights for the calculation of the parameter averages and the standard deviations were assigned 1 and $10^{-4}/\delta^2$ for the nodes with $\delta \leq 0.01$ and >0.01 mag, respectively.

Furthermore, for the parameter averaging we used only the nodes, which reside in a single continuous "island" around the true cluster position in the 3-D parameter space of the SSP model grid. Boundaries of "islands" at

each $\delta_{\max}$ level were determined automatically by the clustering procedure, which finds discontinuities in the parameter space, starting from the true position of the cluster. Such a procedure excludes nodes, which are located in the secondary δ minima, arising due to the age-metallicity-extinction degeneracies in the 3-D parameter space.

The results of parameter determinations of clusters are provided in Figs. 2.18 & 2.19 for color excess values $E(B-V) = 0.1$ and 1.0, respectively. In each panel the differences of parameters (determined minus true) are shown in groups of five filled circles, the middle circle is positioned at the true age of the cluster, i.e., the circles indicate parameters determined at $\delta_{\max}$ threshold values from 0.01 to 0.05 mag, with a step of 0.01 mag, plotted from left to right. Open and black circles correspond to the *UBVRI* and *UBVRIJHK* passband set cases, respectively. Error-bars indicate standard deviations of the determined parameters and characterize the integrated "size" of the $\delta \leq \delta_{\max}$ "island" in the corresponding parameter space.

It is clearly visible in both Figs. 2.18 & 2.19 that additional usage of *JHK* passbands significantly improves the precision of cluster parameter determination with respect to the *UBVRI* passbands alone. Especially good results are in the case of the small color excess, $E(B-V) = 0.1$, value. Note that strong age-metallicity degeneracies at ages $t = 0.1$, 0.2 and 10 Gyr, which are present in the *UBVRI* case, completely disappear in the *UBVRIJHK* case. A similar, but a slightly weaker effect is also visible for models of ages $t = 2$ and 5 Gyr. However, if objects are highly reddened, $E(B-V) = 1.0$, there are still notable parameter degeneracies for some cases. The strongest age-extinction degeneracy is for clusters with: $t = 1$ Gyr and [M/H] = 0.0 dex; $t = 2$ Gyr and [M/H] = -0.7 dex; $t = 5$ Gyr and [M/H] = -1.7 dex. Actually, the quantification results of the last case are much more accurate, when SSP models older than 15 Gyr are not included in the calculation of the average.

The impact of adding the *JHK* passbands to the *UBVRI* system on the accuracy of the quantification of cluster parameters is illustrated in Figs. 2.20–2.27 for the clusters of ages $t = 0.2, 1, 2, 5, 10$ Gyr for solar metallicity, and $t = 0.5$ Gyr for [M/H] = -1.7 dex. The figures display cluster parameter quantification maps at the threshold levels of $\delta_{\max} = 0.01$, 0.03

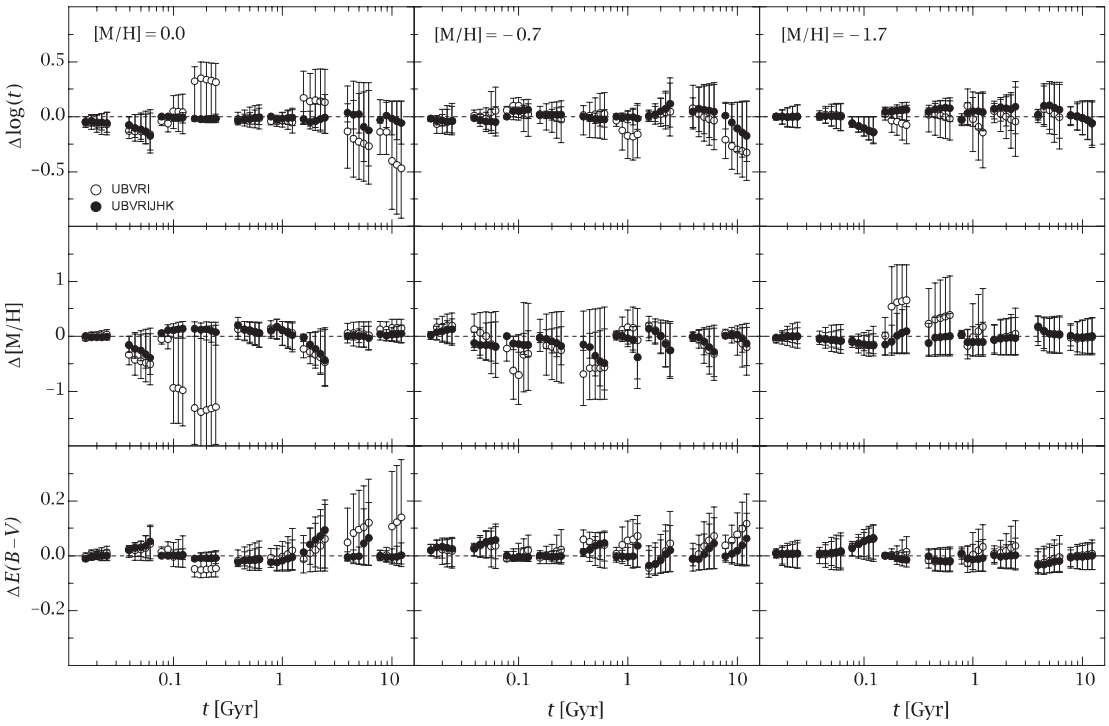

Fig. 2.18. Star cluster parameter determination results for star clusters with the following parameters: age, $t = 0.02, 0.05, 0.1, 0.2, 0.5, 1, 2, 5, 10$ Gyr; metallicity, [M/H] $= 0.0, -0.7, -1.7$ dex (left, middle and right panels); color excess, $E(B-V) = 0.1$. Differences of the parameters (determined minus true) are shown in groups of five filled circles, the middle of which is positioned at the true age of a star cluster. Within a group, from left to right, the circles correspond to the quantification results derived for $\delta_{\max}$ from 0.01 to 0.05 mag, with a step of 0.01 mag. Open and black circles correspond to *UBVRI* and *UBVRIJHK* passband set cases, respectively. Error-bars indicate the standard deviation of the derived parameters.

and 0.05 mag.

In Figs. 2.20 & 2.22 for the *UBVRI* set, the left and the central panels look very similar, although the left panel displays quantification map of a cluster with $t = 200$ Myr and [M/H] $= 0.0$ dex, while the central panel – for a cluster with $t = 500$ Myr and [M/H] $= -1.7$ dex. This means that due to the age-metallicity degeneracy for both clusters we obtain similar and wrong parameters. However, the situation changes when the *JHK* magnitudes are added. Figs. 2.21 & 2.23 display quantification maps of the same clusters, but for the *UBVRIJHK* passband set. Note that degeneracies disappear, even at $\delta_{\max} = 0.05$ mag level.

An interesting example is the cluster with the parameters $t = 2$ Gyr

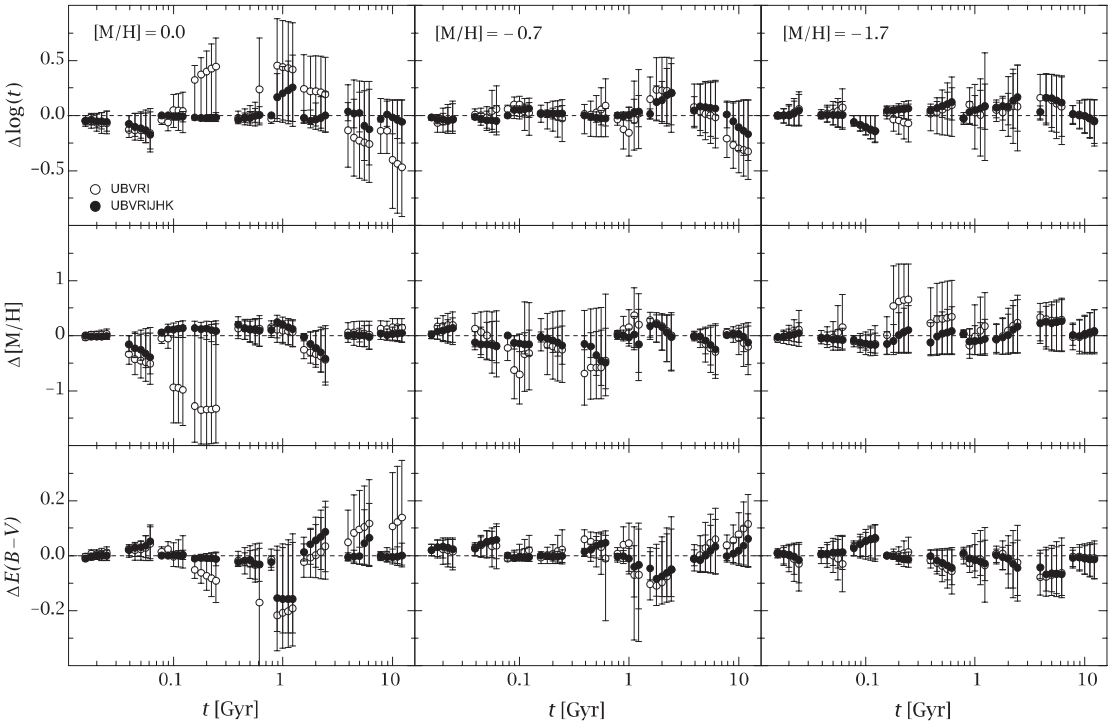

Fig. 2.19. The same as in Fig. 2.18, but for the case of color excess $E(B-V) = 1.0$.

and [M/H] = 0.0 dex. Figs. 2.18 & 2.19 show that the addition of the *JHK* magnitudes improves the age determination, but $E(B-V)$ determination becomes of lower accuracy, comparing to the *UBVRI* set alone. Rightmost panels in Figs. 2.20–2.23 clarify this situation. In the *UBVRI* case, strong age-metallicity degeneracy takes place: note the additional "tail" of suitable SSP models in the $E(B-V)$ vs. t plane towards older ages and lower $E(B-V)$ values. This helps to compensate the influence of SSP models at higher $E(B-V)$ values, and the quantification produces a "correct" reddening. In the case of *UBVRIJHK*, no such "tail" is seen, therefore the determined $E(B-V)$ value is shifted from its true position.

Figs. 2.24–2.27 display three similar cases of parameter degeneracies for clusters of solar metallicity and ages $t = 1$, 5 and 10 Gyr. Only the 10 Gyr age sample is sensitive enough to the addition of the *JHK* passbands, when parameter degeneracies become broken even at $\delta_{\max} = 0.05$ mag level. On the contrary, for the ages of 1 Gyr (except for the case of $E(B-V) = 0.1$; see Figs. 2.24 & 2.25) and 5 Gyr, parameter degeneracies exist even for $\delta_{\max} =$ 0.01 and 0.03 mag, respectively. This implies that the overall accuracy of

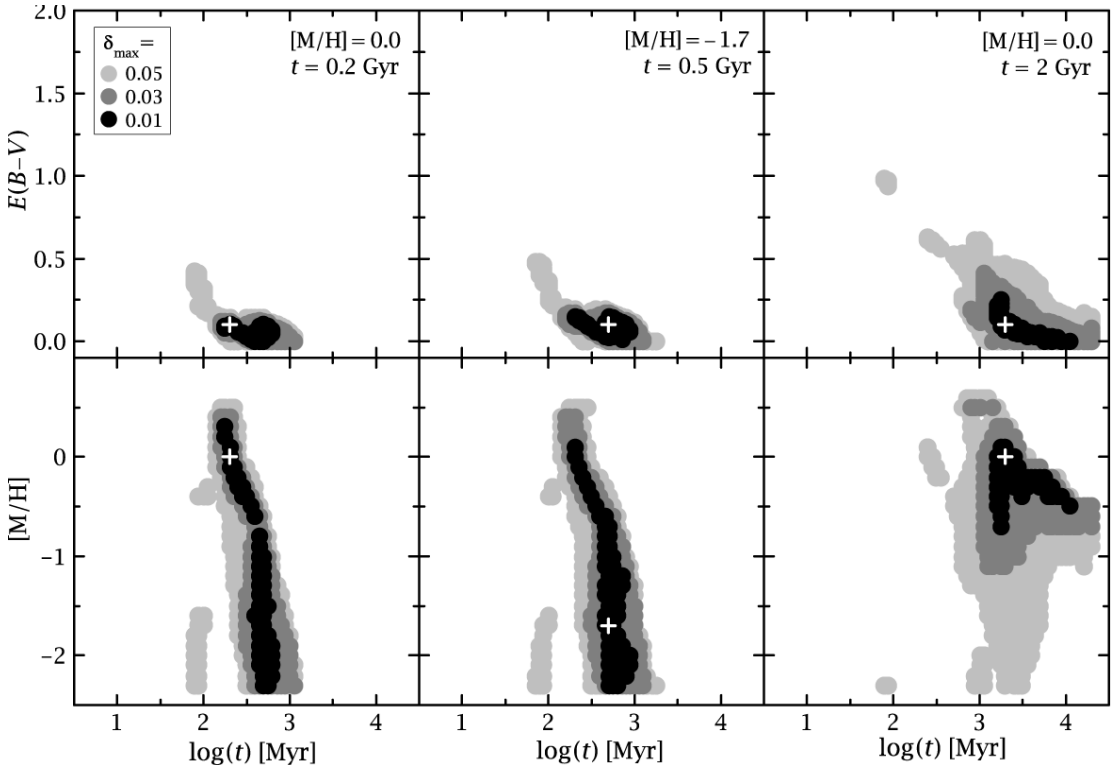

Fig. 2.20. The distribution of the quantification quality criterion, δ, in projection onto the $E(B-V)$ and [M/H] vs. $\log(t/\mathrm{Myr})$ planes for the clusters with the parameters: $E(B-V) = 0.1$, [M/H] $= 0.0$ dex, $t = 0.2$ and 2 Gyr (left and right panels); $E(B-V) = 0.1$, [M/H] $= -1.7$ dex, $t = 0.5$ Gyr (middle panel) for the case of *UBVRI* passband set. The true positions of cluster parameters are marked by a white "plus" symbol. Black, gray and light-gray shaded areas correspond to $\delta_{\max} = 0.01$, 0.03 and 0.05 mag, respectively.

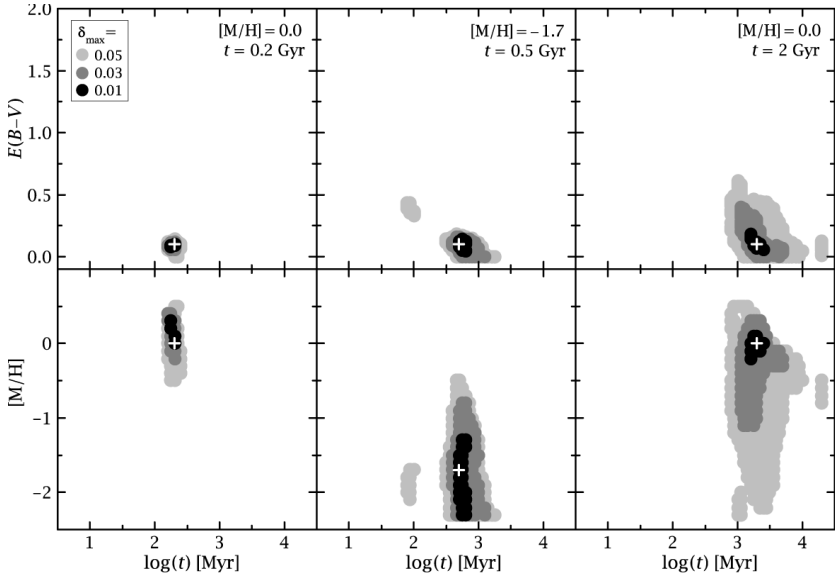

Fig. 2.21. The same as in Fig. 2.20, but for the case of *UBVRIJHK* passband set.

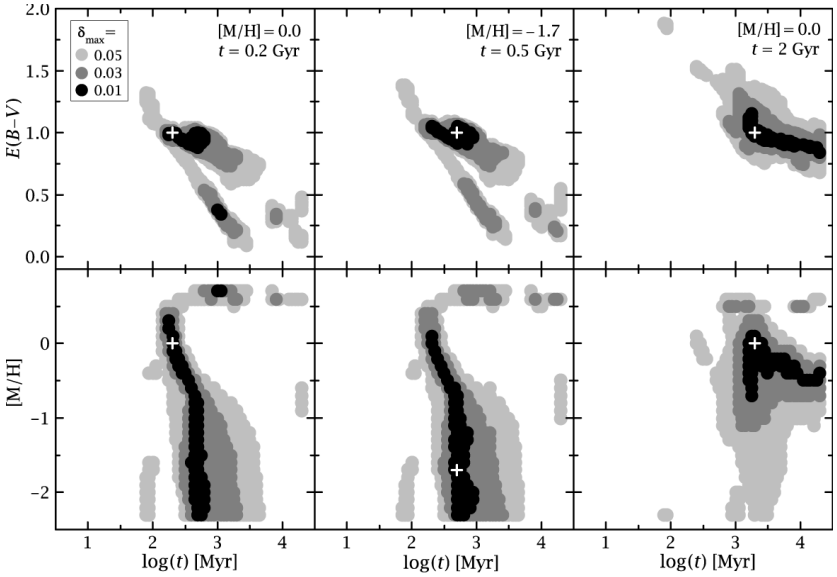

Fig. 2.22. The same as in Fig. 2.20 for the case of *UBVRI* passband set, but for $E(B-V) = 1.0$.

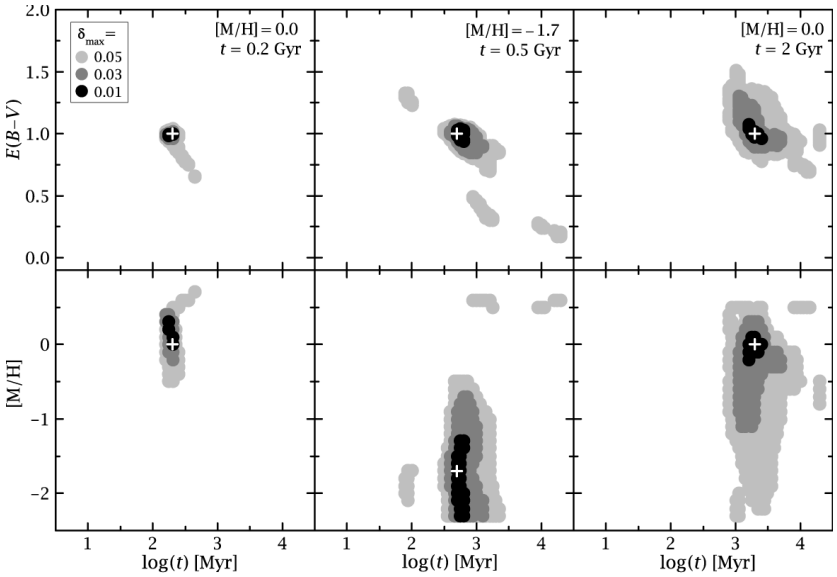

Fig. 2.23. The same as in Fig. 2.22, but for the case of *UBVRIJHK* passband set.

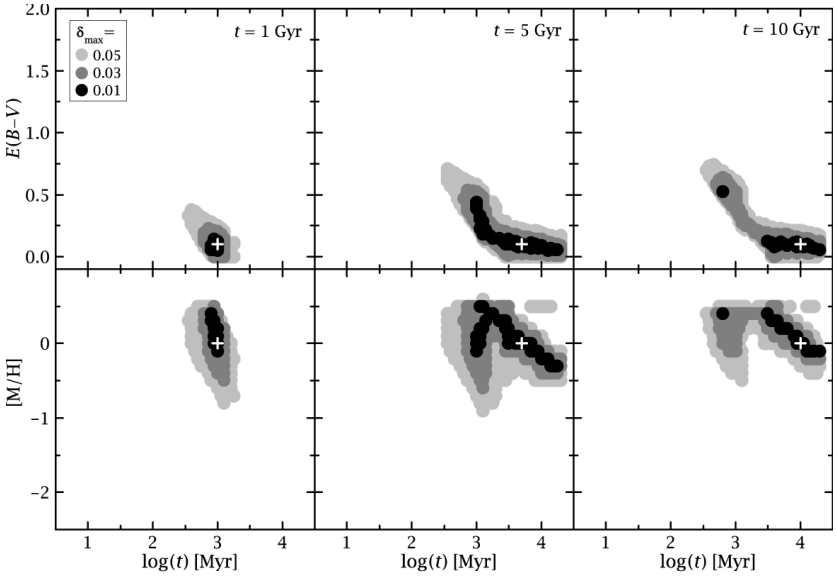

Fig. 2.24. The same as in Fig. 2.20 for the case of *UBVRI* passband set, but for the star clusters with the following parameters: $E(B-V) = 0.1$, [M/H] = 0.0 dex, t = 1, 5 and 10 Gyr.

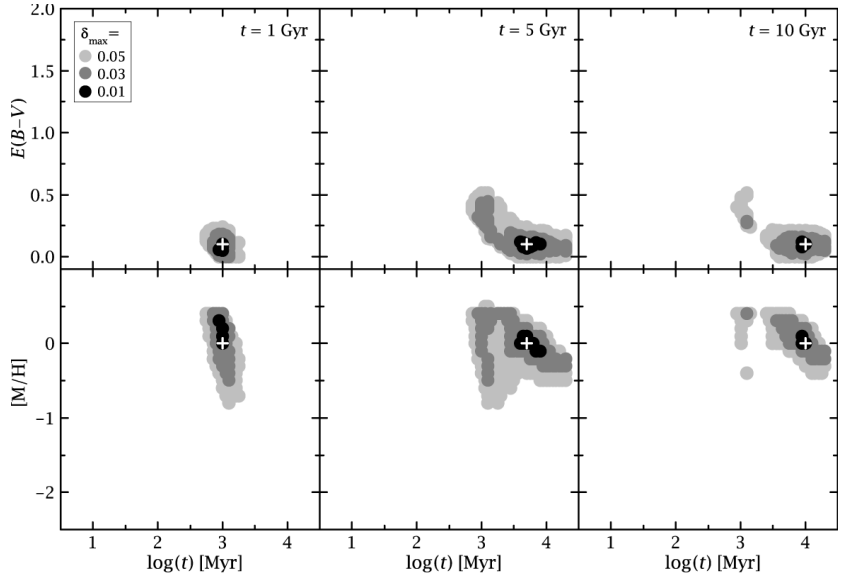

Fig. 2.25. The same as in Fig. 2.24, but for the case of *UBVRIJHK* passband set.

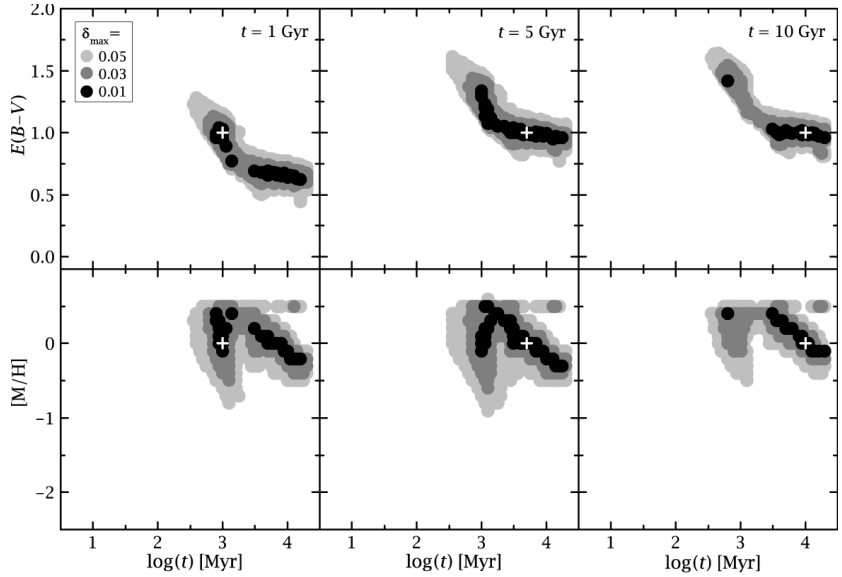

Fig. 2.26. The same as in Fig. 2.24 for the case of *UBVRI* passband set, but for $E(B-V) = 1.0$.

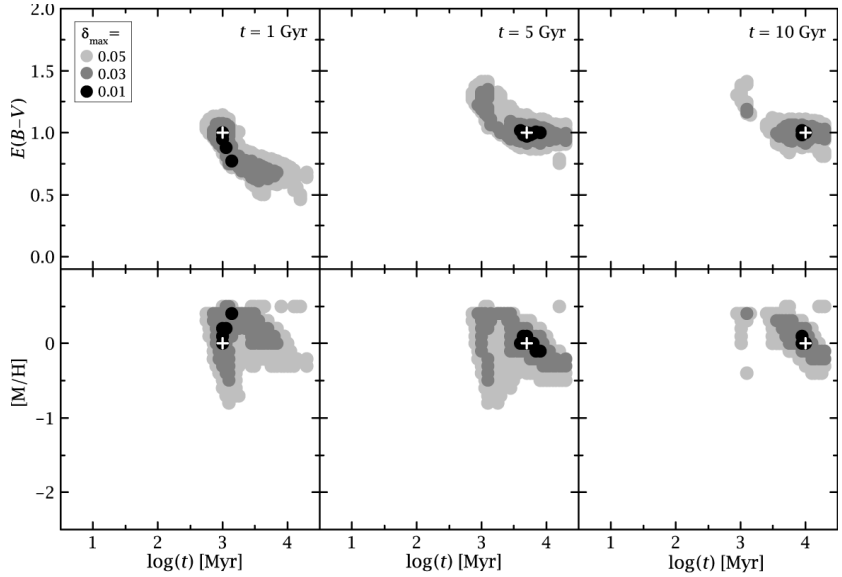

Fig. 2.27. The same as in Fig. 2.26, but for the case of *UBVRIJHK* passband set.

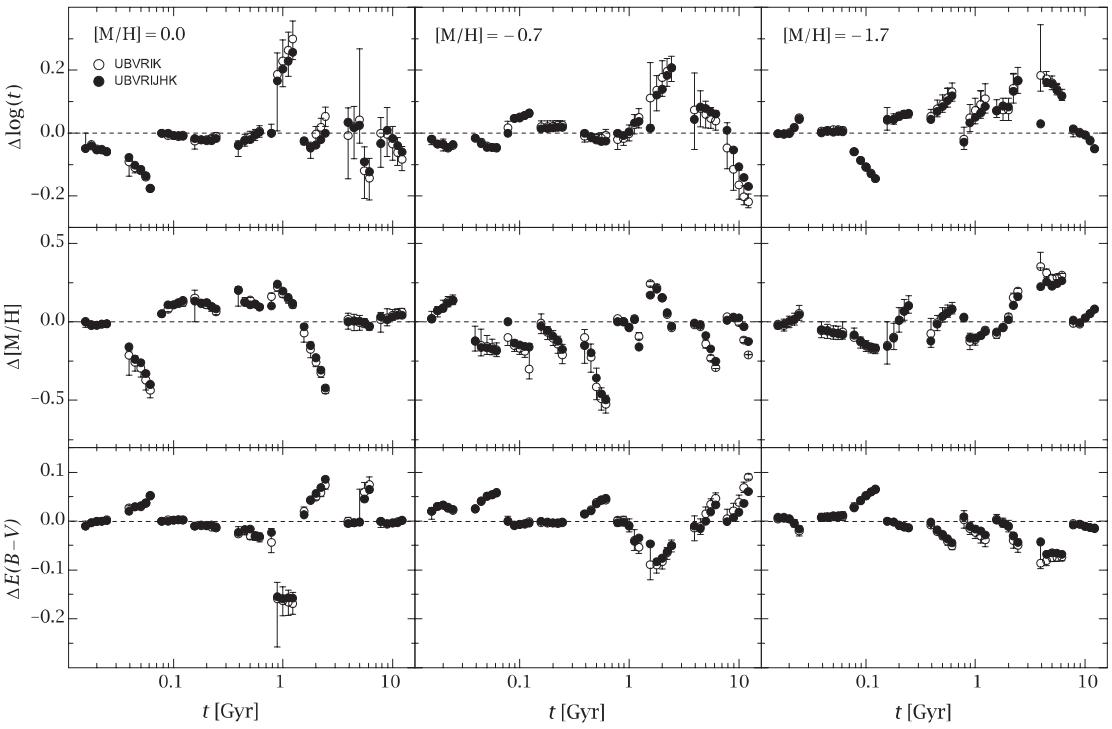

Fig. 2.28. Comparison of star cluster parameter quantification results for the case of color excess $E(B-V) = 1.0$ (see Fig. 2.18 for star cluster details). Black filled circles correspond to the case of *UBVRIJHK* passband set, open circles – to the *UBVRIK*. The error-bars show the sensitivity of determined cluster parameters to the artificial shift of the $V-K$ color by ± 0.03 mag.

cluster color indices must be better than 0.03 mag, which is rather difficult to achieve in infrared photometry.

We also investigated separately the influence of each infrared passband to the parameter determination precision with the purpose to find a minimum passband set, which would be sufficient for the quantification of clusters. The result is that all three color indices ($V-J$, $V-H$, $V-K$), added to the *UBVRI* photometric system separately, reduce the quantification errors, but $V-K$ is most important. Fig. 2.28 displays the quantification results for clusters using the *UBVRIJHK* (filled circles) and the *UBVRIK* (open circles) passband sets, both pictures are quite similar. Thus the K passband helps to solve majority of the parameter degeneracy problems. The error-bars in the *UBVRIK* case show the sensitivity of the parameters to the change of $V-K$ by ± 0.03 mag.

Recently an updated version of stellar isochrones, compared to those used in PEGASE, has been released by the Padova group, which includes

a more accurate treatment of thermally pulsating AGB stars (Marigo et al. 2008). It has been shown that the interpretation of integrated colors of unresolved galaxies can be significantly altered due to improved models of AGB stars by applying galaxy populations synthesis method and the new isochrone set (e.g., Tonini et al. 2008). In the case of SSP analysis of star clusters one can expect similar changes. Our method of the parameter degeneracy analysis, which is much simpler than the methods described in the literature (see, e.g., de Grijs et al. 2005), can be used to study the effects AGB stars on cluster colors by intercomparing parameter degeneracies in various SSP model frameworks.

We conclude that additional photometric information from the *JHK* passbands can significantly improve the accuracy of the determination of cluster parameters based on the PEGASE SSP models, in comparison with the results when photometry of only the *UBVRI* passbands is available. Even one additional K passband can improve significantly the capability of the *UBVRI* photometric system to eliminate age-metallicity and age-extinction degeneracies in the majority of the investigated cluster models, when the overall accuracy of color indices is better than $\sim$0.05 mag.

Note, however, that this condition of photometric accuracy is broken for young low-mass star clusters, where the stochastic effects, arising due to a few bright stars, dominate (e.g., Cervino & Luridiana 2004; Deveikis et al. 2008). This implies that even in case of ideal photometric calibrations, the uncertainty of cluster colors due to stochastic effects limits the applicability of SSP model fitting to derive evolutionary parameters of low-mass star clusters.

Chapter 3

Properties of Star Cluster Population

3.1 Parameter Determination

Star clusters were selected from the initial sample of 285 objects by considering the following criteria: (1) the derived half-light radius is of $r_h \geq 0.15''$ ($\geq$0.6 pc) – this limit arises due to the resolution of ground-based observations; (2) there are no nearby contaminants strongly influencing the accuracy of the derived structural and evolutionary parameters. Note, however, that several genuine star clusters, judged from the *HST* images, did not meet these criteria.

A few dim, i.e., low central surface brightness, objects with an unreasonably large derived half-light radius or composed of several resolved stars were rejected because of low reliability of determined parameters. Although PEGASE (Fioc & Rocca-Volmerange 1997) SSP models incorporate nebular emission lines for young age objects, we note that structural and evolutionary parameters of clusters showing up Hα emissions or superimposed on inhomogeneous diffuse Hα background should be considered with caution.

Note, however, that objects with strong Hα emission were cataloged separately by Kodaira et al. (2004), therefore, these objects were excluded from the analysis in this study. We note that foreground starburst galaxies possessing 24 μm emission, which have been revealed during spectroscopic study by Caldwell et al. (2009), might be present in a sample of young ($t \lesssim 20$ Myr) clusters.

This cleaning yielded a sample of 238 star clusters. Their ID numbers and center coordinates are supplemented with the structural and evolutionary parameters described in the following, and are presented in Tab. 3.1, the full form of which is available in the electronic edition of Vansevičius et al. (2009) available online[1].

[1]M31 cluster parameters: `http://dx.doi.org/10.1088/0004-637X/703/2/1872.`

Tab. 3.1. Evolutionary and Structural Parameters of High-Probability Star Cluster Candidates in the Southwest Field of the M31 Disk.

ID	α_{J2000}	δ_{J2000}	M_V[a]	log(t/ Myr)[b]	log(m/M$_\odot$)[c]	[M/ H][d]	$E(B-V)$[e]	r_h[f]
KW003	10.04519	40.89759	− 6.0	1.89	3.42	− 0.5	0.12	2.0
KW004	10.04568	40.60326	− 6.6	1.67	3.48	− 0.9	0.10	0.7
KW006	10.05430	40.60535	− 6.7	1.79	3.66	− 0.2	0.21	0.7
KW007	10.05468	40.69164	− 6.1	2.04	3.56	− 0.4	0.52	0.9
KW008	10.05671	40.63810	− 6.1	1.52	3.16	− 0.8	0.30	0.6
KW009	10.05700	40.76773	− 5.2	1.36	2.79	− 0.1	0.34	0.8
KW010	10.05768	40.67549	− 7.3	2.07	4.01	− 0.5	0.70	5.1
KW011	10.05924	40.65584	− 6.6	1.88	3.66	− 0.8	0.16	1.4
KW013	10.06067	40.62244	− 6.6	1.78	3.61	− 0.4	0.02	1.5
KW014	10.06177	40.77234	− 6.3	1.42	3.26	− 0.1	0.50	2.2

NOTES. ID number, R.A. and Decl. (J2000) coordinates of the photometric aperture center are in the USNO-B1.0 catalog system (degrees).
[a] Absolute magnitude, M_V, corrected for aperture correction.
[b] Age, t in Myr, log(t/Myr).
[c] Mass, m in solar mass units, log(m/M$_\odot$).
[d] Metallicity, [M/H].
[e] Interstellar extinction in MW plus M31; Color excess, $E(B-V)$.
[f] Average half-light radius in pc, $r_h = (r_h^{\rm K} + r_h^{\rm E})/2$, derived from the King and EFF models.
Full version of table is available in Vansevičius et al. (2009).

3.1.1 Structural Properties

Suprime-Cam V passband mosaic image ($\mathrm{FWHM_{PSF}} \approx 0.7''$, scale $0.2''\,\mathrm{pix}^{-1}$) was used to derive structural parameters of star cluster candidates. For objects saturated or having defects there, the LGGS field F7 V passband mosaic image ($\mathrm{FWHM_{PSF}} \approx 0.8''$, image scale $0.27''\,\mathrm{pix}^{-1}$) was substituted. Sub-images of 201×201 pix in size, centered on object's position, x_{in}, y_{in}, were cut from the mosaic and used for structure model fitting.

We applied the DAOPHOT package to compute single whole field PSF for each mosaic image. IRAF's `seepsf` was used to create PSF suitable for FitClust. The Suprime-Cam V passband mosaic image was also divided into 3×5 segments to compute their individual PSFs. These were treated as test objects and analyzed like star cluster candidates. The derived r_h values of test objects are confined to $r_h \lesssim [0.1''; 0.35\,\mathrm{pc}]$.

We have fitted 285 clusters from the initial sample with circular King (King 1962) and EFF (Elson et al. 1987) models. Since these models have different sensitivity to the cluster's "core" and "wings", comparison of the half-light radii derived by their means provides robustness of the model fit. Elliptical models were not used in this study due to stochastic distribution of bright cluster stars, which introduce fake ellipticity for the low-mass clusters (see Deveikis et al. 2008, for a discussion of stochastic effects). A number of contaminating stars used for the model fitting was: 0 in 40%, 1 in 30%, and 2 in 20% cases. The maximum number of fitted stars was 6.

Typical fitted values of structural parameters are: (1) the core radius, $r_c \sim 0.75\,\mathrm{pc}$, the concentration parameter, $c \sim 1.5$ (the King model); (2) the effective radius, $r_e \sim 0.75\,\mathrm{pc}$, and the power-law index, $n \sim 1.3$ (the EFF model). For ∼70% of clusters the derived c and n parameter values were confined to the reasonable limits of $0.5 \leq c \leq 2.5$ (see boundaries for MW GCs in Harris 1996) and $1.05 \leq n \leq 3.5$, respectively. For practical convenience, the remaining ∼30% of clusters, having determined parameters outside these limits, were re-fitted by setting particular parameters to the corresponding boundary values. We note, however, that although this slightly affects derived r_c or r_e, it does not change the derived half-light radii nor introduces systematic deviations in the residual images.

To estimate both the robustness of the model fitting and the uncertainty

of the derived half-light radius, σ_{r_h}, we have performed two tests: (1) varied photometric background value, $\mu_{\rm sky}$, which is kept constant during model fitting; and (2) decreased fitting radius, $r_{\rm fit}$, from the adopted initial value. These tests indicate that r_h based on the King and the EFF models are in a good agreement, and the overall accuracy of the r_h value is better than 20%. The typical σ_{r_h} is indicated by error-bars in Fig. 1.3 (a).

Based on these results, we applied a conservative lower limit, which mainly depends on the resolution of ground-based observations, of $r_h = 0.15''$ (0.6 pc) for the sample selection. Note, however, that some clusters below this limit have been identified in the *HST* images, which turned out to be of a very compact nature or dominated by a central bright star.

Intrinsic half-light radii of objects, based on the King, $r_h^{\rm K}$, and the EFF, $r_h^{\rm E}$, models, were derived. The half-light radii $r_h^{\rm E}$ vs. $r_h^{\rm K}$ plot of the initial sample of 285 objects is displayed in Fig. 1.3 (a) with typical uncertainty of the half-light radii, σ_{r_h}, indicated, and shows a good correlation and a distinct gap above the region where test objects are scattered. Therefore we defined a conservative lower limit of $r_h = [0.15''; 0.6\,{\rm pc}]$ and provide structural parameters for star cluster candidates above it, although some cluster candidates below this limit have been identified in the *HST* images and are of a very compact nature or dominated by a bright star.

The $r_h^{\rm K}$ and $r_h^{\rm E}$ of 233 star clusters in the southwest M31 field, derived by King and EFF model fits, respectively, are provided in Tab. 3.1. In the following analysis we use the average half-light radius value, $r_h = (r_h^{\rm K} + r_h^{\rm E})/2$. The histogram of r_h is displayed in linear (Fig. 3.1) and log (Fig. 1.3 (b)) scales, showing a prominent peak at $r_h \approx 1.5$ pc. The number of objects decreases (exponentially) with increasing r_h; largest clusters have $r_h \approx 14$ pc. The increase of number of $\sim$8 objects with $r_h \approx 6$ pc indicates a distinct group of extended clusters, which have very similar overall structure as judged from images and could be related evolutionary.

To test the influence of PSF variability on the derived half-light radii, we have divided survey field into 15 regions and constructed individual PSFs for these regions. These PSF models were treated as "virtual objects" and analyzed as star clusters in attempt to derive their structural parameters. The derived half-light radii of eight "virtual objects" are displayed with

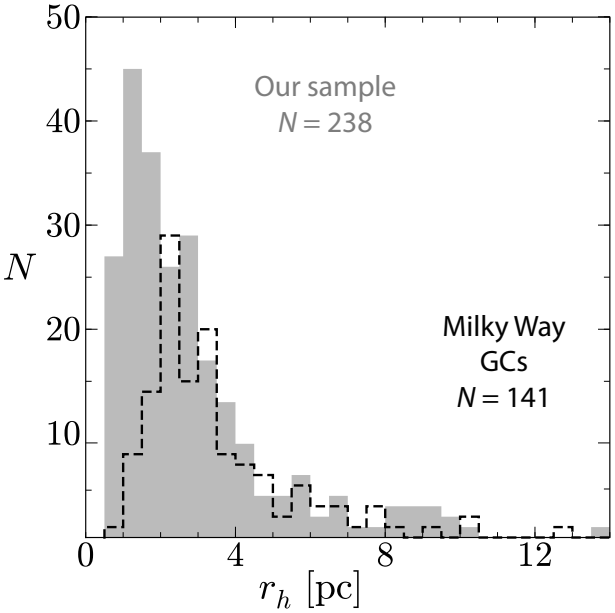

Fig. 3.1. Histogram of half-light radii of 238 star clusters in M31 southwest field. Deficiency of objects with $r_h < 1.5\,\mathrm{pc}$ is due to selection effects. The overplotted size distribution of MW GCs (Harris 1996, dashed line) indicates that most of our sample clusters are more compact.

asterisks in Fig. 1.3 (a) and are confined in the range of $r_h < 0.4\,\mathrm{pc}$. Note that only eight of 15 "virtual objects" are visible, since others failed to be fitted due to FWHM smaller than that of the adopted mosaic PSF. The scatter of $r_h < 0.4\,\mathrm{pc}$ corresponds to the r_h uncertainty of 20% for objects with $r_h \sim 2\,\mathrm{pc}$. It is the upper limit of uncertainty arising due to PSF variability across the survey field. For some individual clusters, we have additionally derived structural parameters by using local and mosaic PSFs, and found results being in a good agreement.

In case of semi-resolved star clusters, subtraction of contaminating stars has a strong effect on the accuracy of derived half-light radii. We have automatically included all stars within $r_{\mathrm{fit}} + \mathrm{FWHM_{PSF}}$ from the cluster's center and having magnitude $\leq(m_{\mathrm{cluster}} + 3)\,\mathrm{mag}$, i.e., up to 3 mag fainter than the cluster itself, into the fitting procedure. Also some individual strong contaminants were marked by hand.

Visual inspection of residual images proved that clusters and contaminating stars are subtracted well. We have estimated the goodness of model fitting by comparing the standard deviation of the sky background within the cluster's area after model subtraction and that of the nearby sky region. For ∼90% of cases, these values were equal, except for the cases with larger residuals visible in the cluster's core, which, most probably, arise due to semi-resolved stars.

We have compared r_h values of 50 bright objects from our sample with the ones derived by Šablevičiūtė et al. (2007). Despite different analysis methods employed, we have found a good agreement between these two studies. The maximum r_h difference of $\sim$30% is attributed to the influence of contaminating stars not properly accounted for in the previous study.

3.1.2 Evolutionary Properties

The *UBVRI* aperture CCD photometry data of 285 star clusters from the initial sample were compared with SSP models (PEGASE Fioc & Rocca-Volmerange 1997) assuming the standard initial mass function (IMF; Kroupa 2002) and various metallicities to yield the best fit model evolutionary parameters. The interstellar extinction was accounted for assuming the standard extinction law (Cardelli et al. 1989). The parameter quantification technique, supplemented with a detailed investigation of multi-band images, introduced to reduce the age-metallicity-extinction degeneracy, was used in the study.

The simple SSP model fitting results for 238 star clusters are provided in Tab. 3.1. The determined evolutionary parameters are: absolute V passband magnitude (corrected for aperture correction, see below for details), M_V; age in Myr, $\log(t/\mathrm{Myr})$; mass in solar mass units, $\log(m/\mathrm{M}_\odot)$; metallicity, [M/H]; and color excess, $E(B-V)$.

The standard deviation of age, $\sigma_{\log(t/\mathrm{Myr})}$, is plotted vs. V passband magnitude and age, $\log(t/\mathrm{Myr})$, in Figs. 3.2 (a) & (b), respectively. The standard deviation of age increases typically from $\sim$0.1 dex for young to $\sim$0.3 dex for old objects. We note that systematic differences of the derived parameters could be expected if another SSP model bank would be used. However, sample clusters were analyzed using PADOVA SSP models (Marigo et al. 2008) and good consistency with PEGASE results was found.

The histograms of the standard deviation of color excess, $\sigma_{E(B-V)}$, and metallicity, $\sigma_{[\mathrm{M/H}]}$, are shown in Figs. 3.2 (c) & (d), respectively. The characteristic $\sigma_{E(B-V)}$ is $\sim$0.05, reaching $\sim$0.15 for $t \sim 10$ Gyr objects due to stronger age-extinction degeneracy. The typical $\sigma_{[\mathrm{M/H}]}$ is $\sim$0.3 dex, reaching up to $\sim$0.7 dex for $t \sim 200$ Myr objects due to stronger age-metallicity degeneracy.

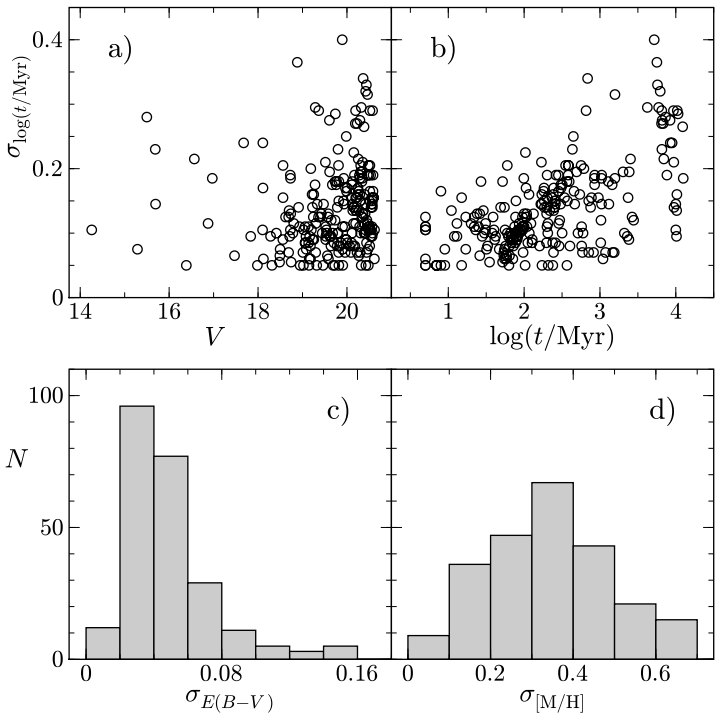

Fig. 3.2. Accuracy of the derived evolutionary parameters of 238 star clusters. Panels (a) and (b) show the standard deviation of age, $\sigma_{\log(t/\mathrm{Myr})}$, plotted vs. V passband magnitude and vs. age, $\log(t/\mathrm{Myr})$, respectively. Panels (c) and (d) display the histograms of standard deviations: color excess, $\sigma_{E(B-V)}$, and metallicity, $\sigma_{[\mathrm{M/H}]}$, respectively.

We note that in this study numerous SSP model simplifications were assumed: (1) a constant IMF; (2) a standard for MW and constant for all cluster stars extinction law; (3) solar element ratio. Additionally, in cases of unreliable photometric solutions for metallicity, we restricted [M/H] determination within lower and upper boundaries as a function of age taken from the chemical evolution model prediction.

Referring to models of MW and M31 by Renda et al. (2005), we assumed that metallicity evolution in the M31 survey field is not significantly different from that of Solar neighborhood, which has been modeled by Schonrich & Binney (2009). Therefore, the [M/H] boundaries roughly between -1 and $+0.5$ were considered, also taking into account possibility that oldest objects could be GCs in M31 halo with [M/H] as low as -2 dex.

The mass of clusters in the solar mass unit, $m/\mathrm{M}_\odot$, was calculated equating the mass-to-luminosity ratio of the best fit SSP model of age, t, and metallicity, [M/H], to the absolute V passband magnitude, M_V. The mass of clusters strongly depends on the derived age, therefore, the primary sources of mass uncertainty are the accuracy of age and extinction. Since cluster candidates in the crowded field were measured through small apertures, we have taken into account an individual aperture correction for each star

cluster by applying the following procedure.

Artificial clusters based on the best-fitted King model parameters were generated and convolved with the homogenized PSF of FWHM = 1.5″; i.e., resolution of model cluster images was matched to the LGGS frame resolution employed for cluster photometry. Individual aperture used for a real cluster was applied to measure corresponding model cluster, the difference between measured and total flux was assumed as an aperture correction for a real cluster photometry. A typical V passband aperture correction is of $\sim$0.4 mag and translates into a correction of mass by $\sim$0.15 dex in $\log(m/\mathrm{M}_{\odot})$ scale.

3.2 Results and Discussion

Here we analyze the structural and evolutionary parameters of 238 star clusters in the southwest field of the M31: half-light radius, age, mass, color excess, metallicity, and spatial distribution. We note that stochastic effects (see, e.g., Deveikis et al. 2008) are important sources of systematic bias and uncertainty of the derived parameters, in particular for young low-mass star clusters.

Assuming stochastic nature of star formation to randomly populate the stellar IMF, we modeled influence of stochastic effects on measurable cluster characteristics, and found that structural and evolutionary parameters could be biased – for some cluster age and mass intervals – in a systematic way. Recently, Barker et al. (2008) gave a strong caution that the standard SSP model analysis significantly underestimates uncertainty in the derived cluster age. However, only standard SSP model fitting was performed in this study; see a recent attempt to solve this problem for star clusters of solar metallicity by Maiz Apellaniz (2009).

3.2.1 Half-Light Radius

The histogram of clusters' half-light radius, r_h, displayed in Fig. 1.3 (b), spans the range from $\sim$0.6 pc to $\sim$10 pc with one large object of $r_h \sim 14$ pc (KW249); the distribution peaks at $r_h \sim 1.5$ pc. For comparison, the peak of the half-light radius distribution of MW GCs from Harris (1996, February

2003 rev.[2]) catalog is at ∼2.5 pc. Therefore, the majority of clusters from our M31 sample are smaller (more compact) than typical MW GCs.

The turnover and a lack of small-size clusters close to the applied lower limit of $r_h = 0.6$ pc can be attributed to the visual selection of the cluster sample. The exponential decrease in the number of clusters in the larger half-light radii domain should be real. Note, however, tests performed with SimClust (Deveikis et al. 2008) show that only extended clusters of low luminosity ($M_V \sim -4.5$), projected on star-forming regions, could be missed by visual inspection. The overplotted power-law slope $\eta = -2.2$ line, defined as $N(r_h)\mathrm{d}r_h \propto r_h^{\eta}\mathrm{d}r_h$, was found as the best fit for M51 star clusters by Bastian et al. (2005), and agrees well with our star cluster size distribution in the range of $r_h = 3$–8 pc. However, a considerably steeper slope was found in the M51 cluster sample of Scheepmaker et al. (2007), which is five times more numerous than that of Bastian et al. (2005).

The half-light radius of clusters is plotted vs. age, $\log(t/\mathrm{Myr})$, in Fig. 3.3 (a). No obvious half-light radius evolution with the age of cluster population, as has been found in LMC/SMC by Mackey & Gilmore (2003), can be judged from this diagram, since objects with large r_h are observed over a wide range of age. However, the lack of small-size clusters at age $t \sim 3$ Gyr can be attributed to the selection effects discussed by Hunter et al. (2003) for the LMC/SMC case, such that with increasing age only bright and, therefore, massive extended clusters are selected in the magnitude limited sample. At $t \sim 10$ Gyr, halo GCs likely dominate in our sample and show r_h distribution similar to that of the MW GCs population with r_h as small as ∼1 pc. They have high densities (see Fig. 3.3 (b)) and likely have survived tidal disturbances by the disk.

The half-light radius vs. mass, $\log(m/\mathrm{M}_\odot)$, distribution is shown in Fig. 3.3 (b), overplotted with five lines of constant half-mass density, $\rho_h = 3m/8\pi r_h^3$, ranging from 1 to $10^4\,\mathrm{M}_\odot\,\mathrm{pc}^{-3}$. The most numerous clusters in the M31 southwest field are compact clusters of small size $r_h \sim 1.5$ pc, intermediate mass $m \sim 4000\,\mathrm{M}_\odot$, and of young $t \sim 100$ Myr age. Largest clusters seem to be enveloped by the lines of ρ_h from 1 to $100\,\mathrm{M}_\odot\,\mathrm{pc}^{-3}$, lending an impression that massive clusters tend to be bigger in size as

[2]MW GCs: `http://physwww.mcmaster.ca/~harris/mwgc.dat`.

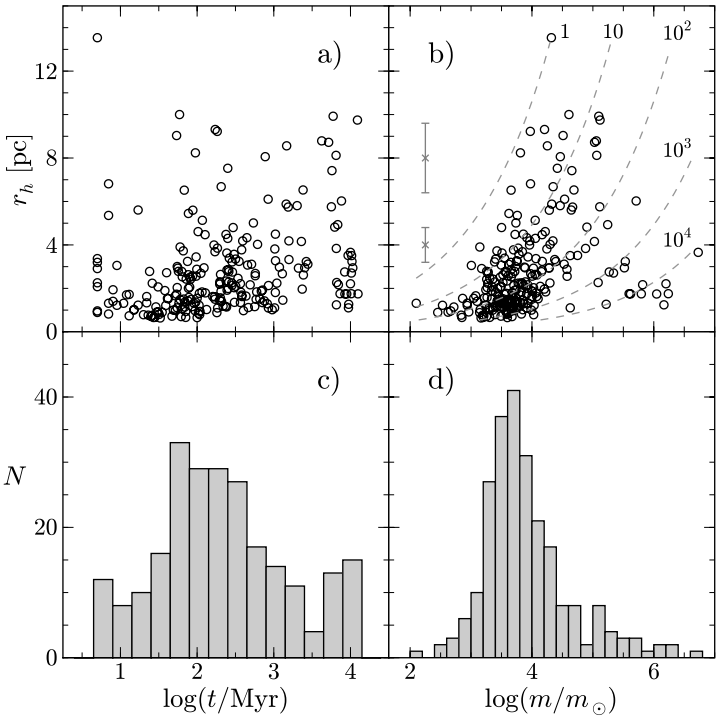

Fig. 3.3. Parameters of 238 star clusters. (a) Half-light radius, r_h, plotted vs. age, $\log(t/\mathrm{Myr})$. (b) r_h vs. mass, $\log(m/\mathrm{M}_\odot)$, overplotted with lines of a constant half-mass density, $\rho_h = 1, 10, 10^2, 10^3$, and $10^4\,\mathrm{M}_\odot\,\mathrm{pc}^{-3}$, from left to right, respectively. (c) and (d) Histograms of the derived cluster age, $\log(t/\mathrm{Myr})$, and mass, $\log(m/\mathrm{M}_\odot)$, respectively. In panel (b) error-bars indicate typical σ_{r_h}.

far as clusters of relatively low specific density of $\rho_h < 100\,\mathrm{M}_\odot\,\mathrm{pc}^{-3}$ are concerned (Hunter et al. 2003).

Comparing the r_h vs. mass distribution of our sample with a sample of M51 star clusters (Scheepmaker et al. 2007), we note a lack of objects with $4 \lesssim \log(m/\mathrm{M}_\odot) \lesssim 5$ and $r_h \lesssim 5\,\mathrm{pc}$ in our sample. The most massive, $\log(m/\mathrm{M}_\odot) \gtrsim 4.5$, clusters are "branching" in Fig. 3.3 (b) at small size, $r_h \lesssim 3\,\mathrm{pc}$, and high density, $\rho_h \sim 10^4\,\mathrm{M}_\odot\,\mathrm{pc}^{-3}$, which is characteristic to old GCs.

The oldest clusters, which have highest densities, are most likely halo GCs of small r_h. That the typical lifetime of $10^4\,\mathrm{M}_\odot$ mass star cluster is estimated to be of $\sim$300 Myr in the survey field implies very low probability for disk star clusters to reach an age of $\sim$10 Gyr without disruption. However, radial velocity measurements are necessary to confirm whether these objects belong to the halo.

3.2.2 Age

The distribution of clusters in the mass vs. age diagram is shown in Fig. 3.4. The upper right domain of the diagram, $t \gtrsim 3\,\mathrm{Gyr}$ and $4.0 \lesssim \log(m/\mathrm{M}_\odot) \lesssim 7.0$, is occupied by $\sim$30 classical GC candidates. The remaining $\sim$210 are most likely disk clusters, which reside in the domain of $t \lesssim 3\,\mathrm{Gyr}$ and

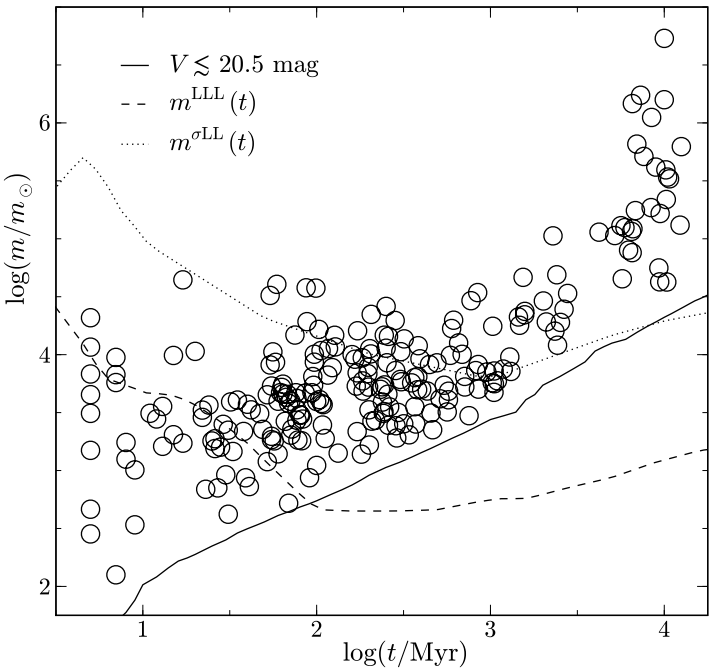

Fig. 3.4. Mass vs. age diagram of 238 star clusters, overplotted with sample selection limit, $V \lesssim 20.5$ mag, (solid line), the Lowest Luminosity Limit, $m^{\rm LLL}(t)$, (dashed line), and 10% stochastic fluctuation of cluster V passband luminosity, $m^{\sigma{\rm LL}}(t)$, (dotted line).

$\log(m/{\rm M}_\odot) \lesssim 4.5$. The curve along the lower envelope of cluster distribution is due to the selection limit of $V \lesssim 20.5$ mag, which was calculated with PEGASE SSP models of [M/H] $= -0.4$ dex metallicity, assuming zero extinction. Note that star clusters are located above the selection limit due to aperture corrections taken into account for mass calculation. However, the upper envelope of the distribution should be free of selection effects.

Cervino & Luridiana (2004) have shown that SSP models cannot be used in a straightforward deterministic way for small-mass cluster analysis, when integrated luminosity of a model is lower than that of the brightest star included in the used isochrone, i.e., "Lowest Luminosity Limit" (LLL) requirement. They defined the smallest mass, $m^{\rm LLL}$, associated with the LLL, and the mass, $m^{\sigma{\rm LL}}$, corresponding to the 10% stochastic fluctuation of the V passband luminosity, $\sigma_{L_V} = 0.1 \times L_V$, which translates into $\sim$0.04 dex uncertainty of $\log(m/{\rm M}_\odot)$. We have overplotted both parameters as a function of age in Fig. 3.4, taken from Cervino & Luridiana (2004), noting that $m^{\sigma{\rm LL}}(t) \sim 10 \times m^{\rm LLL}(t)$. Note, however, that SSP models of solar metallicity used by Cervino & Luridiana (2004) do not significantly influence a qualitative assessment of mass vs. age distribution.

Judging from Fig. 3.4, $m^{\rm LLL}$ is $\log(m/{\rm M}_\odot) \sim 4$ for clusters younger than $\sim$10 Myr. At the age of $\sim$50 Myr, $m^{\rm LLL}$ drops to $\log(m/{\rm M}_\odot) \sim 3$, therefore,

the majority of clusters from our sample satisfy the LLL requirement. At $t \sim 100\,\mathrm{Myr}$, the m^{LLL} coincides with $V \lesssim 20.5\,\mathrm{mag}$ selection limit; older objects are well above LLL. Therefore, clusters with $\log(m/\mathrm{M}_{\odot}) \gtrsim 4.5$ should have the most accurate evolutionary parameters.

The stochastic effects on the derived cluster mass can be estimated by referring to the dotted line in Fig. 3.4, based on the Cervino & Luridiana (2004) methods. The line displays 10% uncertainty of cluster's luminosity at a specific mass for a given age. Since we derived the mass from the V passband luminosity, the mass as a function of age, having 10% uncertainty of mass, is depicted by the dotted line in Fig. 3.4. Formally, mass uncertainty increases to 100% at the LLL indicated by the dashed line. However, the uncertainty of mass is additionally affected by the uncertainty of the derived age, which can be evaluated from the slope of solid line in Fig. 3.4, and also by the uncertainty of extinction shown in Fig. 3.2. Therefore, the LLL provides only the lower limit for uncertainty arising due to stochastic effects, which primarily bias age and extinction, and consequently – mass, i.e., actual accuracy of evolutionary parameters is lower than it is shown in Fig. 3.2.

The histogram of cluster age, displayed in Fig. 3.3 (c), spans the range from $t \sim 5\,\mathrm{Myr}$ to $\sim$12 Gyr. Since evolutionary parameters of the clusters with Hα emission are less reliable due to emission lines altering photometry and stochastic effects, we cannot properly estimate parameters of the clusters younger than $\sim$20 Myr. Therefore, we did not specifically target our survey for such star clusters.

The age distribution of clusters is displayed in Fig. 3.5 (a). We have calculated the number of clusters per linear age interval, $\mathrm{d}N/\mathrm{d}t$, by binning data in $\mathrm{d}\log(t/\mathrm{Myr}) = 0.2$, 0.3, and 0.5 age intervals, while also shifting them by a half-bin width. These results were averaged and smoothed. The symbol size indicates an uncertainty of the resulting distribution, which is plotted vs. age in a log scale. The age distribution is reasonably well represented with two power-law lines of different slopes, and is to be interpreted as a result of star cluster formation/disruption processes.

The cluster number distribution $\mathrm{d}N/\mathrm{d}t$ (Fig. 3.5 (a)) in general follows the "evolutionary fading" line. However, after subtracting the "evolutionary

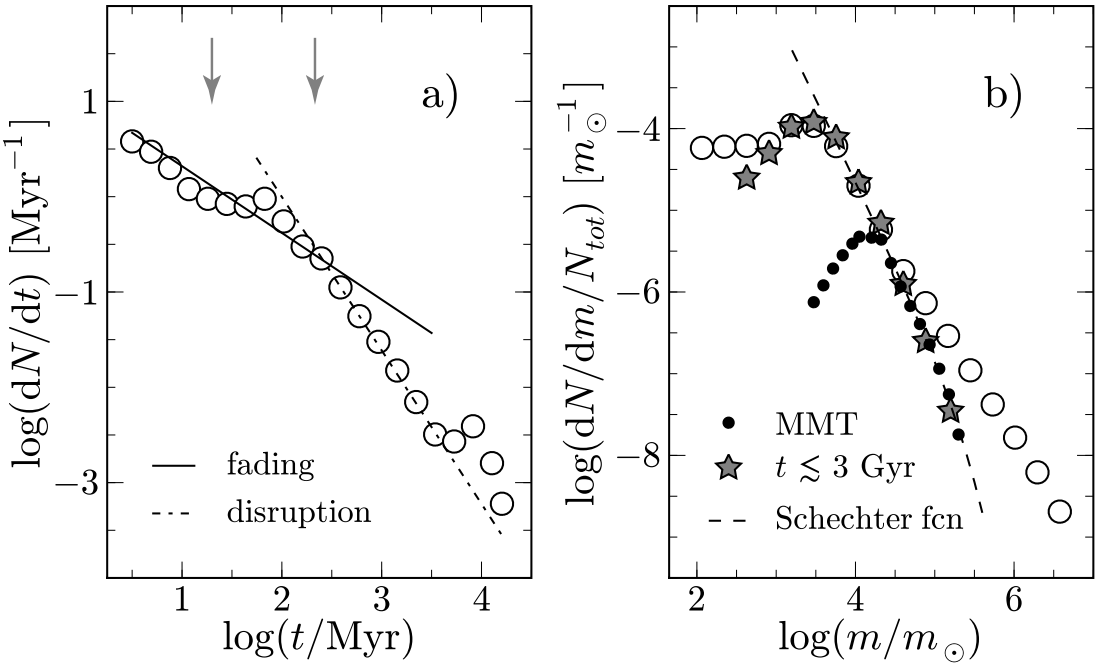

Fig. 3.5. Age and mass distributions of 238 star clusters, indicated by open circles (size indicates the uncertainty of data binning) in both panels. (a) Number of clusters per age interval, $\log(\mathrm{d}N/\mathrm{d}t)$, vs. age, $\log(t/\mathrm{Myr})$ (circles), overplotted with power-law slopes expected for cluster population forming continuously and: (1) fading evolutionary below the detection limit (solid line); (2) instantaneously disrupting at some arbitrary time (dash-dotted line). (b) Number of clusters per mass interval, normalized to the total number of clusters in the sample, $\log(\mathrm{d}N/\mathrm{d}m/N_{\mathrm{tot}})$, vs. mass, $\log(m/\mathrm{M}_\odot)$ (circles), overplotted with Schechter's function (dashed line; Gieles 2009), adopting the turnover mass of $m^* = 2 \times 10^5\,\mathrm{M}_\odot$. Stars correspond to the intermediate age star clusters from our sample in-between of $\sim$100 Myr and $\sim$3 Gyr; filled circles correspond to the star clusters from MMT spectroscopic survey by Caldwell et al. (2009, subsample $V < 19.0$ mag, ages in-between of $\sim$100 Myr and an upper age limit of their sample $\sim$1 Gyr).

fading" number gradient, a gradual increase in the number of clusters per log age interval from $t \sim 20$ Myr to $t \sim 100$ Myr is obvious. A peak of the cluster number distribution is followed with a decrease in the number of clusters, which is a consequence of an evolutionary cluster fading effect, being always significant in the magnitude limited sample (see Fig. 3.4), and star cluster disruption. We note that analysis of both Figs. 3.3 (c) & 3.5 (a) points to the peak of the cluster age distribution at $t \sim 70$ Myr, suggesting an enhanced cluster formation episode at that epoch. A smaller secondary peak at $\sim$10 Gyr is due to old GC candidates.

3.2.3 Mass

The histogram of cluster mass, displayed in Fig. 3.3 (d), spans the range from $\sim 10^2$ to $\sim 5 \times 10^6\,\mathrm{M}_\odot$ and shows a prominent peak at $m \sim 4000\,\mathrm{M}_\odot$. The decrease in the number of clusters in the low-mass domain is apparently not physical, but arises due to selection effects. The estimated completeness of our cluster sample is of $\sim$50% at $V \sim 20.5$ mag. Judging from these circumstances, the completeness at the age of $\sim$100 Myr and the mass of $\sim 4000\,\mathrm{M}_\odot$ (Fig. 3.4) should be credible, even taking into account a stochastic scattering of cluster luminosity at this age and mass. Therefore, decline in the number of clusters per log mass interval in the high-mass domain should be real.

The mass distribution of clusters is displayed in Fig. 3.5 (b). The number of clusters per linear mass interval, normalized to the total number of $N_{\mathrm{tot}} = 238$ clusters in our sample, $\mathrm{d}N/\mathrm{d}m/N_{\mathrm{tot}}$, was calculated by binning data in $\mathrm{d}\log(m/\mathrm{M}_\odot) = 0.2$, 0.3, and 0.5 mass intervals, and also shifting them by a half-bin width. These results were averaged and smoothed. The symbol size indicates the uncertainty of the resulting distribution. For a more detailed comparison of intermediate age (from $\sim$100 Myr to $\sim$3 Gyr) star clusters from our sample we have used the selected subsample ($V < 19.0$ mag, age from $\sim$100 Myr to an upper age limit of their sample $\sim$1 Gyr) of star clusters from the M31 disk study by Caldwell et al. (2009). The $\mathrm{d}N/\mathrm{d}m$ distribution presented in Caldwell et al. (2009) subsample was multiplied by 0.15, taking into account that our survey field covers only $\sim$15% of the M31 disk. We note that there are only eight objects in common between our sample and that of Caldwell et al. (2009).

Decline in the distribution of mass (Caldwell et al. 2009) when $\log(m/\mathrm{M}_\odot) < 4.3$ (see Fig. 3.5 (b)) arises due to a sample incompleteness and resembles a shape of our intermediate age sample distribution for mass less than $\log(m/\mathrm{M}_\odot) \sim 3.5$. Although we have only few star clusters in the high-mass range, the good match with a $\mathrm{d}N/\mathrm{d}m$ slope (Caldwell et al. 2009) and extension down to the mass as low as $\log(m/\mathrm{M}_\odot) \sim 3.7$ allows us to constrain a shape of the star cluster mass function for age in-between of $\sim$100 Myr and $\sim$1 Gyr.

We overplotted Schechter's mass function from Gieles (2009, see Eq. 3.1),

adopting the turnover mass of $m^* = 2 \times 10^5\,\mathrm{M}_\odot$, which shows a good agreement with both our intermediate age sample and Caldwell et al. (2009) subsample data. We note that only vertical adjustment (changing A value) for the Schechter's function was applied to match data at $m \sim 10^4\,\mathrm{M}_\odot$.

$$dN/dm = A \cdot m^{-2} \cdot \exp(-m/m^*)\,, \tag{3.1}$$

where m^* is a characteristic mass, where the exponential drop occurs and A is a constant that scales with the cluster formation rate.

Although we lack low-mass star clusters in our sample due to the selection limit at $V \sim 20.5\,\mathrm{mag}$ ($M_V \sim -4.0$), the detailed *HST* study of star clusters in M31 by Krienke & Hodge (2007, 2008) has revealed a numerous population of star cluster candidates as faint as $V \sim 23\,\mathrm{mag}$ ($M_V \sim -1.5$). They are spatially well correlated with brighter counterparts of $t \sim 100\,\mathrm{Myr}$ from our sample, therefore, it is reasonable to assume that they could be of a similar age. Thus, their mass should be significantly smaller than $\sim$4000 $\mathrm{M}_\odot$, corresponding to the mass range of typical MW OCs in the Solar neighborhood (Piskunov et al. 2008). Although the parameters of MW star clusters are derived basing on individual stars, note that masses of MW clusters are a subject to the accuracy of their derived tidal radii, as discussed by Piskunov et al. (2008).

The high-mass domain of clusters from our sample is found to be overlapping well with the sample of $\sim$140 young clusters, sharing the M31 disk rotation, studied using MMT spectra and *HST* images by Caldwell et al. (2009), who found a mass peak at $\log(m/\mathrm{M}_\odot) \sim 4$, significantly higher than for our cluster sample, probably, due to brighter cluster selection limit applied for spectroscopy. The mass range of clusters from our sample younger than $\sim$3 Gyr falls in-between of the MW GCs (McLaughlin & van der Marel 2005) and the MW OCs (Piskunov et al. 2008), indicating that we are mainly dealing with the disk clusters from the intermediate mass range. The mass distribution of clusters older than $\sim$3 Gyr overlaps well with the mass distribution of MW GCs (McLaughlin & van der Marel 2005).

Comparing the mass vs. age diagram of our cluster sample (Fig. 3.4) with those of LMC/SMC (Hunter et al. 2003) and M51 (Bastian et al. 2005), we see a prominent lack of massive, $\log(m/\mathrm{M}_\odot) \sim 5$, clusters younger than

$\sim$3 Gyr in M31. Although our survey covers only $\sim$15% of the deprojected M31 disk, it contains a representative part of its star-forming ring (Gordon et al. 2006) in the vicinity of NGC 206. We also note that other studies of the M31 disk clusters, which covered the whole galaxy, did not detect a significant number of clusters more massive than $\log(m/\mathrm{M}_\odot) \sim 4.5$ in this age range either (Caldwell et al. 2009, and references therein).

A few massive, $\log(m/\mathrm{M}_\odot) \sim 5$, objects with an estimated age of $t < 1$ Gyr were reported by Caldwell et al. (2009), who found that most of their young clusters have a low concentration, typical to the MW OCs. Their spatial distribution is subject to patchy field selection of *HST* high-resolution imaging over the M31 disk. Although there are only eight objects in common in their and our samples, judging from the overlapping mass range and the reasonable agreement of the derived age, we may tentatively assume that both samples belong to the same category of star clusters.

The general lack of star clusters of $\log(m/\mathrm{M}_\odot) \sim 5$ mass in the M31 disk could be due to a low-average star formation rate in M31 (Barmby et al. 2006). However, an unfavorable inclination angle of M31 could hide star clusters embedded in the M31 disk, mimicking the situation in MW (Clark et al. 2005) – there could be massive star clusters hidden by dust clouds and yet to be detected in M31. This hypothesis might be supported by the molecular cloud mass distribution in M31 (Nieten et al. 2006; Rosolowsky 2007), where star clusters with a mass of up to $\log(m/\mathrm{M}_\odot) \sim 5$ are expected to form, if the typical star formation efficiency of $\sim$30% in the cores of molecular clouds is assumed.

3.2.4 Extinction

A typical color excess of star clusters in our sample is $E(B-V) \sim 0.25$. Clusters younger than $\sim$500 Myr have a range of $E(B-V) \lesssim 1.0$, which is consistent with a large extinction of objects residing in the galaxy disk, e.g., four high extinction, $E(B-V) \sim 1.1$, objects of $t \sim 100$ Myr are projecting close to the 24 μm emission regions and prominent dust lanes. The range of $E(B-V) \lesssim 0.4$ derived for clusters of intermediate age, 500 Myr $\lesssim t \lesssim 3$ Gyr, might be related to the evolutionary fading of clusters and the observed narrow mass interval in this age range (see Fig. 3.4),

therefore, objects possessing color excess higher than ∼0.4 are missing from our sample. We note that $E(B-V)$ vs. projected distance from the M31 center does not show any tight correlation. Moreover, $E(B-V)$ of an individual cluster seems to be more strongly dependent on the local interstellar matter environment than on the radial distance from the M31 center.

The GC candidates of $t \gtrsim 3\,\mathrm{Gyr}$ have color excess over the range of $E(B-V) \lesssim 0.6$, consistent with their presence in the M31 halo on both sides of the disk. There are numerous objects with $E(B-V) \sim 0.04$, which is in a good agreement with MW color excess in the direction of the survey field in M31, estimated from the MW extinction maps (Schlegel et al. 1998).

Note, however, that for eight objects in common with Caldwell et al. (2009) sample, which have $E(B-V) \sim 0.25$ derived in their study, we determine color excess from 0.05 to 0.65. Although Caldwell et al. (2009) determined extinction by examining the shape of spectra continuum, for those cases when late-type stars dominate they used a mean color excess for young clusters of $E(B-V) \sim 0.28$, which is in agreement with the typical value of $E(B-V) \sim 0.25$ derived in our study for presumably the same population of star clusters.

3.2.5 Metallicity

The metallicity, [M/H], of star clusters, plotted vs. age and projected distance from the M31 center, R_{M31}, in Figs. 3.6 (a) & (b), respectively, spans a range from -2.0 to $+0.5$ dex. We divided clusters into two age groups of $t \lesssim 3\,\mathrm{Gyr}$ and $t \gtrsim 3\,\mathrm{Gyr}$, indicated by a different symbol size in Fig. 3.6 (b). The apparent narrowing of the metallicity scatter at an age of ∼200 Myr is attributed to the SSP model fitting artifact due to a strong age-metallicity degeneracy in this age domain. Although the accuracy of photometrically derived metallicity is low (see Fig. 3.2 (d)), the evolutionary trend with time is apparent.

A rather constant average metallicity of [M/H] ~ -0.4 dex is observed for clusters younger than ∼1 Gyr, however, there is a slight tendency of the average [M/H] to decrease with increasing galactocentric distance. The radial profile of cluster metallicity matches well those of disk red giant stars from Worthey et al. (2005) and Bellazzini et al. (2003) shown by lines in

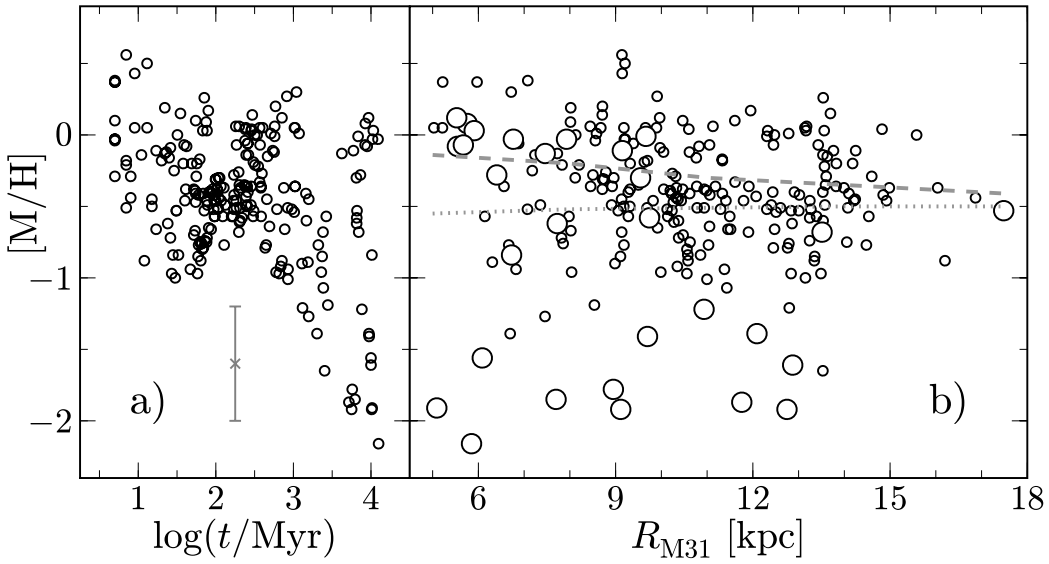

Fig. 3.6. Metallicity, [M/H], of 238 star clusters plotted vs. age, $\log(t/\mathrm{Myr})$, and projected distance from the M31 center, R_{M31}, in panels (a) and (b), respectively. In panel (a) error-bar indicates typical uncertainty of metallicity taken from Fig. 3.2 (d). In panel (b) clusters are divided into two age groups of $t \lesssim 3\,\mathrm{Gyr}$ (small circles) and $t \gtrsim 3\,\mathrm{Gyr}$ (large circles), and overplotted with the average metallicity trends for disk red giant stars from Worthey et al. (2005, dashed line) and Bellazzini et al. (2003, dotted line).

Fig. 3.6 (b).

There are 20 clusters in our sample, which have [Fe/H] estimates from the William Herschel Telescope (WHT) spectra by Perrett et al. (2002). By accounting for α-element overabundance typical to MW GCs, we see a reasonable agreement between photometric and spectroscopic metallicity estimates of old, $t \sim 10\,\mathrm{Gyr}$, clusters. Two of those metal-rich massive clusters (KW221 and KW225), presumably similar to GCs, have metallicity of [M/H] ~ -0.8 and 0.0 dex, and are found in our survey field area closest to the M31 bulge, located at the projected distance of $R_{\mathrm{M31}} \sim 5\,\mathrm{kpc}$ from the galaxy's center. Note, however, that for several objects of ∼100 Myr age, the metallicity estimated by Perrett et al. (2002) is of [Fe/H] ~ -2.2 dex, i.e., significantly lower than a photometrically estimated [M/H] ~ -0.4 dex.

The elaborated M31 evolution models, such as "M31 model-b" by Renda et al. (2005), may well reproduce the metallicity gradient and the metallicity change in time, as they are presented in Fig. 3.6. Detailed studies of the age-dependent profiles of the disk cluster population would provide further constraints on the M31 disk evolution models.

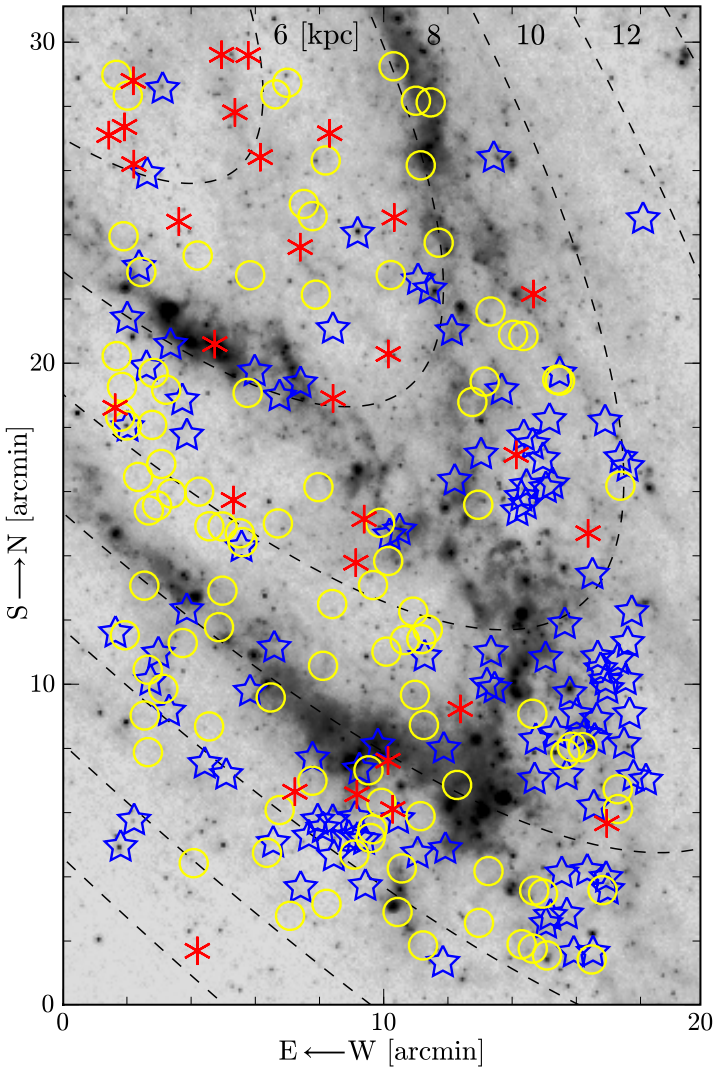

Fig. 3.7. Distribution of 238 star clusters in the M31 southwest field, overlaid on *Spitzer* (24 μm) image. Clusters are divided into three age groups: $t \lesssim 150$ Myr (stars), 150 Myr $\lesssim t \lesssim 3$ Gyr (circles), and $t \gtrsim 3$ Gyr (asterisks). Elliptical ring segments, indicating projected distance from the M31 center, $R_{\rm M31} = 6$–18 kpc, are marked with dashed lines. North is up, east is left.

3.2.6 Spatial Distribution

Positions of star clusters are indicated on the *Spitzer* (24 μm) image of the M31 southwest field in Fig. 3.7. Clusters are divided into three age groups: young ($t \lesssim 150$ Myr); intermediate (150 Myr $\lesssim t \lesssim 3$ Gyr); and old ($t \gtrsim 3$ Gyr), shown by different symbols. The distribution of young clusters resembles that of warm dust, but is shifted outward to larger $R_{\rm M31}$ by $\sim$1.5 kpc along the galaxy's major axis. The intermediate age clusters are smoothly distributed over the whole field. Old age clusters (GC candidates) scatter over the area, but show a higher concentration toward the M31 bulge.

Star clusters with ultraviolet (*GALEX*) or 24 μm (*Spitzer*) emission are mainly distributed along the sites of active star formation. At the bottom

of the survey field, young and intermediate age clusters appear to be well mixed. Around the position of [6′,16′], where a lack of warm dust is attributed to the "split" of the star forming ring, intermediate age clusters dominate. However, around [17′,11′] mainly young clusters are observed. The spatial density of young and intermediate age clusters decreases toward the bulge, which is consistent with a gas distribution in the M31 disk (Nieten et al. 2006).

To explain the M31 spiral structure and features of the prominent star-forming ring at $R_{\mathrm{M31}} \sim 10\,\mathrm{kpc}$, two scenarios of the M32 galaxy having passed through the M31 disk were recently proposed: (1) passage through the disk occurred ∼20 Myr ago (Gordon et al. 2006) and created a "split" of the ring around position [6′,16′] (see Fig. 3.7; NGC 206 is located at the ring's "branching" point [15′,17′]); (2) passage through the M31 center occurred ∼210 Myr ago (Block et al. 2006). The star cluster population data could provide a reference to disentangle the more preferable scenario.

True locations of objects in the M31 disk are subject to a strong projection effect due to an unfavorable inclination angle of ∼75°. The projection of the galaxy and its rotation are such that the southwest field of the disk approaches the observer (Henderson 1979); the corotation radius lies beyond $R_{\mathrm{M31}} \sim 20\,\mathrm{kpc}$ (Efremov 1980; Ivanov 1985); and the rotation period at $R_{\mathrm{M31}} \sim 10\,\mathrm{kpc}$ distance is of ∼250 Myr. Assuming that all clusters in our sample are residing in the M31 disk, we made a deprojection of cluster locations to face-on view, and referring to the disk rotation curve (Carignan et al. 2006), computed object positions as a function of look-back time.

Judging by eye, the clumps of young clusters, which are located at [9′,5′] and [17′,10′], formed two compact spatial configurations $\sim 70 \pm 20$ Myr ago. This age coincides well with the cluster age peak and suggests a possible evolutionary connection. There was no other compact spatial cluster configuration noted in the look-back time range from ∼20 Myr to ∼150 Myr, which is valid for this kind of study based on our cluster sample. The range of the age distribution peak, estimated from the SSP model fitting, is of ∼50–120 Myr. However, there is an age-metallicity degeneracy observed at the age of ∼100 Myr, which could introduce slight bias to the age determination. Therefore, we note this interesting coincidence of cluster age peak

and compact spatial cluster configurations. To discuss this finding more reliably, a global kinematic study of the M31 disk cluster population and a detailed dynamic model of the M31 and M32 encounter are needed. Note, however, that Caldwell et al. (2009) did not find evidence for a peak in star formation between 20 Myr and 1 Gyr.

3.2.7 Objects for Detailed Study

Here we present several remarkable objects, which could serve as targets for future spectroscopy and high-resolution imaging. We briefly discuss their properties referring to the derived parameters, multi-band and *HST* images. We provide cross-referencing with the Revised Bologna Catalog of M31 GCs and candidates compiled by Galleti et al. (2007) in brackets when available.

KW044 (B325) is located at the position of [16′,2′] in Fig. 3.7 and is resolved in Suprime-Cam images. The structural model fit resulted in a large half-light radius, $r_h \sim 11$ pc, and an extremely small ratio of King model parameters, $r_t/r_c \sim 3$. Its age of ∼60 Myr, mass of $\log(m/\mathrm{M}_\odot) \sim 4.6$, and radial velocity of -560 km s^{-1}, compatible with gas disk velocity at this position, imply that KW044 is a representative of the young disk cluster population. However, another solution for evolutionary parameters (a low extinction case) also exists – the cluster could be an old object of low concentration and low metallicity, resembling the extended ones in M31 (Mackey et al. 2006) and M33 (Stonkutė et al. 2008), and suggesting its location in the M31 halo. The age of ∼630 Myr is derived by Caldwell et al. (2009).

KW072 (VdB0) is located at the position of [15′,7′] in Fig. 3.7. A visual impression that it is surrounded by an enhanced surface number density of stars (ejected from cluster) is confirmed by the structural model fit, indicating its extended nature – structural model parameters: ratio $r_t/r_c \sim 300$ (King), $n \sim 1$ (EFF), and $r_h \sim 5.5$ pc. Its young age of ∼20 Myr is confirmed by a strong ultraviolet (*GALEX*) flux. A mass, $\log(m/\mathrm{M}_\odot) \sim 4.6$, of the cluster, which formed recently, is remarkably high comparing with the MW typical OCs' mass. This cluster was studied in detail by Perina et al. (2009) based on photometry of individual stars from *HST* images. The parameters derived are in a very good agreement with values derived

in the present study based on its integrated properties.

KW141 (B011D) is located at the position of [11′,15′] in Fig. 3.7. It represents a population of young, ∼10 Myr, intermediate-mass, $\log(m/\mathrm{M}_\odot) \sim 3.8$, clusters. However, stochastically appearing four bright red stars enclose the blueish central part of this object suggesting an older age. Its *HST* WFPC2 color image is displayed in Fig. 3.8 (a). The age and mass of this "stochastic cluster example" are in good agreement with Caldwell et al. (2009): ∼30 Myr and $\log(m/\mathrm{M}_\odot) \sim 3.8$.

KW249 – the most controversial object is located close to the M31 bulge at the position of [3′,29′] in Fig. 3.7. Its young age of ∼10 Myr and a mass of $\log(m/\mathrm{M}_\odot) \sim 4.3$ make it incompatible with the structural parameter best-fit model indicating very high ratio of $r_t/r_c > 500$ (King model) and large half-light radius of $r_h \sim 14$ pc (the most extended object in our cluster sample). It is associated with 24 μm (*Spitzer*) and HI emission, probably, still being an embedded cluster with $E(B-V) \sim 1.5$, which could explain the absence of Hα and ultraviolet emission. It was imaged with the *HST* WFPC2 (F606W filter), displayed in Fig. 3.8 (b) (fitted elliptical models provide the ellipticity of ∼0.75 – a ratio of minor to major axis). We suggest that it could be either: (1) an intermediate-mass cluster, which expanded after a rapid gas removal phase (Baumgardt & Kroupa 2007), or (2) a background galaxy, having emission in K_s (2MASS) attributed to older stellar populations.

KW271 and KW273 (G099*) – a double cluster candidates are located at the position of [2′,18′] in Fig. 3.7. KW271 is centered on a strong 24 μm emission source, its parameters are: $t \sim 10$ Myr, $\log(m/\mathrm{M}_\odot) \sim 3.7$, $E(B-V) \sim 0.9$, and $r_h \sim 3.6$ pc. Contrarily, KW273 has no 24 μm emission, is much older ($t \sim 800$ Myr), more massive ($\log(m/\mathrm{M}_\odot) \sim 4.5$), has a low color excess ($E(B-V) \sim 0.1$), and large half-light radius ($r_h \sim 4.3$ pc). The structural parameters of two "adhered" cluster candidates were derived by masking KW271 and fitting the brighter KW273. After subtracting the best-fit model of KW273 from the original image, KW271 was fitted. In total, seven iterations of the object subtraction were performed, leading to fine residual images. We suggest two possible explanations of the nature of these objects: (1) they make a double cluster, similar to those detected in

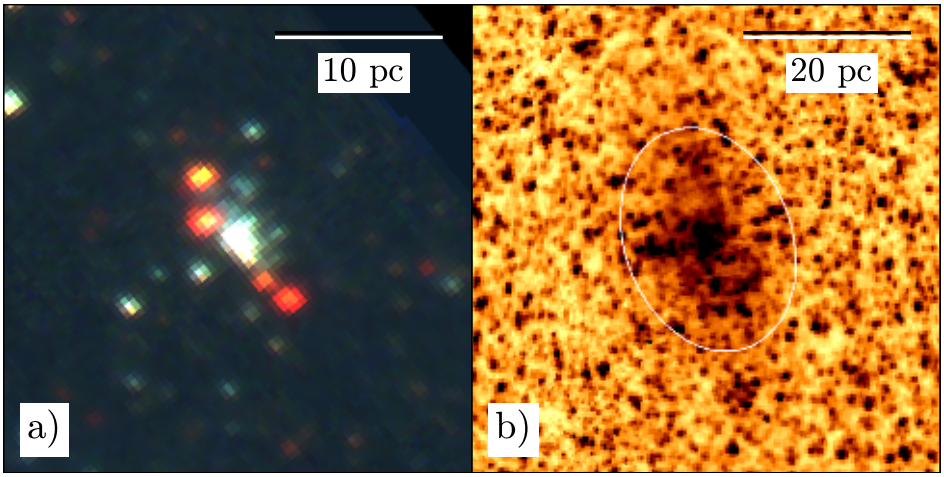

Fig. 3.8. *HST* images. Panels show: (a) KW141 – an example of stochastic appearance of red bright stars (color coding of *HST* filters: red – F814W, green – F555W, and blue – F439W); (b) KW249 – an object with the largest half-light radius, $r_h \sim 14$ pc, in our sample (F606W filter, overplotted with ellipse indicating r_h, derived via elliptical King model fit). Note different image scales in panels (a) and (b). North is up, east is left.

LMC/SMC (Carvalho et al. 2008), with one component just emerging from the embedded phase. Close image inspection reveals an extended "halo" enshrouding both these objects, however, the derived age difference does not support this case; (2) both clusters (they could be a cluster and a galaxy – 24 μm emission source) are the result of spatial projection, however, probability of such a close coincidence is low. We note that Caldwell et al. (2009) classify KW271 as a background galaxy based on the measured redshift $z \sim 0.15$, and for KW273 they provide age of ∼400 Myr and mass $\log(m/\mathrm{M}_\odot) \sim 4.0$ in reasonable agreement with our values.

KW279 (B205D) is located at a large projected galactocentric distance, thus far from the star-forming ring, at the position of [2′,5′] in Fig. 3.7. It is associated with strong 24 μm emission, which is indicator of its young age of ∼10 Myr. A low-mass, $\log(m/\mathrm{M}_\odot) \sim 3.2$, substantial color excess, $E(B-V) \sim 0.6$, and a moderate size, $r_h \sim 2$ pc, were deduced assuming it being a star cluster. However, its asymmetric shape with a blueish "tail", pointing at a neighboring 24 μm emission source, implies that it could be an interacting starburst galaxy. We note that Caldwell et al. (2009) classify KW279 as a background galaxy based on the measured redshift $z \sim 0.1$.

3.2.8 Cluster Formation and Disruption

If star clusters are being formed continuously at a constant rate with a power-law cluster initial mass function, their number increases with time in the mass vs. age diagram as described by Boutloukos & Lamers (2003). Consequently, the mass of the most massive cluster in the older log age bins rises due to a statistical effect of sample size. However, in our sample, we see a lack of massive $\log(m/\mathrm{M}_\odot) \gtrsim 4$ clusters older than $\sim$100 Myr (Fig. 3.4), probably, indicating a non-constant cluster formation history. Therefore, using the observed mass and age distributions of star clusters we attempt to derive their formation and disruption rates in the studied field by adopting the technique developed by Boutloukos & Lamers (2003).

For a simple estimate, first we selected clusters more massive than $\log(m/\mathrm{M}_\odot) \sim 3.5$. There are $N_1 \sim 30$ and $N_2 \sim 70$ objects in the age ranges $\Delta t_1 \equiv 30 \lesssim t \lesssim 100\,\mathrm{Myr}$ and $\Delta t_2 \equiv 100\,\mathrm{Myr} \lesssim t \lesssim 1\,\mathrm{Gyr}$, respectively. If a cluster formation rate (CFR) is constant and there is no cluster disruption, then a ratio of $N_2/N_1 = \Delta t_2/\Delta t_1 \approx 13$ is expected. The actual ratio is $N_2/N_1 \sim 2$, indicating that CFR is not constant and/or significant cluster disruption took place during the last Gyr in the M31 disk.

The number of clusters per linear age interval, $\mathrm{d}N/\mathrm{d}t$, plotted vs. age in Fig. 3.5 (a) can be described by two power-law slopes, intersecting at $t \sim 300\,\mathrm{Myr}$. The slope values were taken from the fading/disruption models by Boutloukos & Lamers (2003, Eq. 14: $\alpha = 2.0$, $\gamma = 0.62$, $\zeta = 0.69$) and only vertical adjustment to the observed distribution was applied. In the age domain of $t \lesssim 300\,\mathrm{Myr}$ the slope line, expected for a cluster population forming continuously and fading in the course of evolution below the detection limit, provides a rather good match to the observed data. Around $t \sim 70\,\mathrm{Myr}$, there is a sudden increase in the number of clusters by a factor of $\sim$2, which could be attributed to the increased CFR at that epoch. In the age domain older than $\sim$300 Myr, the observed distribution can be well described by the slope expected for a cluster disruption at some arbitrary time. An increase in the cluster number at $t \sim 10\,\mathrm{Gyr}$ is attributed to the GC candidates, prominent in our sample.

The number of clusters per linear mass interval, $\mathrm{d}N/\mathrm{d}m$, is displayed vs. mass in Fig. 3.5 (b). In the mass range of $\log(m/\mathrm{M}_\odot) \lesssim 3.3$ the incom-

pleteness of our cluster sample is obvious. Due to incompleteness, the mass distribution of our cluster sample cannot be used to constrain the typical lifetime of star clusters since the fading line cannot be adjusted properly. Note that the distribution of clusters in between ∼100 Myr and ∼3 Gyr and in the mass range of $\log(m/\mathrm{M}_\odot) \gtrsim 4.5$ is steeper than that of the whole sample, which includes the old GC candidates.

Using the Boutloukos & Lamers (2003) technique and relying on the power-law slope line intersection point in Fig. 3.5 (a), we estimate a conservative value of typical lifetime of $\log(m/\mathrm{M}_\odot) = 4$ mass cluster to be of $t_4^{\mathrm{dis}} \sim 300$ Myr in the M31 survey field. For comparison, the following values in other galaxies were derived by Lamers et al. (2005): M51 central region – ∼70 Myr; M33 – ∼630 Myr; MW Solar neighborhood – ∼560 Myr; and SMC – ∼8 Gyr.

The cluster disruption analysis gives the disruption time of ∼500 Myr if only cluster age distribution of our sample is used. If the mass distribution is taken into account (although it is difficult to define intersection point of fading and disruption lines in Fig. 3.5 (b)), the cluster disruption time can be estimated to be as small as ∼100 Myr since it is sensitive to the "intersection" mass. Therefore, we choose $t_4^{\mathrm{dis}} \sim 300$ Myr as a conservative value. We note that a similar inconsistencies between age and mass distribution analyses were noticed recently for LMC star clusters by Parmentier & de Grijs (2008). However, they found an opposite effect for the LMC sample – the cluster mass distribution analysis tends to yield higher cluster disruption timescale than the age distribution analysis. Such discrepancy might be related to the assumptions applied in the Boutloukos & Lamers (2003) analysis used in our study: (1) a constant cluster formation rate; (2) a power-law cluster initial mass function, which should be of the Schechter's function type.

Lamers et al. (2005) found anti-correlation between the lifetime, t_4^{dis}, of $\log(m/\mathrm{M}_\odot) = 4$ mass cluster and the ambient density of its environment, ρ_{amb}, in the galaxies. Following the reasoning by Lamers et al. (2005), we estimate ρ_{amb} in the M31 disk. We took the structural parameters of the M31 disk from the best-fit model of Geehan et al. (2006): a disk scale-length, $R_d = 5.4$ kpc; a central surface density, $\Sigma_0 = 4.6 \times 10^8\,\mathrm{M}_\odot\,\mathrm{kpc}^{-2}$.

Therefore, the average disk surface density at $R_{\rm M31} \sim 10\,{\rm kpc}$, i.e., at the center of our survey field $\Sigma = \Sigma_0 \exp(-R_{\rm M31}/R_d) \sim 70\,{\rm M}_\odot\,{\rm pc}^{-2}$.

van der Kruit (2002) has shown that for spiral galaxies the vertical scale height is of $h_z \sim 0.15\,R_d$; this implies $h_z^{\rm stars} \sim 800\,{\rm pc}$. Braun (1991) found $h_z^{\rm gas} \sim 350\,{\rm pc}$ for a gas distribution at a galactocentric distance of $R_{\rm M31} = 10\,{\rm kpc}$. The scale height for dust distribution is assumed to be of $h_z^{\rm dust} \sim 100$ and $\sim$150 pc by Hatano et al. (1997) and Semionov et al. (2003), respectively. Depending on the adopted h_z, the estimated ambient density in our survey field, $\rho_{\rm amb} \sim 0.5\,\Sigma\,h_z^{-1}$, is in the range of $\rho_{\rm amb} \sim 0.05 \ldots 0.35\,{\rm M}_\odot\,{\rm pc}^{-3}$. This density is much lower than the typical half-mass density $\rho_h \sim 10^2\,{\rm M}_\odot\,{\rm pc}^{-3}$ of star clusters, shown in Fig. 3.3 (b).

Referring to Fig. 4 in Lamers et al. (2005), we see that values of $t_4^{\rm dis} \sim 300\,{\rm Myr}$ and $\rho_{\rm amb} \sim 0.05 \ldots 0.35\,{\rm M}_\odot\,{\rm pc}^{-3}$ derived here, place the studied field of the M31 disk in the position between MW and M33 and M51, however, slightly below the predicted theoretical $t_4^{\rm dis} = t_4^{\rm dis}(\rho_{\rm amb})$ line (see Fig. 3.9).

Gieles et al. (2006) have modeled encounters of star clusters with molecular clouds to explain the short disruption time for star clusters in the M51 central region. Our survey field in M31 is centered on the star-forming ring possessing high-density gas (Nieten et al. 2006), therefore, enhanced star cluster disruption in respect to MW and M33 could apparently take place. Although Rosolowsky (2007, and references therein) discuss similarity of the molecular cloud properties in M31 and MW, enhanced star cluster disruption should apparently take place in the M31 molecular gas "ring" in respect to that of the Solar neighborhood. The whole field survey of the M31 disk clusters and more detailed models of cluster and cloud kinematics, which are needed to estimate encounter cross sections in the disk, should be considered in future.

Finally, we attempt to estimate the CFR in the M31 disk. We select $N = 51$ clusters with age $\Delta t \equiv 30\,{\rm Myr} \lesssim t \lesssim 130\,{\rm Myr}$ and mass $3.3 \lesssim \log(m/{\rm M}_\odot) \lesssim 4.5$ (see Fig. 3.4). This subsample should have accurately estimated parameters and be relatively free of selection and cluster disruption effects. The total stellar mass of these clusters is $\Delta m \sim 3 \times 10^5\,{\rm M}_\odot$.

Assuming the constant power-law cluster mass function (index -2.0;

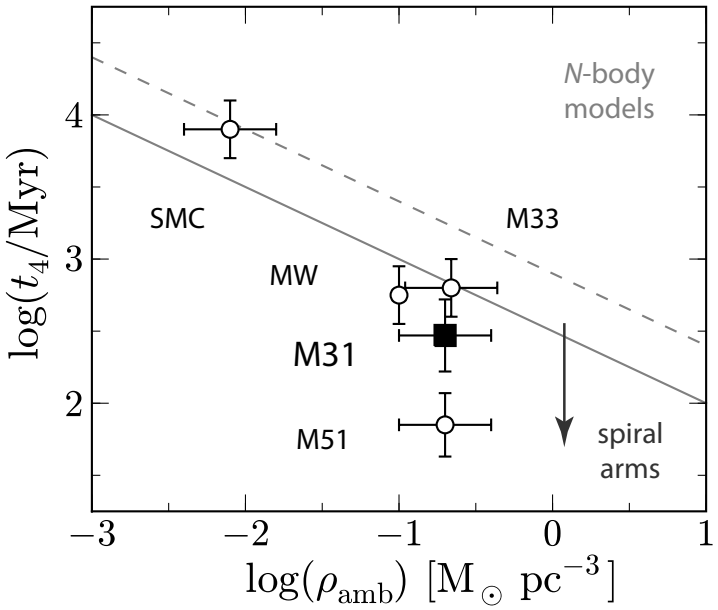

Fig. 3.9. Predicted dependence of lifetime of the $10^4\,M_\odot$ mass star cluster versus the mean ambient density in the galaxy disk. Values for SMC, MW Solar neighborhood, M33, M51 (Lamers et al. 2005) and M31 at 10 kpc galactocentric distance derived in this stydy are indicated and follow predictions of N-body models. Cluster disruption in M51 is enhanced due to strong spiral arms.

Gieles 2009) down to $\log(m/M_\odot) = 2$, mass correction factor of ∼2.5 was deduced. Therefore, the approximate rate of star formation in the clusters was $\mathrm{CFR_{field}} = \Delta m/\Delta t \sim 0.008\,M_\odot\,\mathrm{yr}^{-1}$. The deprojected area of survey field (Fig. 3.7) is of ∼70 kpc^2, making ∼15% of the galaxy disk. From this, we estimate the lower limit of the average CFR at the epoch of ∼100 Myr to be of $\mathrm{CFR_{M31}} \sim 0.05\,M_\odot\,\mathrm{yr}^{-1}$ over the M31 disk. This can be compared to the present-day star formation rate of $0.4\,M_\odot\,\mathrm{yr}^{-1}$ (Barmby et al. 2006), indicating that $\gtrsim$10% of formed stars could remain "locked" in star clusters during ∼100 Myr.

For comparison, Williams (2003) found the mean star formation rate for the disk $\sim 1\,M_\odot\,\mathrm{yr}^{-1}$ over the last 60 Myr. Based on stellar population analysis, he suggests that the lowest star formation rate occurred ∼25 Myr ago being ∼2 times lower compared with the epoch from ∼50 Myr to ∼250 Myr. Note a good coincidence of star formation history in M31 deduced by Williams (2003) and one inferred from our cluster population data (Fig. 3.5 (a)), which suggests an episode of a double increase in cluster formation ∼70 Myr ago. Also, Kodaira et al. (1999) have found that the star formation rate in the field around OB association A24 has decreased by ∼2.5 times from the epoch at ∼1 Gyr to the present day.

Although clusters in the intermediate mass range ($3.5 \lesssim \log(m/M_\odot) \lesssim 4.5$) are not well known in the MW, the compact clusters in M31 might rep-

resent a new class of star clusters of intermediate age $30\,\mathrm{Myr} \lesssim t \lesssim 3\,\mathrm{Gyr}$, linking the age of GC formation and the present. It could be suspected that this class of disk-population clusters is not observed in the MW because of high extinction through the Galactic plane. This might be supported by the Clark et al. (2005) discovery that a Galactic star cluster Westerlund 1 is a Super Star Cluster with a mass of up to $\log(m/\mathrm{M}_\odot) \sim 5$, age of $\sim$3 Myr, and radius of 0.6 pc, which suffers strong interstellar extinction of $A_V \sim 11.5\,\mathrm{mag}$ being at the distance of $\sim$5 kpc. Therefore, a more numerous massive compact star cluster population also could be hidden by dust clouds in the M31 disk.

The sample of compact star clusters in the present homogeneous photometric survey of the $17.5' \times 28.5'$ field in the southwest field of the M31 disk is apparently overlapping with the clusters detected in the patchy *HST* fields, in terms of their mass $3.0 \lesssim \log(m/\mathrm{M}_\odot) \lesssim 4.5$, which is in-between of the mass of typical OCs and classical GCs, well known in the MW. The structural properties of the compact clusters are similar to those of GCs, except for minor irregularities, and they resemble those of massive clusters in the LMC/SMC, including blue clusters of globular appearance.

These findings suggest a rich intermediate-mass cluster population in M31, which appears to be scarce or hidden by dust clouds and still to be uncovered in the Milky Way. The global follow-up survey of the whole M31 disk cluster population is of great importance.

Conclusions

Observational evidence that star formation proceeds in a clustered manner raise a question on the mass function of star clusters and their evolution. However, we have a limited scope of these processes in the MW. The M31 galaxy is the nearest stellar system similar to MW, therefore, it is the most suitable one to provide clues for understanding evolution of the star cluster population and galaxy structures. However, detailed study of stellar populations and star clusters is a challenging task for ground-based observations due to crowded stellar fields.

We have carried out a survey of compact star clusters in the southwest field of the M31 galaxy, based on the high-resolution Suprime-Cam images ($17.5' \times 28.5'$), covering ∼15% of the galaxy disk area. The *UBVRI* photometry of 285 cluster candidates ($V \leq 20.5$) was performed using frames of the Local Group Galaxies Survey (Massey et al. 2006).

Data analysis methods and programs were developed, tested, and applied for: reduction of wide-field images registered with mosaic CCD cameras; determination of structural parameters of semi-resolved star clusters; quantification of evolutionary parameters of star clusters based on integrated broadband multicolor photometry.

The sample, containing 238 high-probability star cluster candidates (typical half-light radius, $r_h \sim 1.5\,\mathrm{pc}$), was selected by specifying a lower limit of $r_h \gtrsim 0.15''$ ($\gtrsim 0.6\,\mathrm{pc}$). We derived cluster parameters based on the photometric data and multi-band images by employing simple stellar population models.

Clusters are in a wide range of ages from ∼5 Myr (young objects, associated with warm dust and/or Hα emission) to ∼10 Gyr (globular cluster candidates), and show a mass distribution concentrating around $3.0 \leq \log(m/\mathrm{M}_\odot) \leq 4.3$, peaking at $m \sim 4000\,\mathrm{M}_\odot$. Typical ages of these intermediate-mass clusters are in the range of $30\,\mathrm{Myr} \leq t \leq 3\,\mathrm{Gyr}$, with a prominent peak at ∼70 Myr. The age peak is located in between of the suspected M32 galaxy passages through the central region of our survey field ∼20 Myr ago (Gordon et al. 2006) and the center of the M31 galaxy

$\sim$210 Myr ago (Block et al. 2006).

The derived lifetime of the $10^4\,M_\odot$ mass cluster in M31 galaxy before disruption is of $\sim$300 Myr, which is in between those of MW and M51 galaxies (Lamers et al. 2005). The derived cluster formation rate is $\sim 5 \times 10^4\,M_\odot$/Myr, while star formation rate is $\sim 4 \times 10^5\,M_\odot$/Myr, i.e., only $\sim$10% of stars remain in clusters at the age of $\sim$100 Myr.

The mass function of star clusters is similar to that in other low star formation activity galaxies and is best described by the Schechter's function with a characteristic mass of $\sim 2 \times 10^5$ solar masses. These findings suggest a rich intermediate-mass cluster population in M31 galaxy, which appears to be scarce or hidden by dust clouds and still to be uncovered in MW. The global follow-up survey of the entire M31 galaxy disk cluster population is of great importance.

The developed methods and software are applicable for the forthcoming surveys of distant galaxies up to $\sim$20 Mpc, e.g., with James Webb Space Telescope, where high-resolution imaging will enable to achieve resolution similar to that in this Suprime-Cam study of the M31 disk.

References

Anders P., Bissantz N., Fritze-v. Alvensleben U., et al. 2004, MNRAS, 347, 196

Barker S., de Grijs R., Cervino M. 2008, A&A, 484, 711

Barmby P., Ashby M.L.N., Bianchi L., et al. 2006, ApJ, 650, L45

Barmby P., Holland S., Huchra J.P. 2002, AJ, 123, 1937

Barmby P., McLaughlin D.E., Harris W.E., et al. 2007, AJ, 133, 2764

Bastian N., Gieles M., Lamers H.J.G.L.M., et al. 2005, A&A, 431, 905

Baumgardt H., Kroupa P. 2007, MNRAS, 380, 1589

Bellazzini M., Cacciari C., Federici L., et al. 2003, A&A, 405, 867

Bertin E. 2009, Memorie della Societa Astronomica Italiana, 80, 422

Bik A., Lamers H.J.G.L.M., Bastian N., et al. 2003, A&A, 397, 473

Block D.L., Bournaud F., Combes F., et al. 2006, Nature, 443, 832

Boutloukos S.G., Lamers H.J.G.L.M. 2003, MNRAS, 338, 717

Braun R. 1991, ApJ, 372, 54

Bridžius A., Narbutis D., Stonkutė R., et al. 2008, Baltic Astronomy, 17, 337

Caldwell N., Harding P., Morrison H., et al. 2009, AJ, 137, 94

Cardelli J.A., Clayton G.C., Mathis J.S. 1989, ApJ, 345, 245

Carignan C., Chemin L., Huchtmeier W.K., et al. 2006, ApJ, 641, L109

Carvalho L., Saurin T.A., Bica E., et al. 2008, A&A, 485, 71

Cervino M., Luridiana V. 2004, A&A, 413, 145

Charbonneau P. 1995, ApJS, 101, 309

Clark J.S., Negueruela I., Crowther P.A., et al. 2005, A&A, 434, 949

Cohen J.G., Matthews K., Cameron P.B. 2005, ApJ, 634, L45

de Grijs R., Anders P., Lamers H.J.G.L.M., et al. 2005, MNRAS, 359, 874

de Grijs R., Fritze-v. Alvensleben U., Anders P., et al. 2003, MNRAS, 342, 259

de Vaucouleurs G. 1958, ApJ, 128, 465

Deveikis V., Narbutis D., Stonkutė R., et al. 2008, Baltic Astronomy, 17, 351

Efremov Y.N. 1980, Soviet Astronomy Letters, 6, 152

Elson R.A.W., Fall S.M., Freeman K.C. 1987, ApJ, 323, 54

Fioc M., Rocca-Volmerange B. 1997, A&A, 326, 950

Galleti S., Bellazzini M., Federici L., et al. 2007, A&A, 471, 127

Galleti S., Federici L., Bellazzini M., et al. 2004, A&A, 416, 917

Geehan J.J., Fardal M.A., Babul A., et al. 2006, MNRAS, 366, 996

Gieles M. 2009, MNRAS, 394, 2113

Gieles M., Portegies Zwart S.F., Baumgardt H., et al. 2006, MNRAS, 371, 793

Gil de Paz A., Boissier S., Madore B.F., et al. 2007, ApJS, 173, 185

Gilliland R.L. 1994, ApJ, 435, L63

Gordon K.D., Bailin J., Engelbracht C.W., et al. 2006, ApJ, 638, L87

Harris W.E. 1996, AJ, 112, 1487

Hatano K., Branch D., Fisher A., et al. 1997, ApJ, 487, L45

Henderson A.P. 1979, A&A, 75, 311

Hill A., Zaritsky D. 2006, AJ, 131, 414

Hunter D.A., Elmegreen B.G., Dupuy T.J., et al. 2003, AJ, 126, 1836

Ivanov G.R. 1985, Ap&SS, 110, 357

Jordi C., Hog E., Brown A.G.A., et al. 2006, MNRAS, 367, 290

Kaluzny J., Stanek K.Z., Krockenberger M., et al. 1998, AJ, 115, 1016

Kaviraj S., Rey S.C., Rich R.M., et al. 2007, MNRAS, 381, L74

Kidger M., Martin-Luis F., Artigue F., et al. 2006, The Observatory, 126, 166

Kim S.C., Lee M.G., Geisler D., et al. 2007, AJ, 134, 706

King I. 1962, AJ, 67, 471

Kodaira K. 2002, vol. 15 of Reviews in Modern Astronomy, 1–26

Kodaira K., Vansevičius V., Bridžius A., et al. 2004, PASJ, 56, 1025

Kodaira K., Vansevičius V., Stonkutė R., et al. 2008, vol. 399 of Astronomical Society of the Pacific Conference Series, 431–438

Kodaira K., Vansevičius V., Tamura M., et al. 1999, ApJ, 519, 153

Krienke O.K., Hodge P.W. 2007, PASP, 119, 7

—. 2008, PASP, 120, 1

Kroupa P. 2001, MNRAS, 322, 231

—. 2002, Science, 295, 82

Lamers H.J.G.L.M., Gieles M., Portegies Zwart S.F. 2005, A&A, 429, 173

Larsen S.S. 1999, A&AS, 139, 393

Li Z., Han Z., Zhang F. 2007, A&A, 464, 853

Mackey A.D., Gilmore G.F. 2003, MNRAS, 338, 85

Mackey A.D., Huxor A., Ferguson A.M.N., et al. 2006, ApJ, 653, L105

Magnier E.A., Cuillandre J. 2004, PASP, 116, 449

Magnier E.A., Lewin W.H.G., van Paradijs J., et al. 1992, A&AS, 96, 379

Maiz Apellaniz J. 2002, in The 2002 *HST* Calibration Workshop: *Hubble* after the Installation of the ACS and the NICMOS Cooling System, ed. S. Arribas, A. Koekemoer, & B. Whitmore, 346–349

—. 2004, PASP, 116, 859

—. 2009, ApJ, 699, 1938

Marigo P., Girardi L., Bressan A., et al. 2008, A&A, 482, 883

Massey P., Olsen K.A.G., Hodge P.W., et al. 2006, AJ, 131, 2478

McConnachie A.W., Irwin M.J., Ferguson A.M.N., et al. 2005, MNRAS, 356, 979

McLaughlin D.E., van der Marel R.P. 2005, ApJS, 161, 304

Miyazaki S., Komiyama Y., Sekiguchi M., et al. 2002, PASJ, 54, 833

Mochejska B.J., Kaluzny J., Stanek K.Z., et al. 2001, AJ, 122, 1383

Narbutis D., Bridžius A., Stonkutė R., et al. 2007, Baltic Astronomy, 16, 421

Narbutis D., Stonkutė R., Vansevičius V. 2006a, Baltic Astronomy, 15, 471

Narbutis D., Vansevičius V., Kodaira K., et al. 2006b, Baltic Astronomy, 15, 461

—. 2008, ApJS, 177, 174

Nieten C., Neininger N., Guelin M., et al. 2006, A&A, 453, 459

Ochsenbein F., Bauer P., Marcout J. 2000, A&AS, 143, 23

Padmanabhan N., Schlegel D.J., Finkbeiner D.P., et al. 2008, ApJ, 674, 1217

Parmentier G., de Grijs R. 2008, MNRAS, 383, 1103

Perina S., Barmby P., Beasley M.A., et al. 2009, A&A, 494, 933

Perrett K.M., Bridges T.J., Hanes D.A., et al. 2002, AJ, 123, 2490

Pflamm-Altenburg J., Kroupa P. 2008, Nature, 455, 641

Piskunov A.E., Schilbach E., Kharchenko N.V., et al. 2008, A&A, 477, 165

Renda A., Kawata D., Fenner Y., et al. 2005, MNRAS, 356, 1071

Rosolowsky E. 2007, ApJ, 654, 240

Scheepmaker R.A., Haas M.R., Gieles M., et al. 2007, A&A, 469, 925

Schlegel D.J., Finkbeiner D.P., Davis M. 1998, ApJ, 500, 525

Schonrich R., Binney J. 2009, MNRAS, 396, 203

Schuster M.T., Marengo M., Patten B.M. 2006, vol. 6270 of Society of Photo-Optical Instrumentation Engineers Conference Series

Semionov D., Stonkutė R., Vansevičius V. 2003, Baltic Astronomy, 12, 633

Stetson P.B. 1987, PASP, 99, 191

—. 1996, PASP, 108, 851

Stonkutė R., Vansevičius V., Arimoto N., et al. 2008, AJ, 135, 1482

Tody D. 1993, in Astronomical Data Analysis Software and Systems II, ed. R. J. Hanisch, R. J. V. Brissenden, & J. Barnes, vol. 52 of Astronomical Society of the Pacific Conference Series, 173–183

Tonini C., Maraston C., Devriendt J., et al. 2008, arXiv:0812.1225

Šablevičiūtė I., Vansevičius V., Kodaira K., et al. 2006, Baltic Astronomy, 15, 547

—. 2007, Baltic Astronomy, 16, 397

van der Kruit P.C. 2002, in The Dynamics, Structure History of Galaxies: A Workshop in Honour of Professor Ken Freeman, ed. G. S. Da Costa & H. Jerjen, vol. 273 of Astronomical Society of the Pacific Conference Series, 7–18

Vansevičius V., Arimoto N., Hasegawa T., et al. 2004, ApJ, 611, L93

Vansevičius V., Bridžius A. 1994, Baltic Astronomy, 3, 193

Vansevičius V., Kodaira K., Narbutis D., et al. 2009, ApJ, 703, 1872

Westmeier T., Braun R., Thilker D. 2005, A&A, 436, 101

Williams B.F. 2003, AJ, 126, 1312

Williams B.F., Hodge P.W. 2001a, ApJ, 559, 851

—. 2001b, ApJ, 548, 190

Worthey G. 1994, ApJS, 95, 107

Worthey G., Espana A., MacArthur L.A., et al. 2005, ApJ, 631, 820

Yagi M., Kashikawa N., Sekiguchi M., et al. 2002, AJ, 123, 66